University of Crete

Study of visible and infrared sensors based on two dimensional materials

Stavrakaki Alexandra

Thesis Submitted

For the degree of Master of Science

Academic Supervisor: Prof. Alexandros Georgakilas

Scientific Supervisor: Dr. George Deligeorgis

DEPARTMENT OF PHYSICS

Heraklion 2016

CONTENTS

Acknowledgments

Firstly, I would like to express my gratitude to my academic supervisor, Prof. Alexandros Georgakilas for giving me the opportunity to work in the facilities of the Microelectronics Research Group (MRG).

Moreover, I would like to express my sincere appreciation and gratitude to my scientific supervisor Dr. George Deligeorgis for the excellent cooperation we had during these years. His guidance and support were valuable during this study and I am grateful for that. His willingness to spend his time and knowledge for giving me the grounding to deal with research activities has been greatly appreciated. In addition, I would like to thank Prof. Chatzopoulos Zaharias and Prof. Savvidis Pavlos for their willingness to participate in my thesis committee.

Furthermore, my special thanks to Dr. Fabrice Iacovella and Dr. Vladimir Prudkovskiy, both members of the research group I worked with. I would like to express my great appreciation to Fabrice for his substantial assistance to device fabrication and Vladimir for the exceptional collaboration we had during the experiments. Also, their knowledge and advice were highly helpful for my studies and I am sincerely thankful for their support. Special thanks to my colleague and third member of the group, Kostas Triantopoulos. Even though we occupied on different subjects, his encouragement and support was truly valuable.

I would also like to express my thanks to Maria Androulidaki for her crucial assistance and for the great cooperation we had during the experiments.

Special thanks to my family for encouraging me all this time in every possible way.

Finally, great thanks to my friends, Alexandros Tsimis, Ioannis Michail, Marina Stivaktaki, Elisa Papadopoulou, Ioanna Demeridou, and Simos Tsintzos, for their great assistance and support during the years of my study.

Abstract

Detection of light (photodetection) is the prominent issue which has been widely investigated the recent decades by the research community in optoelectronics and used for applications in biomedical imaging, molecular sensing and telecommunication.

Transition metal dichalcogenides (TMDs) belong to the family of 2 dimensional (2D) materials. They exhibit great optical properties and have attracted the interest of optoelectronic research.

The scope of this thesis is to construct and investigate photodetecting devices based on MoS_2, a member of the 2D – TMDs group. MoS_2 was used through a dispersion (liquid phase exfoliated MoS_2) in order to fabricate a significant amount of devices for testing. Raman analysis was used for the characterization of the deposited MoS_2 films. From Raman spectra a trilayer form of MoS_2 crystal was estimated. The photodetectors that were tested were fabricated with different metal electrodes and deposited on different substrates.

Concerning the first samples, MoS_2 was deposited on Si/SiO_2 substrate with asymmetric Pt/Ti metal contacts. Electrical measurements were carried out for testing the operation of the devises without illumination (dark current measurements) revealing non – linear and symmetric I – V characteristics. The devices were also tested under illumination (photocurrent measurements) using a laser beam of wavelength λ = 405nm, where a non – linear photoresponse was measured as a function to incident laser power.

The second series of samples contains MoS_2 on glass substrate with symmetric Au metal electrodes. According the respective I – V characteristics (dark current) an ohmic – like behavior was observed. Under illumination a linear dependence of photocurrent to incident power was measured. From power dependence measurements responsivity at the order of nA/W was calculated and quantum efficiency was also extracted from the power of light incident to the area of the material (MoS_2).

Chapter 1 – Introduction

As field effect transistors (FETs) compose the main part of electronic applications, photodetectors and light emitting diodes (LEDs) are the dominant components of optoelectronic applications. The former involve the conversion of absorbed photons into electric signal, while the latter involve the conversion of injected electric current into light emission. Photodetection, which is the main subject of study in this thesis, is related to applications such as biomedical imaging, gas sensing, video imaging, and night vision.

Compared to three dimensional (3D) materials, two dimensional (2D) semiconductors provide great advantages in the performance of photodetectors due to their thickness dependent tunable band gaps, their mechanical flexibility and easy processing. These advantages revealing great potentials for photodetection make 2D materials very promising in optoelectronics. A significant amount of photodetectors based on different types of 2D materials have been demonstrated during the last decade with the first started with graphene which revealed excellent capabilities in photodetecting operations. Transition metal dichalcogenides (TMDs) are the most interesting component of the family of 2D materials, owning to sizable band gaps which result in lower dark currents and higher responsivity, are more attractive in optoelectronic applications compared to graphene. [1]

1.1 Introduction to transition metal dichalcogenide (TMD) nanosheets

The extended research on graphene – based devices and the absence of a band gap in its electronic band structure, which limits the operation of many electronic and optoelectronic devices, such as transistors and photodetectors, has led to the investigation of other materials with two – dimensional (2D) structure similar to graphene. Transition metal dichalcogenides (TMDs) have attracted the attention of research due to their remarkable electronic and optical properties suitable for nanoelectronic and optoelectronic applications.

TMDs exhibit a 2D layered (graphene – like) structure where the layers in bulk crystals, are joined together by van der Waals forces. They consist of MX_2 compounds, where M is a transition metal of group IV (Ti, Zr or Hf), group V (V, Nb, or Ta) or group VI (Mo or W), and X is a chalcogen (Se, S or Te) [2]. The different combinations of chalcogen and metal lead to more than 40 different types of TMDs. Some of the representatives are MoS_2, $MoSe_2$, WS_2 and WSe_2 [3]. Within each layer, a plane of transition metal atoms is sandwiched between two hexagonal planes of chalcogen atoms joined together via covalent bonds (Figure 1.2 a).

The band structure of TMDs depends on the number of layers. Bulk crystals have an indirect band gap which is transformed to direct band gap in the monolayer form. This direct band gap in single layer makes TMDs a very promising property for (opto)electronic applications. Figure 1.1 presents the periodic table of elements including the colored areas which correspond to the transition metals (M) and chalcogens (X).

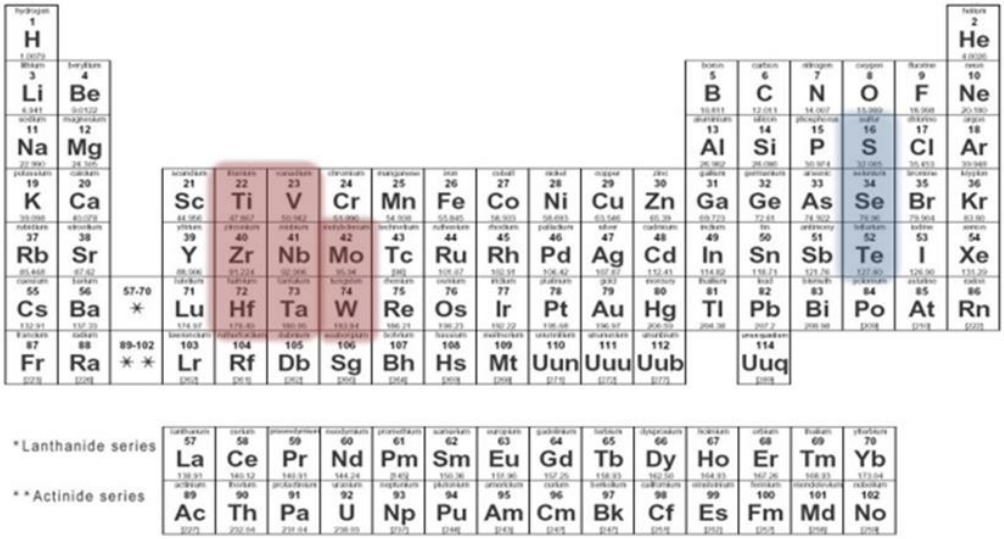

Figure 1.1 Periodic table of elements. The colored areas correspond to the transition metals (M) (purple) of groups IV, V, and VI and chalcogens (X) (blue).

1.2 Properties of Molybdenum disulfide (MoS_2)

The main representative of TMDs – Molybdenum disulfide (MoS_2) – has attracted significant attention in nanoelectronic and optoelectronic research in the recent years due to its unique physical, optical and electrical properties related to its 2D ultra – thin layer structure. In the following sections the general properties of MoS_2 will be further discussed.

1.2.1 Crystal structure

MoS_2 crystals possess a layered structure of S – Mo – S, with S and Mo atoms covalently bonded. The adjacent layers are joined together by weak van der Waals forces, as it has been described before for TMDs. In MoS_2 a hexagonal plane of Mo atoms is located between two hexagonal planes of S atoms, as shown in Figure 1.2 (a). Each Mo atom is positioned at the center of a triangular prism consisted of 6 S atoms. This tri – layer form is attributed to a monolayer of MoS_2 and it is stacked in three different formations leading to three different types of multilayer MoS_2, as shown in Figure 1.2 (b) which will be further discussed in the following section. [2]

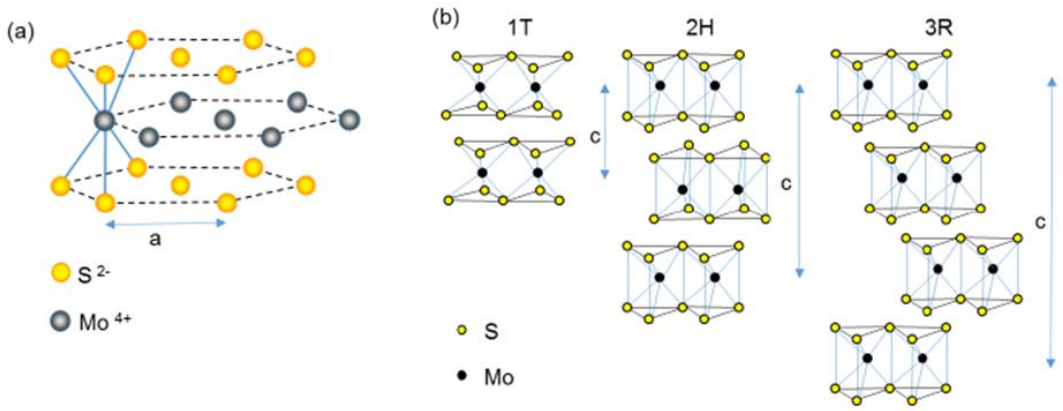

Figure 1.2: ***(a)*** *Structure of S and Mo hexagonal planes in monolayer MoS_2.* ***(b)*** *Side view of the three different configurations (1T, 2H, and 3R) of multilayer MoS_2. [2]*

The weak van der Waals interactions between the layers allow bulk MoS_2 to appear in different polytypes of structure. There are three common known structures – 1T, 2H, and 3R. Both 2H (H for hexagonal symmetry) and 3R (R for rhombohedral symmetry) structures have triangular prismatic coordination. The 2H – MoS_2 type contains two S – Mo – S units along the c axis and has hexagonal symmetry. The 3R structure has rhombohedra symmetry with three S – Mo – S units. In 1T – MoS_2 type (T for tetragonal symmetry) the upper triangle of S atoms is inversed to the bottom triangle which leads to a tetragonal symmetry. It has octahedral coordination with one S – Mo – S in the unit cell. [3]

Figure 1.3 (a) represents the top view of MoS_2 crystal structure which is similar to honeycomb structure of graphene. The interlayer distance is 6.5Å as it is shown in Figure 1.3 (b).

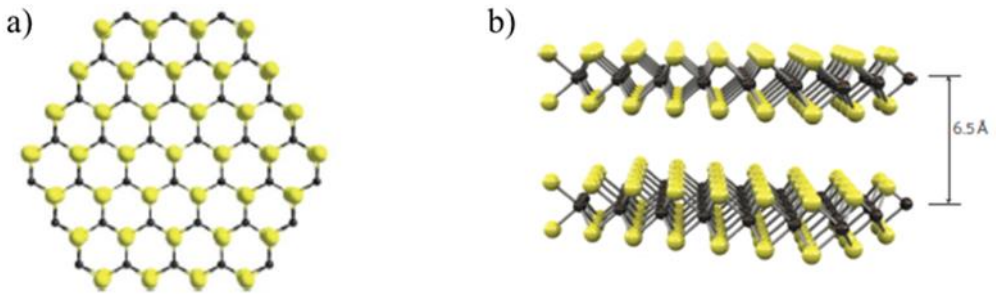

Figure 1.3: ***(a)*** *Top view of MoS_2 honeycomb structure. [4]* ***(b)*** *Schematic representation of interplanar spacing between two MoS_2 layers of 6.5Å. [5]*

1.2.2 Electronic band structure and optical properties

The band structure of 2D materials is affected and transformed by the quantum confinement effect. The position of the band edges can be changed as the thickness of the material decreases, thus a transition from indirect – to direct band gap occurs as we move from bulk to monolayer form. For bulk (and bilayer) MoS_2 the valence band maximum and the conduction band minimum are located at the Γ point and a point at the half distance between K and Γ respectively, as shown by the red arrow in Figure 1.4. This leads to an indirect band gap, E_g = 1.2eV for bulk MoS_2. In the case of monolayer both valence band maximum and conduction band minimum are located at the K point leading to a direct band gap of E_g = 1.9eV. [2], [6]

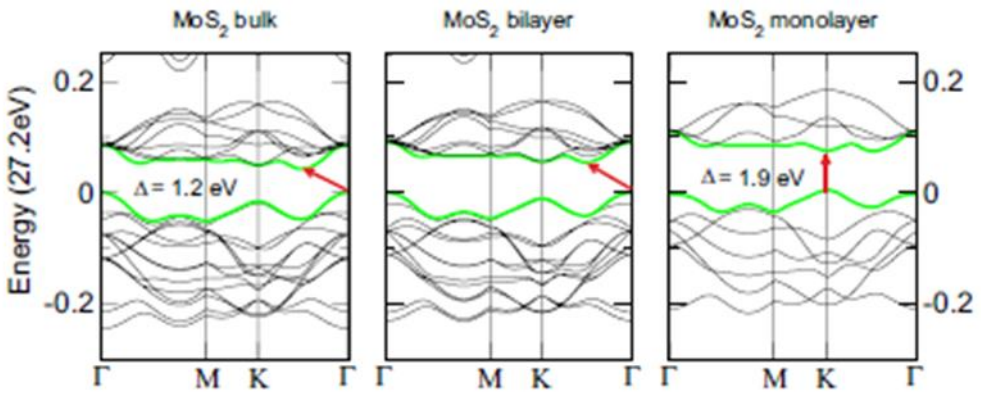

Figure 1.4: Band structure of bulk, bilayer, and monolayer MoS_2. The green lines correspond to the bottom of the conduction band and the top of the valence band. The red arrows show the smallest value of the band gap. [6]

This transition in the band structure has a significant impact on the optical properties in MoS_2. It has been investigated by absorption and photoluminescence (PL) spectra (Figure 1.5) [7]. Strong PL emission was observed in monolayer MoS_2 indicating the configuration of a direct gap semiconductor. This strong emission vanishes from monolayer to bulk crystal as a result of direct – to indirect gap transition, as shown in Figure 1.5(b).

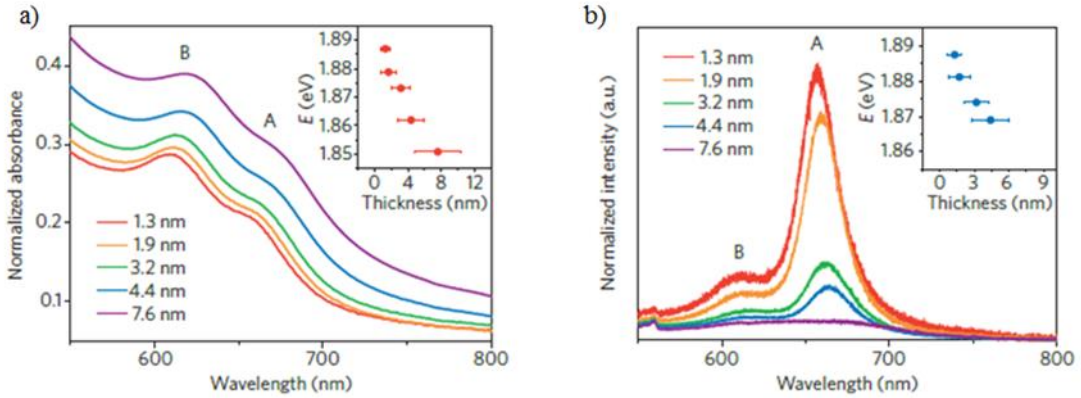

*Figure 1.5: **(a)** Absorption and **(b)** Photoluminescence spectra of MoS_2 with a range of layer thickness from 1.3 to 7.6nm. Insets for (a) and (b) depict the energy of the A exciton peak as a function of the layer thickness. [7]*

Two pronounced emission peaks can be observed in the optical absorption and photoluminescence spectrum at around 660 and 610nm, known as A and B excitonic transitions, respectively (green arrows in Figure 1.6). These two peaks originate from the direct transition at K point of the Brillouin zone between the maxima of split valence bands and the minimum of the conduction band. This splitting at the valence band maximum at the K point is associated with spin – orbit coupling in single layer MoS_2. [7], [8]

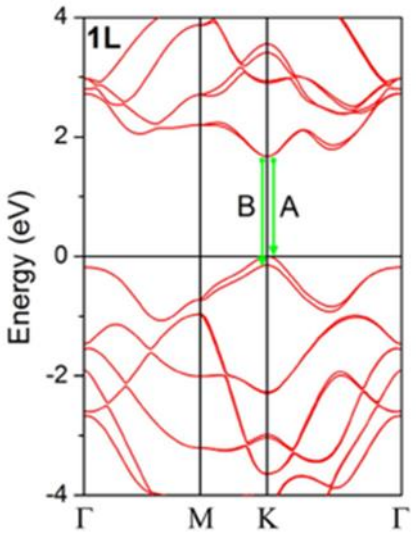

Figure 1.6: Band structure of monolayer MoS_2, calculated by density functional theory (DFT). The green arrows indicate the direct A and B excitonic transitions. [9]

1.2.3 Vibrational properties

An extended research has also been made in order to investigate the vibrational modes in MoS_2 crystal and in TMDs in general. A powerful tool for such a study is Raman spectroscopy. It is a non – destructive, fast and accurate method for research and characterization of MoS_2 properties. It provides structural and electronic information such as identifying the number of layers in a crystal which is the application of interest in this study. Raman spectroscopy will be further discussed in the next chapter (Section 2.1.2)

As it has already been mentioned (Section 1.2.1), bulk MoS_2 is made of chalcogen – metal – chalcogen (S – Mo – S) layers connected to each other via Van der Waals forces. The unit cell contains 2 metal (Mo) atoms and 4 chalcogen (S) atoms – 6 atoms in total – into two neighboring layers of bulk MoS_2. Every single atom has three degrees of freedom leading to 18 vibrational modes (phonon modes) in the unit cell, 3 of which are acoustic modes and 15 are optical modes. [3]

Among the 18 vibrational modes 4 are Raman – active modes i.e. doubly degenerate $2E_{2g}$ (E_{2g}^1 and E_{2g}^2), doubly degenerate E_{1g}, and A_{1g}. Here, the notation "E" is used for the modes that are doubly degenerate in the xy plane [3]. E_{2g}^2 mode corresponds to the vibration of an S – Mo – S layer on the opposite direction with respect to its adjacent layers. This mode has a very low frequency ($32cm^{-1}$) and cannot be detected through a typical Raman system due to the use of a filter with a cutoff edge of $\sim 100cm^{-1}$. The mode E_{1g} ($\sim 286cm^{-1}$) is absent in back – scattering Raman modulation with the laser beam propagating in the direction of the c – axis of the crystal. Thus, two dominant peaks, E_{2g}^1 at $383cm^{-1}$ and A_{1g} at $408cm^{-1}$, are observed in a typical Raman spectrum for bulk MoS_2 [10]. The first in – plane mode (E_{2g}^1) is attributed to the vibration of the two S atoms against the Mo atom while the second, out – of – plane mode (A_{1g}) is a result of the vibration of S atoms in opposite directions with respect to each other [11], as shown in Figure 1.7 (b).

The frequency of the two dominant peaks (E_{2g}^1 and A_{1g}) described above were found to be dependent on the thickness of the crystal. The frequency of the E_{2g}^1 mode increases (blue – shifting of $1cm^{-1}$) and A_{1g} mode decreases (red – shifting of $5cm^{-1}$) as the layer number decreases (Figure 1.7 a) [10], [12]. The changes of the peak position for these two modes from bulk to monolayer are attributed to the weakening of the Van der Waals force between the layers (for A_{1g} peak) and the changes in

structure or the Coulomb interaction among the layers (for E_{2g}^{1} peak), as the thickness decreases. [10], [11]

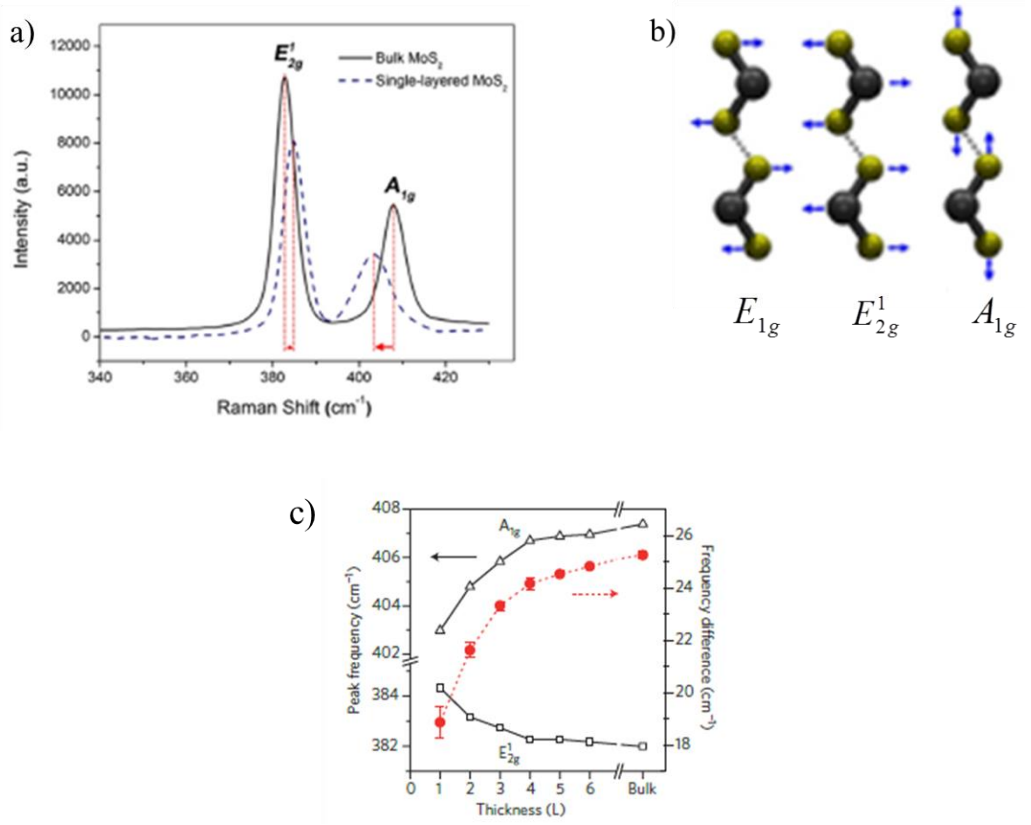

Figure 1.7: ***(a)*** *Raman spectra for bulk and monolayer MoS_2 flake in SiO_2 substrate with 514,5nm excitation wavelength. [12]* ***(b)*** *Representation of the three Raman active modes E_{1g}, E^{1}_{2g}, and A_{1g}. The black spheres correspond to the Molybdenum atoms and the yellow spheres to the Sulfur atoms. The blue arrays depict the orientation of the vibrations. [12]* ***(c)*** *The shifts in the position of E^{1}_{2g} and A_{1g} peaks of MoS_2 and the frequency difference of these modes (red spots) as function of layer thickness. [13]*

The widely used method for identifying the number of layers in MoS_2 crystals is through the calculation of the frequency difference of E_{2g}^{1} and A_{1g} i.e. $\Delta\omega$ ($A_{1g} - E_{2g}^{1}$). The value of $\Delta\omega$ ($A_{1g} - E_{2g}^{1}$) for monolayer MoS_2 was found to be~$19cm^{-1}$, for bilayer ~$21cm^{-1}$, and for bulk ~$25cm^{-1}$, as shown in Figure 1.7 (c). [13], [14]

1.3 Synthesis of 2D TMDs

As it has already been mentioned, monolayer and few – layered 2D TMD thin films exhibit remarkable properties making them attractive for the research community. Preparing such thin films with high quality is substantial for research and practical applications.

The initial attempt of making TMD thin films was mechanical exfoliation, the initial method for the development of graphene. [15] Due to the weak van der Waals forces between the layers, thin TMD flakes can be easily exfoliated from bulk crystals, using adhesive tape, which are then transferred to all forms of substrates. This process offers no impurities or defects and results in high quality flakes. [16] Thus mechanical exfoliation has been widely used for device fabrications. Nevertheless, TMD thin crystals developed by this method are small in size which is not suitable for the production of large size flakes owning uniform thickness needed for industrial scale applications. Alternative methods have been also employed in order to produce large scale monolayer and few – layered TMD nanosheets, such as chemical vapor deposition (CVD) method and liquid phase exfoliation. An optical image of a single – to multilayer MoS_2 flake by mechanical exfoliation is shown in Figure 1.8 (a). [17]

Concerning the liquid phase exfoliation method, individual sheets from TMD bulk crystals can be created by the use of organic solvents or aqueous solutions involved in the process. The interaction between the TMD material and the solvent with the simultaneous use of sonication breaks the weak van der Waals bonds leading to separation of the layers. Organic solvents often used for this method are, N – methyl – 2 – pyrrolidone (NMP), isopropanol or ethyl alcohol (used in this work) [16]. However, liquid – phase exfoliated flakes may exhibit different properties due to the adsorption of liquid species during the exfoliation process.

During the chemical vapor deposition (CVD) method, a precursor gas is flowing into a chamber which contains one or more heated objects for coating. Chemical reactions take place on the hot surfaces leading to the deposition of a thin film of the desired material, on the substrate. [18] A two – step MoS_2 CVD growth from a thin film of MoO_3 annealed in a sulfur environment is shown in Figure 1.8 (c). [19]

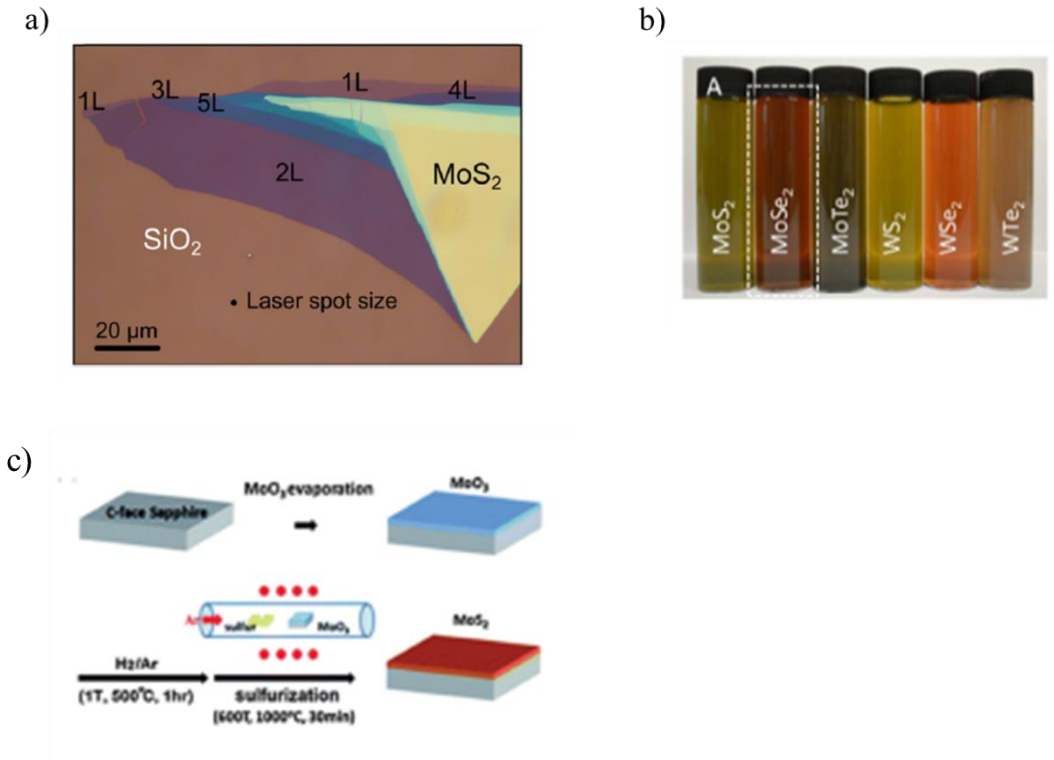

Figure 1.8: ***(a)*** *Optical image of a mechanical exfoliated MoS_2 flake from single – to multilayer on 285nm thick SiO_2.The number of layers (1L – 5L) is also depicted. [17]* ***(b)*** *Photograph of standard dispersions of all TMDs from group VI, in water/ sodium – cholate (SC). [20]* ***(c)*** *Two – step CVD process of MoS_2 growth from sulfurization of a thin MoO_3 film. The first step is the annealing of MoO_3 film in H/Ar environment followed by the second step of annealing in a sulfur environment. [19]*

Even though mechanical exfoliation results in good quality nanoflakes with negligible defects, CVD method, offering a large – scale growth of TMD flakes with uniform thickness, regular shape, and high purity is considered as a reliable and promising tool for preparing high quality TMD layers and other 2D materials.

1.4 Device applications based on MoS_2

A variety of electronic and optoelectronic applications based on MoS_2 have been made and studied the recent decades. A series of these applications will be presented and discussed in the following sections.

1.4.1 Electronic applications based on MoS_2

Field effect transistor (FET) is one of the most fundamental components of electronic applications. The basic features of a FET structure are a semiconductor channel region which is connected to the source and drain electrodes. The device also contains a gate electrode which is separated from the channel by a dielectric layer. The conductivity of the channel can be modulated by the gate electrode which controls the current that flows between the source and drain electrodes. [13]

Desirable properties for FETs are high conductivity, high on/off ratio (the ratio of on – state to off – state conductance) and high charge – carrier mobility which leads to fast operation. The stunning properties of two – dimensional graphene such as the high carrier mobility have attracted the attention of research for the last decades, but the absence of a band gap limits the operation of graphene – based FETs. This drawback has led researchers to investigate alternative 2D materials with properties similar to graphene but with a sizable band gap. [13]

2D TMDs with tunable band gaps, extreme thinness, structural stability and ease in fabrication are suitable for channel materials in FETs. Concerning the MoS_2 FETs, B. Radisavljevic *et al.* [5] first reported, in 2011, a top – gate transistor with a single layer MoS_2 as the conductive channel. It showed an excellent current on/off ratio of 10^8, n – type conduction and high room – temperature mobility at least 200 $cm^2\ V^{-1}\ s^{-1}$. In this work, 30nm hafnium dioxide (HfO_2) dielectric was used (Inset of Figure 1.9 a), which led to the improvement of the field – effect mobility of the device.

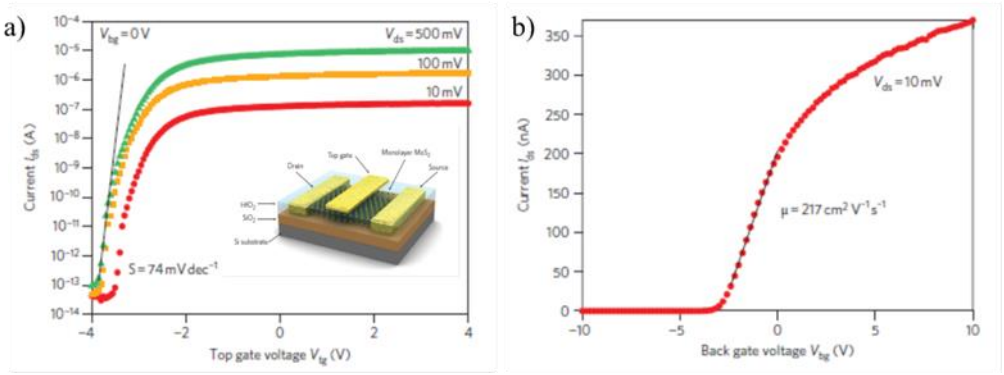

Figure 1.9: ***(a)*** *I_{ds} – V_{tg} curves for a bias voltage range from 10mV to 500mV. The back gate is grounded and the measurements are performed at room temperature. For V_{ds} = 10mV the I_{on}/I_{off} ratio is > 1×10^6 and for V_{ds} = 500mV, the I_{on}/I_{off} ratio is > 1×10^8. Inset: Schematic view of the MoS_2 transistor.* ***(b)*** *Transfer characteristic for monolayer MoS_2 transistor with V_{ds} = 10mV at room temperature. Back – gate voltage V_{bs} is applied to the substrate and the top – gate is disconnected. The device exhibits a field – effect mobility of ~217 cm^2 V^{-1} s^{-1}. [5]*

In 2012, S. Das and co – workers [21] reported a really enhanced value of field – effect mobility of 700 cm^2 V^{-1} s^{-1} at room temperature for a back – gated transistor based on multilayer MoS_2. This value was achieved by the use of Scandium (Sc) as low work function metal contacts on 10nm thick MoS_2 flakes covered by a layer of Al_2O_3 dielectric, with a 15nm thickness.

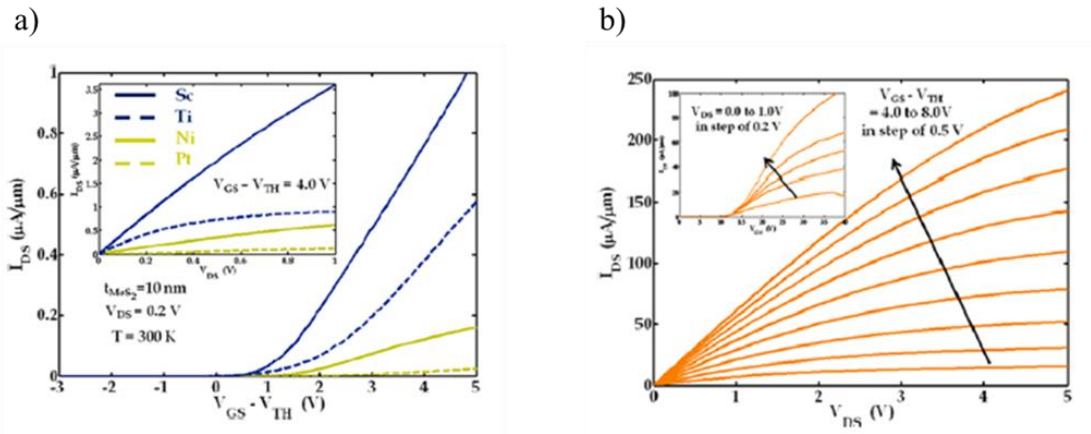

Figure 1.10: ***(a)*** *Transfer characteristics of 10 – nm thick MoS_2 back – gated transistor for Pt, Ni, Ti, and Sc metal contacts for V_{DS} = 0.2V at T = 300˚C. Inset: The output characteristics of the corresponding devices for a gate voltage overdrive of 4.0V – 5.0V.* ***(b)*** *Output characteristics of MoS_2 transistor with 15- nm thick Al_2O_3 dielectric for different gate voltages. Inset: Transfer characteristics of the same device for different drain voltages. [21]*

Figure 1.10 (a) indicates the transfer characteristics for the 10 – nm thick MoS_2 transistor using Pt, Ni, Ti, and Sc as the metal contacts. The field – effect mobility for Sc metal contact reaches the highest value of 184 cm^2/ (V s), compared to the corresponding values extracted for the other metal contacts. This fact indicates the importance of using the proper metal contacts in order to exploit the intrinsic properties of such materials for optimum device operation. The field – effect mobility for this device, has been increased from 184 to 700 cm^2/ (V s) with the use of Al_2O_3 dielectric, as it was extracted by the measurements shown in Figure 1.10 (b).

1.4.2 Optoelectronic applications based on MoS_2

According to advantages like low dimensionality, large direct band gaps which match the visible spectrum and strong photoluminescence, 2D TMDs have been attractive materials for various optoelectronic applications. The illumination of photons with energy greater than the band gap of a semiconductor results in photocurrent generation upon the separation of photogenerated electron – hole pairs by an applied or built – in field. [22], [23] Various applications for light detection based on TMDs have been made in the recent years, but we will focus on optoelectronic devices based on MoS_2. Phototransistors (applied field) and photodiodes (built – in field) are two of the main components in photodetection designs, and will be discussed in the following section.

Phototransistors

In phototransistors, the 2D TMD material is acting as a semiconducting channel, where incident light is absorbed and converted into current. A crucial parameter for the performance of a phototransistor is the responsivity which is defined as $R = I_{ph}/P_{light,}$ (in A/W) where I_{ph} is the photocurrent generated and P_{light} is the power of incident light. (see section 1.5)

The first phototransistor based on mechanically exfoliated monolayer MoS_2 was reported by Z. Yin *et al.*(2012) [24], who evaluated a responsivity of ~ 0.42 mA/W at zero gate voltage which reaches at 7.5mA/W when the gate voltage was set at ~50V (Figure 1.11 c).

The aforementioned device exhibited a rapid photoswitching (photocurrent generation and annihilation) between illumination (ON) and under dark (OFF) states within 50ms as shown in Figure 1.11 (b).

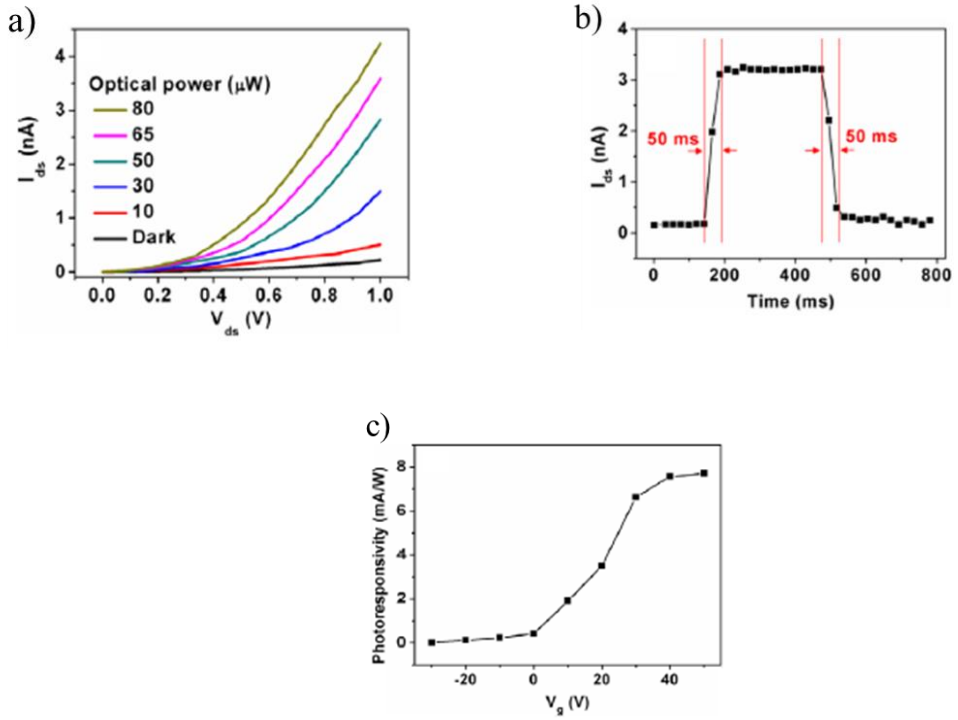

Figure 1.11: ***(a)*** *Output characteristics of phototransistor at the range of 10 - 80μW of incident optical power, at V_g = 0.* ***(b)*** *Photoswitching test with the duration of 50ms between ON (under illumination) and OFF (in dark) states of single – layer MoS_2 phototransistor at V_{ds} = 1V and P_{light} = 80μW.* ***(c)*** *Photoresponsivity as a function of the gate voltage at V_{ds} = 1V and P_{light} = 80μW. [24]*

Another work was reported by Woong Choi *et al.* [25], in 2012. They fabricated a phototransistor with a multilayer MoS_2 channel (layer thickness ~ 60nm) on a silicon substrate with an Al_2O_3 dielectric of 50nm thickness in between (Figure 1.12 a). Responsivity at a range of 50 – 120 mA/W, for visible light, was calculated in this work (Figure 1.12 b).

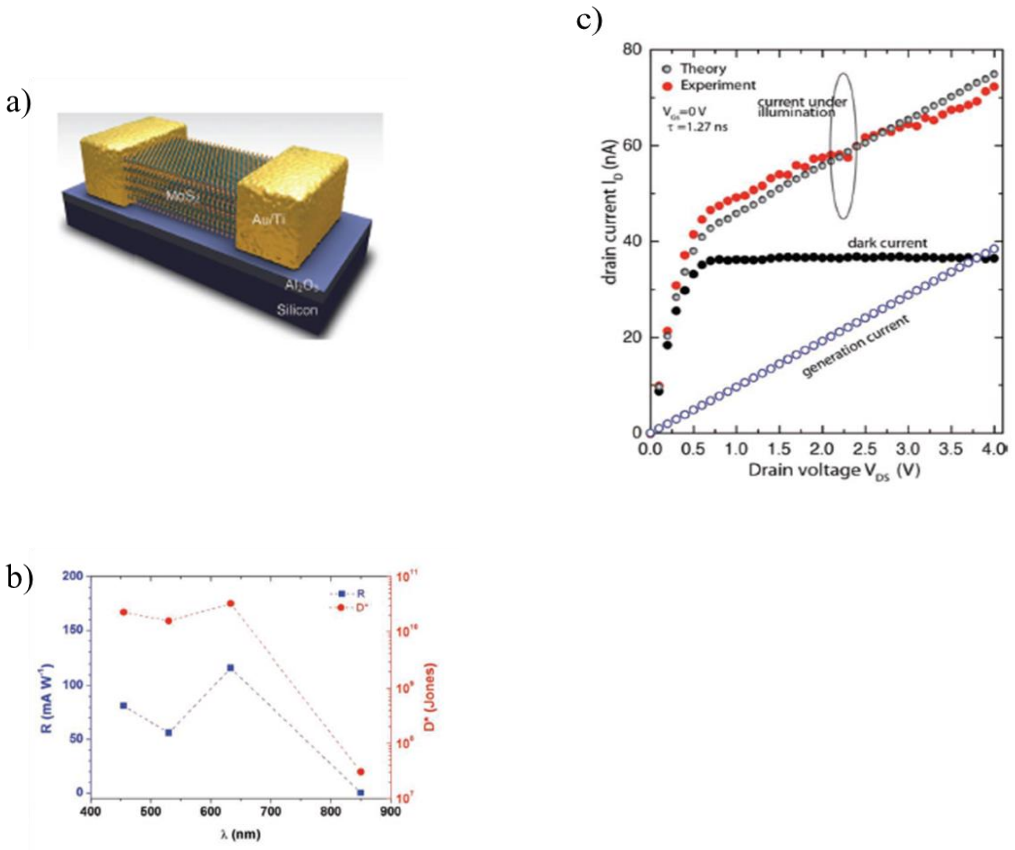

Figure 1.12: ***(a)*** *Three - dimensional representation of multilayer (~60nm thickness) MoS_2 phototransistor.* ***(b)*** *Responsivity and specific detectivity at different wavelengths.* ***(c)*** *Comparison between theoretical and experimental measurements for drain current under illumination. [25]*

In 2013, an ultrasensitive phototransistor based on monolayer MoS_2 was demonstrated by Oriol Lopez - Sanchez *et al.* [26], with a calculated responsivity reaching at 880 A/W under illumination with a laser beam of 561nm in wavelength. An exfoliated MoS_2 monolayer was deposited on a Si/SiO_2 (270 nm thickness) with 90 – nm – thick Au electrodes on top (Figure 1.13 a). A monotonous decrease in photoresponsivity was observed with increasing incident laser power, as shown in Figure 1.13 (c), which can be attributed to the presence of trap states either in MoS_2 or at the MoS_2/substrate interface leading to saturation of the photoresponce. A short gate pulse with a brief increase from – 70V to 0V led to an improvement in the response time of the device, as shown in Figure 1.13 (b).

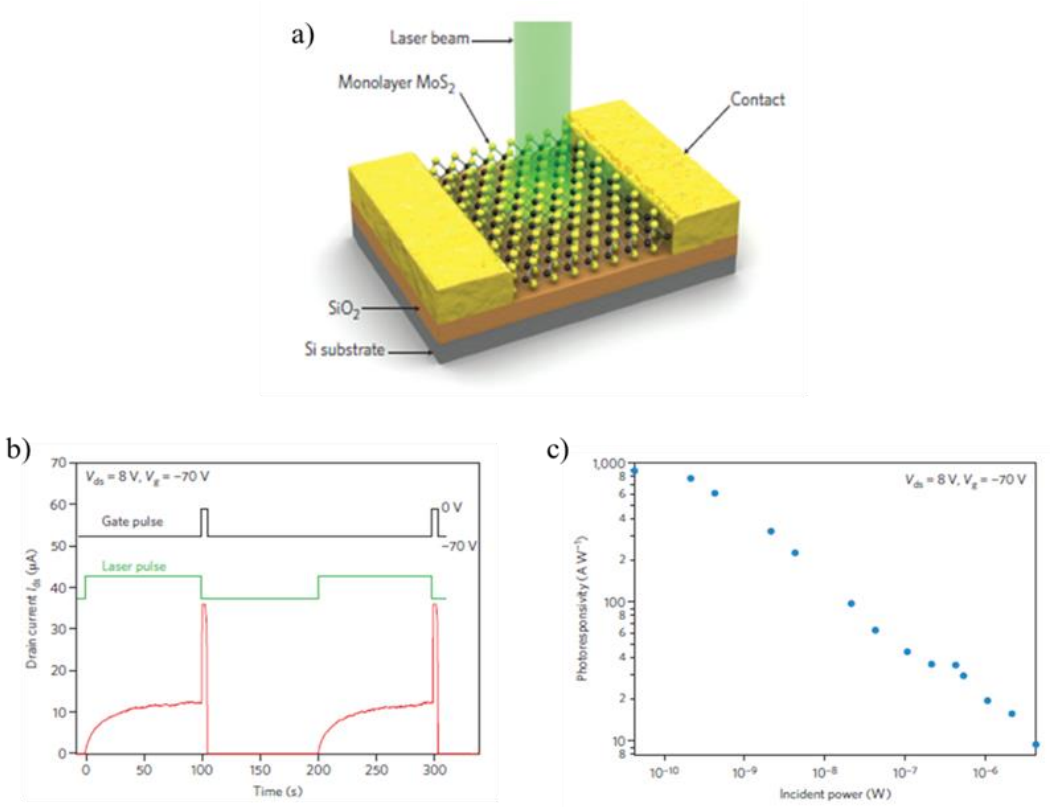

Figure 1.13: ***(a)*** *Schematic view of the monolayer MoS_2 based phototransistor.* ***(b)*** *Time – resolved photoresponse of MoS_2 phototransistor (red curve) to an incident power of 0.425μW with a voltage pulse from -70V to 0V at the gate electrode. The photocurrent decay time was decreased to less than 0.6s.* ***(c)*** *Photoresponsivity as a function of incident power. The device showed a maximum photoresponsivity of 880A/W for 150pW illumination power with a monotonous decrease with increasing the incident power due to the presence of trap states either in MoS_2 or at the interface between MoS_2 and the substrate. [26]*

- *Photodiodes*

In phototransistors, an external electric field is required by applying a source – drain bias in order to separate the optically generated electron – hole pairs. On the other hand, in photodiodes the photogenerated carriers can be separated by a built – in (internal) electric field in the active area of the device. This is called the *photovoltaic effect*. [22] This built – in electric field is achieved by p – n junctions, semiconductor – metal Schottky junctions or heterojunctions between two different semiconductors. [22], [23]

A few – layered MoS_2 photodetector was demonstrated by D. Tsai *et al*, [27] in 2013. The fabrication of the device was based on metal – semiconductor – metal (M – S – M) geometry (Figure 1.14 a) using Au electrodes as Schottky contacts. A responsivity of 0.57A/W was reported with a laser beam of 532nm wavelength used for illumination. The rise time (OFF to ON state) and fall time (ON to OFF state) were estimated to be 70 and 110μs, respectively, as shown in Figure 1.14 b. These fast photoresponse times were attributed to the large electric field yielding at the Schottky MoS_2/Au barrier, as well as to the inter – digitated electrode pattern which can lead to an enhanced collection of photocarriers and faster response speed.

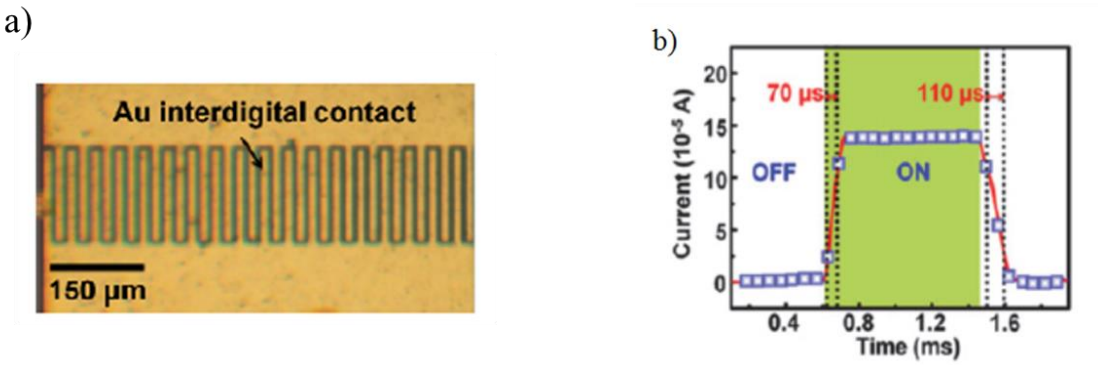

Figure 1.14: ***(a)*** *Optical microscope top – view image of the few – layered MoS_2 M – S – M photodetector.* ***(b)*** *Time response of MoS_2 photodetector where the rise (70μs) and fall (110μs) times are presented. [27]*

N. Lopez *et al.* [28], in 2014, fabricated a photosensor based on monolayer MoS_2 in triangular form (Figure 1.15 a), grown by CVD method (see section 1.3) with Ti electrodes. The device exhibits a maximum responsivity of 1.1mA/W under a 514.5 nm excitation wavelength, as shown in Figure 1.15 c.

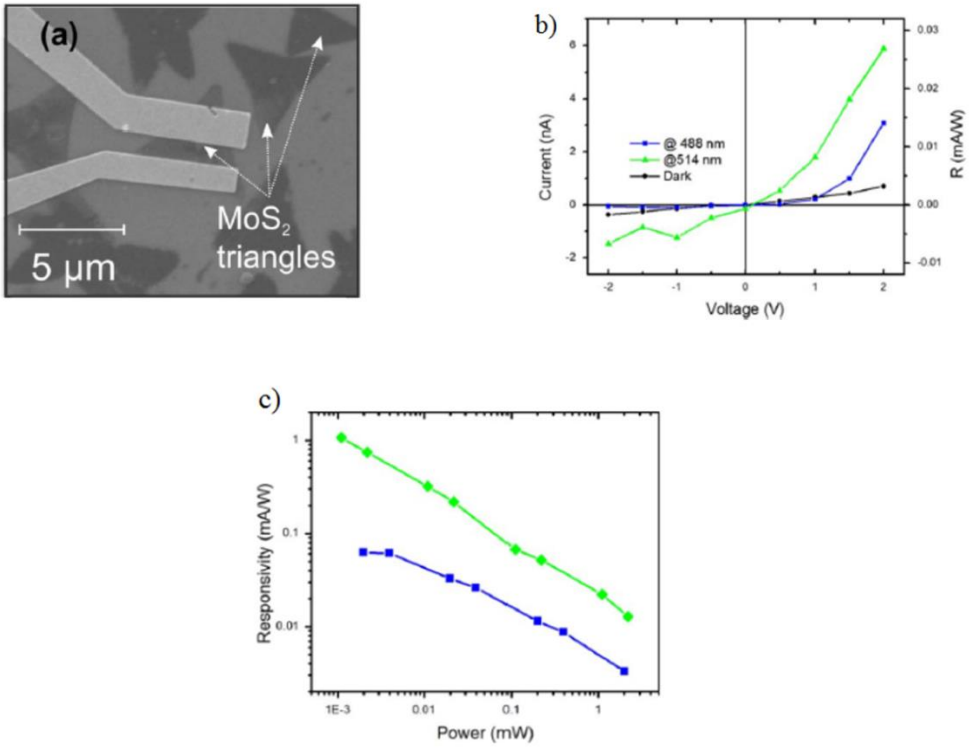

Figure 1.15: ***(a)*** *SEM image of the triangular MoS_2 monolayers with Au/Ti electrodes.* ***(b)*** *I – V curves of the device without illumination (darkness) and under illumination with two different excitation wavelengths (488 and 514nm) depicted with blue and green color, respectively. The power of both wavelengths was 0.22mW.* ***(c)*** *Responsivity as a function of incident laser power for both 488 and 514 nm, with a constant bias at 1.5V. [28]*

A few – layered MoS_2 photodetector was demonstrated, in 2015, by S. Ghosh *et al*. [29] The MoS_2 flakes were produced by liquid phase exfoliation method (see section 1.3) and deposited on pre – fabricated inter – digitated Pt electrodes on borosilicate glass substrate. A responsivity of 0.14mA/W was obtained under laser excitation power of 60mW with 20V applied voltage as shown in the inset of Figure 1.16 a.

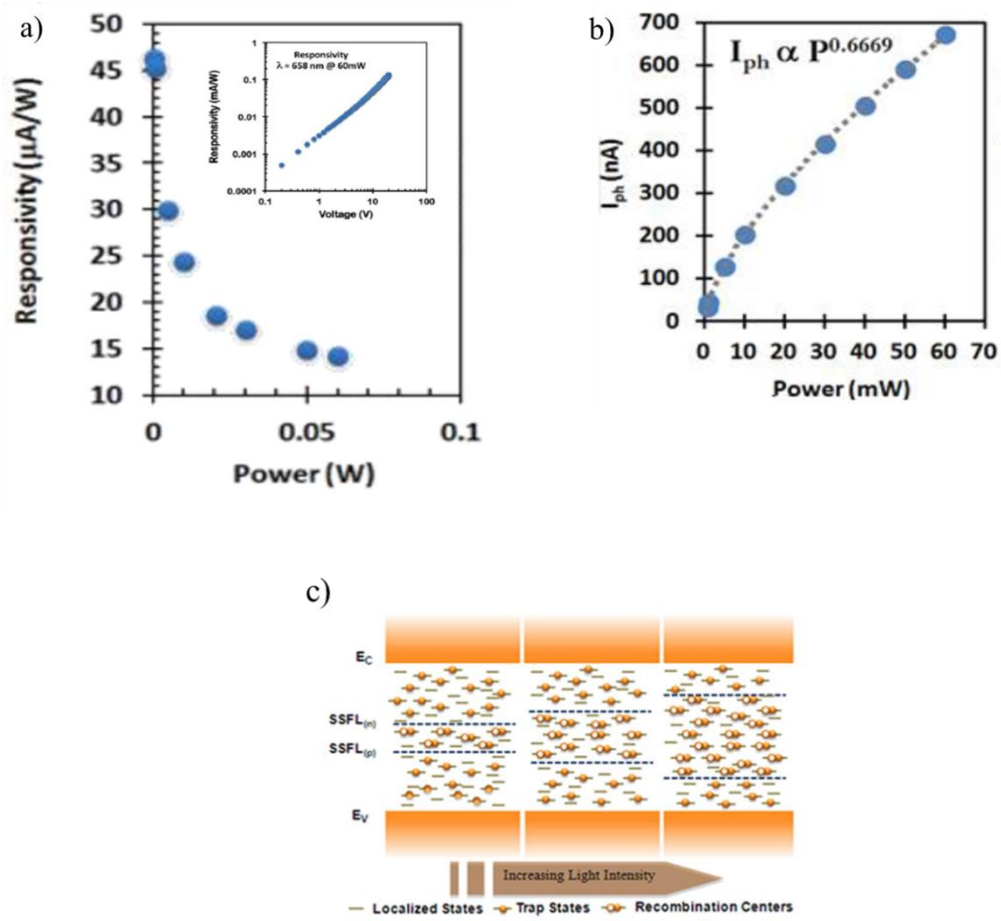

Figure 1.16: ***(a)*** *Responsivity and* ***(b)*** *Photocurrent as a function of incident laser power with a laser beam of wavelength λ = 658nm. Inset: Responsivity as a function of applied voltage with incident laser of λ= 658 nm and power 60mW.* ***(c)*** *Schematic representation of the shift of Steady State Fermi Levels as the light intensity increases. [29]*

A fractional dependence of photocurrent and a reduction of the responsivity were observed, as a function of incident laser power. These facts attributed to the presence of trap states within the liquid exfoliated MoS_2 flakes. The states that are laying between the steady state Fermi levels for electrons ($SSFL_{(n)}$) and for holes ($SSFL_{(p)}$) act as recombination centers (the free carriers falling into that centers will recombine and will not contribute to the conduction of the channel) and they move apart as the light intensity increases, as shown in Figure 1.16 c. As a result, the number of recombination center increases causing a reduction in the lifetime of free carriers, thereby resulting in a sub – linear dependence of photocurrent and a reduction of the responsivity as the incident power increase (Figure 1.16 a, and b).

The presence of these trap states may arise due to the random orientation of the stacked MoS_2 layers produced by the liquid – phase exfoliation method.

Metal contacts have a crucial role for the operation of the device. If both electrodes are made of the same metal, the profile of the built – in electric field in the channel between the two adjacent electrodes is symmetric. This leads to a zero total photocurrent and an external bias is needed to drive the free carries in one direction within the channel. Thus, using different metal contacts (asymmetric metallization) the mirror symmetry of the built – in electric field of the channel breaks giving rise to an overall photocurrent. This can be achieved by applying one Schottky and one Ohmic contact at the metal/semiconductor interface. This asymmetric metallization was employed on the first photodetector based on graphene, and led to an enhancement of photocurrent, allowing for more efficient photodetection. [30]

In 2013, M. Fontana and his collaborators [31] fabricated a multilayer MoS_2 transistor with two Pd electrodes and one Au electrodes as the metal contacts of the device, in order to investigate the impact of different contact material on the performance of the device. The current values as a function of source – drain voltage for one Pd and one Au electrode used as source and drain contacts, are presented in Figure 1.17 a.

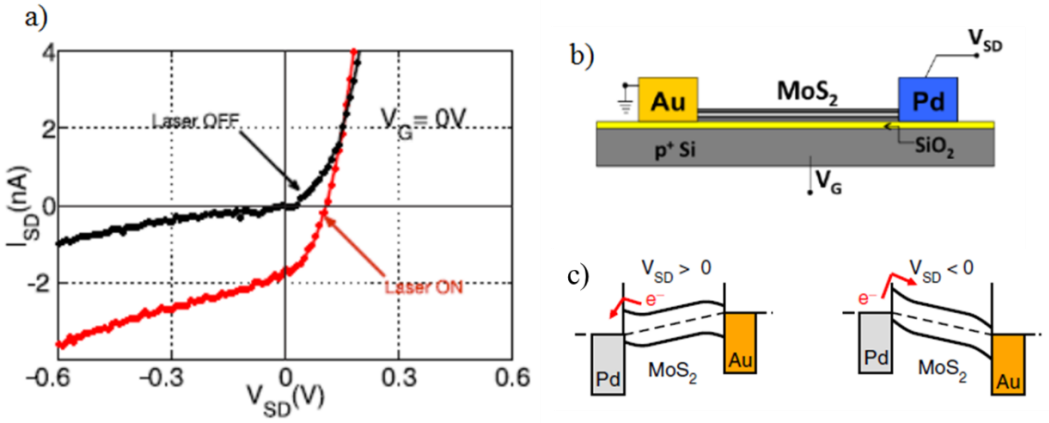

Figure 1.17: ***(a)*** *Current as a function of source – drain voltage at V_G = 0 for one Pd and one Au contact.* ***(b)*** *Schematic of the device with Pd – Au configuration.* ***(c)*** *Schematic band alignment for one Pd and one Au metal contact with the effect of source – drain bias. [31]*

The device shows an asymmetric diode – like behavior for the Pd – Au configuration at $V_G = 0$. Under illumination with a 532nm laser beam, electrons from Pd are photo – excited over the Pd/MoS_2 barrier and electron – hole pairs are created and separated by the built – in electric field at the contacts. Electrons accumulate at the Au electrode and hole at the Pd electrode giving rise to an open circuit voltage, $V_{OC} = 0.1V$ (red curve in Fig. 1.17 a), a clear evidence of the photovoltaic effect. For positive bias at the Pd contact, the barrier for electrons propagating from MoS_2 to Pd is reduced (left image of Figure 1.16 c) resulting in an exponential increase in current under $V_{SD} > 0$. The current is limited, for $V_{SD} < 0$, due to electrons thermally excited over the barrier from Pd to MoS_2, as shown in the right image of Figure 1.17 c.

Regarding the Pd – Pd bias configuration (Figure 1.18 b), the curves show more symmetric behavior as a function of source – drain bias voltage. This is due to the symmetric built – in electric field at the two ends of the channel (Figure 1.18 c), where the carriers are accelerated in opposite directions resulting in no charge separation and in zero open circuit voltage ($V_{OC} = 0$), as shown in Figure 1.18 a.

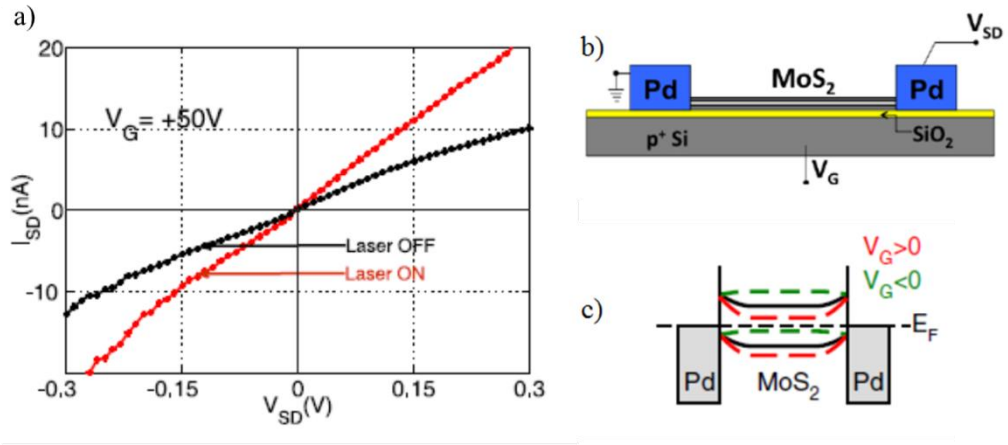

Figure 1.18: ***(a)*** *Current as a function of source – drain voltage at V_G = 0 for two Pd contacts.* ***(b)*** *Schematic of the device with Pd – Pd configuration.* ***(c)*** *Schematic band alignment for two Pd metal contacts with the shift in bands by applying a gate voltage. [31]*

The following table (Table 1) summarizes the main parameters (responsivity and response time) of device performance for MoS_2 based photodetectors reported so far. The responsivities for the various photodetectors spread over a wide range from 0.09mA/W up to 880A/W which is not surprising due to the different forms of MoS_2, fabrication processes and electrode materials that are used. This variation has already been observed among all the applications described so far. [1]

Table 1: Device Performance of MoS_2 based Photodetectors [1]

Year	Description	Responsivity	Response time	Wavelength
2012	Monolayer	7.5mA/W	< 50ms	~670nm
2012	Multilayer	50-120 mA/W for visible, 0.09mA/W for infrared		450-850nm
2013	Monolayer	880A/W (150pW, V_{ds} = 8V, V_g = -70V	< 0.6s (with reset voltage pulse)	561nm
2013	Few - layer	0.57A/W	70µs rise time 110µs fall time	532nm
2014	Monolayer	~50A/W, V_{ds} = 6V	< 1ms at low temperature	640nm
2014	Monolayer	1.1mA/W		514.5nm
2015	Monolayer	3.5A/W, V_g = -40V, V_{ds} =10V		532nm
2015	Thin films	~50µA/W to~0.1mA/W	~few ps	658nm
2015	Monolayer		3-5ps fast component 80-110ps slow component	452nm
2015	Monolayer	5.5mA/W(1T) 0.2mA/W(2H)		440nm
2015	Multilayer bottom – gate TFT	342.6A/W (V_g = 8V, V_{ds} = 1V, incident power density = 2mW/cm^2)		532nm
2016	Monolayer	3.07mA/W	≤few ms	633nm

1.5 Figures – of – merit for photodetectors

Photodetection is a process where light signal is converted to electric signal. It involves light (photon) absorption, generation of electron – hole pairs and charge carrier transport to respective electrodes. A set of figures – of – merit is commonly used in order to compare photodetectors based on different principles and composed of different materials, and geometries. In this section, an introduction to the meaning of the main figures that have been used in this work will be discussed.

- ***Responsivity, R***

Responsivity is the ratio of photocurrent to the total incident optical power on the photodetector, expressed in amps/Watt (A/W) and defined as

$$R = \frac{I_{ph}}{P_{inc}}$$

where I_{ph} is the generated photocurrent and P_{inc} the incident optical power (of a laser beam used in our work). Responsivity indicates the electric signal that can be attained from the detector at a certain incident power. [32], [33] For linear dependence of photocurrent as a function of incident power, responsivity is constant and can be extracted by the slope of the power dependence graph. Deviations from linearity can be caused by other mechanisms such as the existence of trap states within the material as it has already been observed in previous works [28].

- ***External Quantum Efficiency, (EQE)***

Quantum efficiency is one of the most important parameters used for the estimation of the quality of photodetectors. External quantum efficiency is the ratio of the number of photogenerated carriers (n_e) to the total number of incident photons ($n_{photons}^{total}$), defined as

$$EQE = \frac{n_e}{n_{photons}^{total}} = \frac{I_{ph}}{q \cdot \phi} \text{ (dimensionless)}$$

where I_{ph} is the photocurrent, q is the unit electron charge and φ is the photon flux, defined as the number of incident photons per second

$$\phi = \frac{P}{E_{ph}} \text{ (photons/sec)}$$

where P is the power of incident light and E_{ph} is the energy of a single photon. EQE > 1 means that more than one electron – hole pairs are created per incident photon. [32], [33]

- ***Internal Quantum Efficiency, (IQE)***

The internal quantum efficiency is the ration of the number of photogenerated carriers (n_e) to the number of the absorbed photons ($n_{photons}^{abs}$)

$$IQE = \frac{n_e}{n_{photons}^{abs}} = \frac{I_{ph}}{q \cdot \phi_{abs}} \text{ (dimensionless)}$$

where ϕ_{abs} is now the number of absorbed photons per second. According to this parameter photon losses due to reflection and transmission are taken into account. IQE is greater than EQE since in the latter all the impinging photons are assumed to be absorbed (reflected and transmitted photons are not counted). [32]

The aforementioned parameters will be evaluated and discussed in more details in chapter 3.

Chapter 2 – Experimental techniques

2.1 Experimental techniques for optical characterization

Two techniques were employed for the characterization of deposited MoS_2 flakes, in this thesis, i.e. Scanning electron microscopy and Raman spectroscopy which will be discussed in details in the following sections.

2.1.1 Scanning Electron Microscopy (SEM)

Scanning electron microscopy is a method for high-resolution imaging of surfaces. The scanning electron microscope involves a focused beam of high-energy electrons in order to generate the image of a sample in a similar way with visible light used in an optical microscope. The electrons interact with atoms of the sample producing various signals. These signals can be detected revealing information about the topography and composition of the sample's surface. In SEM a beam of incident electrons is generated in a column above the sample and is focused to a spot at the order of few nanometers in diameter by a series of lenses included in the column. The focused beam is then positioned onto the sample with the use of scanning coils near the bottom of the column and a raster scan is achieved for imaging.

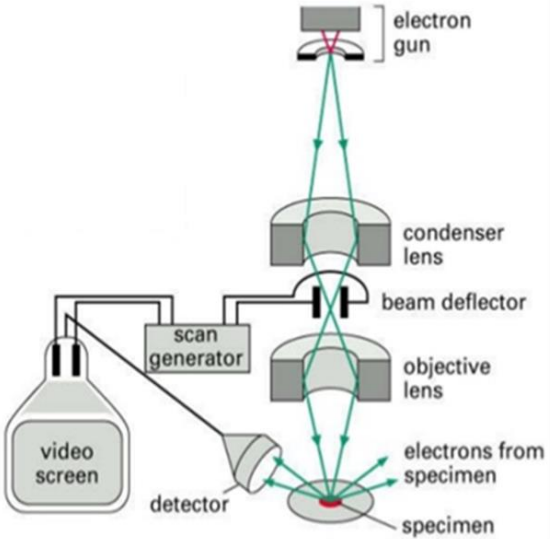

Figure 2.1: The main components of SEM. [34]

When the incident electrons interact with the sample, the electrons lose energy which is dispersed as a variety of signals. These signals contain backscattered electrons (by elastic scattering), secondary electrons (by inelastic scattering), photons (X-rays), visible light, transmitted electrons and heat. Each of these signals can be detected by specialized detectors. Figure 2.1 represents the main components included in the experimental set - up of SEM. Figure 2.2 represents the result of the interaction between the electron beam and the specimen.

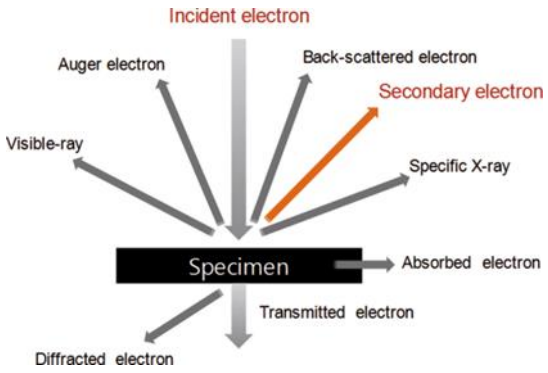

Figure 2.2: Electron – sample interaction in SEM [35]

The most common imaging modes include secondary electrons (topography) and backscattered electrons (composition) for SEM images. Diffracted backscattered electrons can also be used to determine the crystallographic structure of the sample. [36], [37]

2.1.2 Raman Spectroscopy

- *Introduction*

Raman spectroscopy is a spectroscopic technique used for the research and study of the rotational, vibrational and other low- frequency modes in molecules, ions and crystals. It is based on inelastic scattering coming from the interaction of incident radiation with molecular vibrations. Inelastic scattering of sunlight was observed in 1928 by the Indian scientist Sir C. V. Raman in the honor of whom it was named the Raman effect. [38]

Raman spectroscopy is a versatile tool which provides useful information about chemical identification, molecular structure characterization, effects of bonding and stress on a sample. It can be used to study solid, liquid and gaseous samples.

- *Origins of Raman spectra*

In Raman spectroscopy, the sample is illuminated with monochromatic light, usually from a laser beam at the range of visible, near infrared or near ultraviolet. When photons of the beam interact with the molecules of the sample, they have a possibility to be adsorbed or they might be scattered in all directions, or may not interact with the sample and pass through it. The main part of the scattered radiation has a frequency equal to the frequency of the incident radiation (elastic scattering) which constitutes Rayleigh scattering. A small portion of scattered radiation has different frequency from that of incident radiation (inelastic scattering) which constitutes Raman scattering. [38] It is the shift in frequency of the scattered photons, in inelastic scattering which is used to construct the Raman spectrum and provides information about the molecular vibrations of the material under investigation.

In Raman scattering the laser beam can be considered as an electromagnetic wave. The electric field of the electromagnetic wave can be described by the following equation:

$$\vec{E} = \vec{E}_0 \cos(2\pi \nu_{las} t) \qquad (2.1)$$

where E_0 is the amplitude of the electric field and ν_{las} is the frequency of the laser beam.

When the laser beam interacts with the sample it excites molecules and transforms them into oscillating dipoles which form a short – lived state called "virtual state". This state is unstable with subsequent re-emission of a photon.

When a diatomic molecule is illuminated, dipole moment is induced and given by

$$P = \alpha E = \alpha_0 E \cos(2\pi \nu_{las} t) \qquad (2.2)$$

where α is a constant called polarisability. For the molecular vibration the displacement q of the nuclei is written

$q = q_0\cos(2\pi\nu_{vib}t)$ (ν_{vib} is the vibration frequency) (2.3)

where q_0 is amplitude of vibration. Polarizability α can be written, for small amplitude of vibration, as a function of q:

$$a(q) = a_0 + \left.\frac{\partial a}{\partial q}\right|_{q_0} \cdot q + ... \tag{2.4}$$

By inserting (2.1) and (2.4) into (2.2) the dipole moment can be finally written as

$$P = a_0 E_0 \cos(2\pi\nu_{las}t) + \frac{1}{2}\left.\frac{\partial a}{\partial q}\right|_{q_0} \cdot q_0 E_0 \left[\cos(2\pi(\nu_{las} + \nu_{vib})t) + \cos(2\pi(\nu_{las} - \nu_{vib})t)\right] \tag{2.5}$$

The first term in Eq. (2.5) predicts a dipole with light emission at the same frequency as the frequency of the incident light, ν_{las} (Rayleigh scattering), while the second term determines inelastic ($\nu_{las} \pm \nu_{vib}$) Raman scattering. Raman scattering occurs only if $\left(\frac{\partial a}{\partial q} \neq 0\right)$ i.e. the vibrations change polarisability. [39], [40]

A Raman spectrum is a plot of intensity vs. Raman shift. The latter is the vibrational frequency ν_{vib} shift from the incident light frequency ν_{las} i.e. $\Delta\bar{\nu} = \bar{\nu}_{las} \pm \bar{\nu}_{vib}$, where, $\bar{\nu}$ is the wavenumber defined by

$$\bar{\nu} = \frac{\nu}{c} = \frac{1}{\lambda}\ (\text{cm}^{-1}) \tag{2.6}$$

where c is the velocity of light ($c = 3\cdot10^{10}$ cm/s) and λ is the wavelength (in centimeter units).

The $\nu_{las} - \nu_{vib}$ line corresponds to the frequency of the scattered photon coming from the molecular relaxation to a higher vibrational state than the initial ground state and corresponds to the so-called *Stokes* shift. On the other hand if the molecule relaxes to a lower vibrational state than the initial excited state, the scattered photon

has a frequency of $\nu_{las} + \nu_{vib}$ which corresponds to the so – called *anti – Stokes* shift. [39]

In Figure 2.3 the basic processes that occur in one vibration are presented.

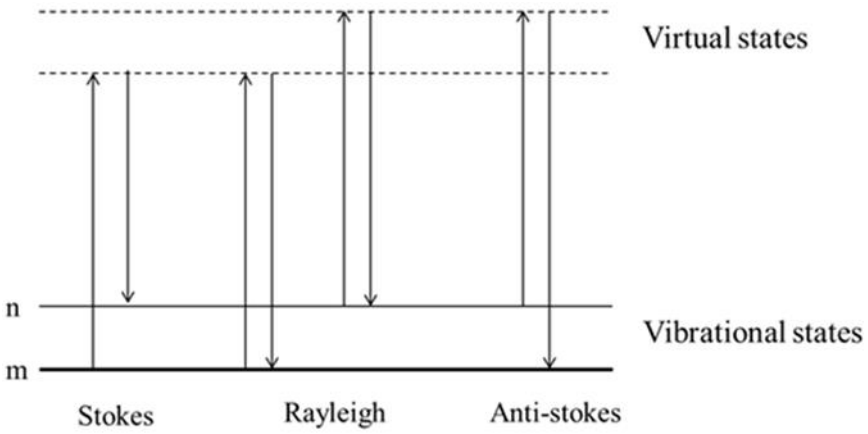

Figure 2.3: Diagram of the Rayleigh and Raman scattering processes. The lowest energy vibration state m is presented at the bottom with states of increasing energy above it. [41]

The ratio of Stokes and anti – Stokes Raman intensities is modified according to the Boltzmann's Law as follows,

$$\frac{I_{Stokes}}{I_{anti-Stokes}} = \frac{(\nu_{las} - \nu_{vib})^4}{(\nu_{las} + \nu_{vib})^4} e^{\frac{\Delta E}{kT}} \tag{2.7}$$

At normal temperatures, the population of the lowest (ground) vibrational state is larger than the population of the excited states, thus the ratio described above is very large resulting to the anti – Stokes Raman scattering, which requires the molecule to be already excited, to be very weak compared to the Stokes Raman scattering. At higher temperature values the anti – Stokes Raman scattering increases leading to a decrease in the relative ratio. [40]

- *Vibrations in crystals*

All the vibrations that occur in crystals can be considered as the superposition of plane waves propagating to infinity. These plane waves, which are called normal modes of vibration, are often designated as quasi-particles named *phonons*. Every phonon has energy $\hbar\omega$ and wave vector q. The phonon frequency $\omega(q)$ as a function of the wave vector q is known as the phonon dispersion relation.

Two types of phonons can be derived from the dispersion relation, called *acoustic* and *optical* phonon modes. For a crystal containing $n \geq 2$ different atoms, the total number of modes is 3n. Three of that branches correspond to the acoustic modes where the other $(3n - 3)$ branches are the optical modes in the crystal where q is confined to the first Brillouin zone. In acoustic modes the atoms of the unit cell are moving coherently in the same direction and the crystal can be considered to be displaced as a continuum. In optical modes the movement of the atoms in the unit cell is out-of phase where adjacent atoms are moving in opposite directions.

The atomic modes of vibration in a crystal can be either *longitudinal* (the atomic motion is parallel to the direction of wave propagation) or *transverse* (the atomic motion is perpendicular to the direction of wave propagation). Longitudinal and transverse modes correspond to both optical and acoustic phonon modes. The longitudinal and the transverse optical phonon modes are often labeled as LO and TO respectively. Likewise, the labels LA and TA correspond to the longitudinal and transverse acoustic phonon modes in crystals. [39], [42]

- *Raman scattering processes*

In semiconductors, during a scattering event an electron, absorbing a photon, is excited from the valence energy band to the conduction energy band. Then the excited electron is scattered by emitting or absorbing a phonon and then relaxes to the valence band by emitting a photon. Thus, phonon emission corresponds to Stokes scattering and phonon absorption corresponds to anti – Stokes scattering.

The intensities of Stokes and anti – Stokes processes depend on the population of the various vibrational states (number of phonon modes). The number of μth phonon modes with wave vector q at a temperature T is given by the Bose – Einstein statistics

$$n(q,\mu) = \frac{1}{e^{(\hbar\omega(q,\mu)/k_B T)} - 1} \tag{2.8}$$

where k_B is the Boltzmann constant. At room temperature the number of thermally excited phonons involved in the anti – Stokes scattering is very small. Thus the anti – Stokes scattering will be weak, compared to the Stokes scattering but it will increase relative to Stokes scattering as the temperature increases. [43]

- *First – order and second – order Raman scattering*

The number of phonons involved in a Raman scattering process can be one, two and so on which correspond to one – phonon, two – phonon, and multi – phonon Raman processes respectively. This number of phonons determines the order of a scattering process. The lowest order of such a process is the first – order Raman scattering in which one phonon is involved.

In second – order Raman scattering two phonons, or one phonon and one elastic scattering event are involved. In the latter case, the scattering event may consist of the same phonon mode, or different phonon modes. In second – order Raman scattering, phonons with q and – q wave vectors are included so the excited electron can relax to its initial position after scattering. [43]

Experimental set up of Raman Spectroscopy

The experimental set up of a typical Raman spectrometer consists of a focused laser beam which interacts with the specimen, a microscope, and a spectrometer for the analysis of the output signal.

The laser beam passes through a beam splitter and is focused through a microscope objective lens directly on the sample. The backscattered signal contains elastic (Rayleigh) scattered and inelastic (Raman) scattered light. Rayleigh scattered light is cut out with the use of a filter in order not to overwhelm the weak Raman signal. Diffraction of the beam then occurs by a high resolution grating (2400 lines/mm) that analyses the signal. The output signal is detected though a CCD sensor which converts the incident photons to electrical signal which is then analyzed by the proper PC software giving rise to the Raman spectrum.

In this work, the Thermo Scientific, Nicolet Almega XR Micro Raman system was used, including microscope with magnification up to ×100. A diode – pumped solid – state laser of 473nm in wavelength was focused by the microscope objective lens, with maximum output power of 50μW. A schematic representation of the Raman spectrometer set up is shown in Figure 2.4.

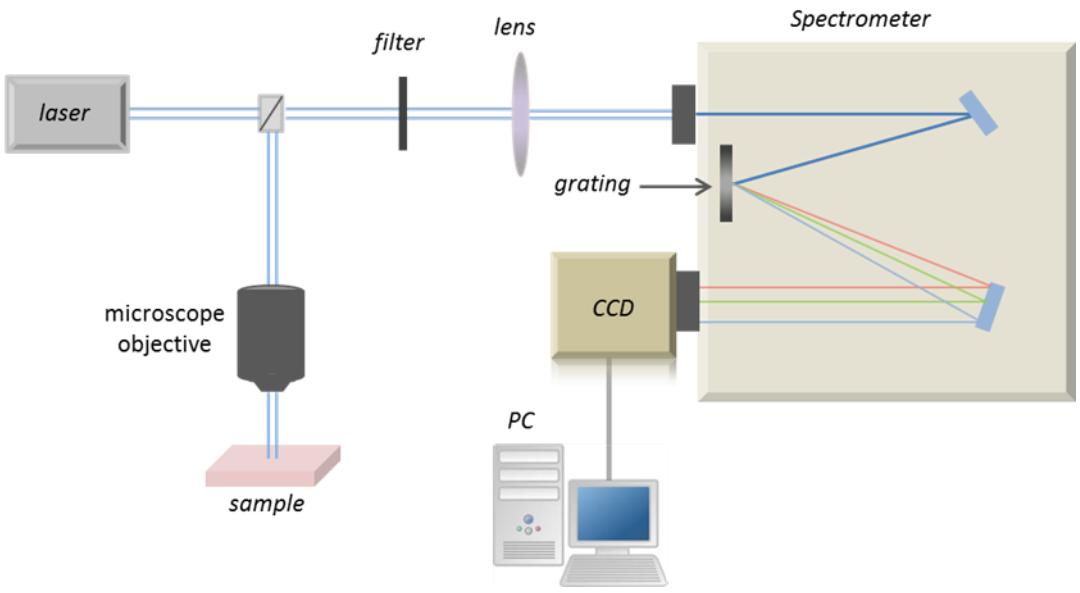

Figure 2.4: Schematic representation of the experimental set up used for Raman Spectroscopy.

2.2 Deposition methods for MoS_2

Various methods are available for the deposition of materials contained in dispersion (liquid phase deposition) such as drop casting, dip - coating, spray – coating, and filtration. In this thesis, drop – casting, dip – coating and filtration were tested as potential MoS_2 deposition methods for device fabrication due to the simple and low cost operation, and the fact that no or negligible amount of the material is wasted. The aforementioned methods will be described in the next section.

2.2.1 Drop – casting method

During the drop – casting process, droplets of the dispersion containing the material of interest, (MoS_2 nanoflakes in our work) are deposited on the substrate through a pipette. The sample is then drained (usually heated on a hot plate) for solvent evaporation. The droplets will be spread in different ways if the substrate is hydrophilic or hydrophobic. Concerning the case of a hydrophilic substrate, the spread of the droplet will be wider covering a larger area while in the hydrophobic case the material will stay within the initial position of the droplet without spreading, during the evaporation of the solvent. The main steps of the drop casting method, including the hydrophilic and hydrophobic cases, are presented in the following figure (Figure 2.5).

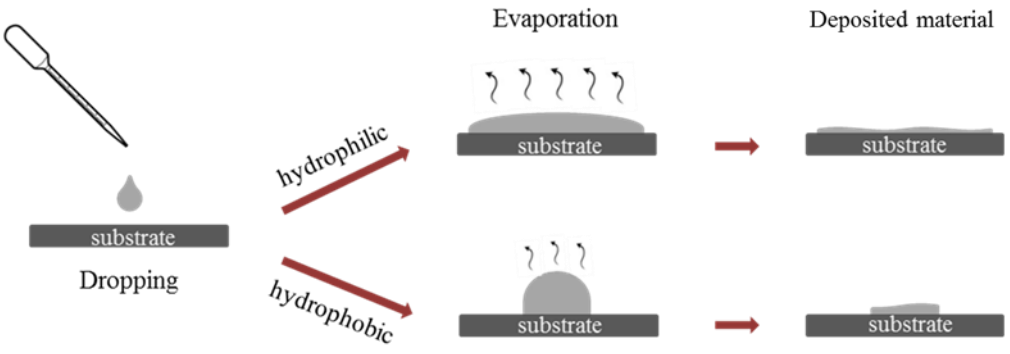

Figure 2.5: The main steps of drop casting method both for hydrophilic and hydrophobic substrates.

2.2.2 Dip – coating method

The dip – coating method involves the immersion of the substrate into a liquid and its subsequent withdrawal at a constant speed under well – defined temperature and atmospheric conditions (the process occurs in an oven connected to the dip – coater, see Figure 2.7). The coating thickness depends on the withdrawal speed, the viscosity of the liquid, and the solid content.

During the process, the substrate to be coated is, at first, placed in the holder of the dip – coater machine and is then immersed into the dispersion bath. It is then started to be pulled up at a constant speed. During the withdrawal time, thin layers of the material are deposited while the excess of the liquid is drained from the surface of the substrate. At the same time the solvent evaporates from the liquid, forming the thin layer. The main steps of the dip – coating process, described above, are presented in Figure 2.6.

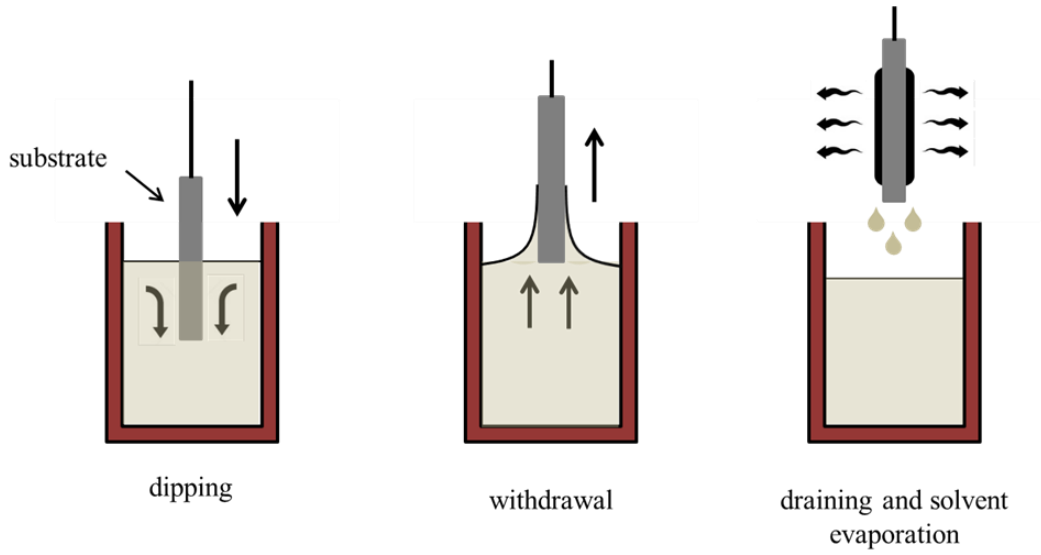

Figure 2.6: The main steps for dip – coating technique.

In this work a PTL – NMB dip – coater was used with a touch – screen control. The upper limit of pulling and dipping speed is 500nm/sec and the temperature range of the oven is 20 - 200˚C. The dip – coater machine is presented in the following picture (Figure 2.7).

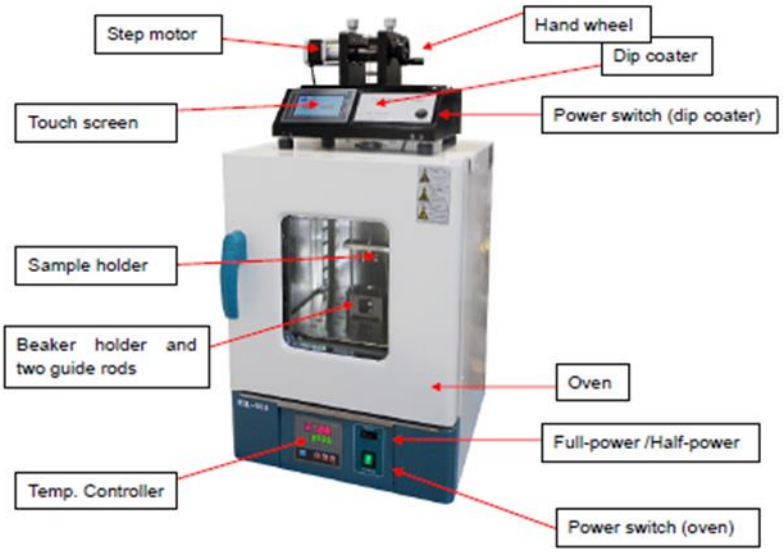

Figure 2.7: Structure of the dip – coater machine. The labels contain the parts of operation.

2.2.3 Filtration method

Filtration is another technique for depositing the material of interest from dispersion. According to this method, solids can be separated from liquids by the use of an interposing porous medium (filter) through which only particles of the liquid can pass while the solid particles are trapped on the surface of the filter. The liquid that passes through the filter is called the filtrate (Figure 2.8 a). The filters for this process are shown in Figure 2.8 (b) made from cellulose ester with pores of 50nm in diameter.

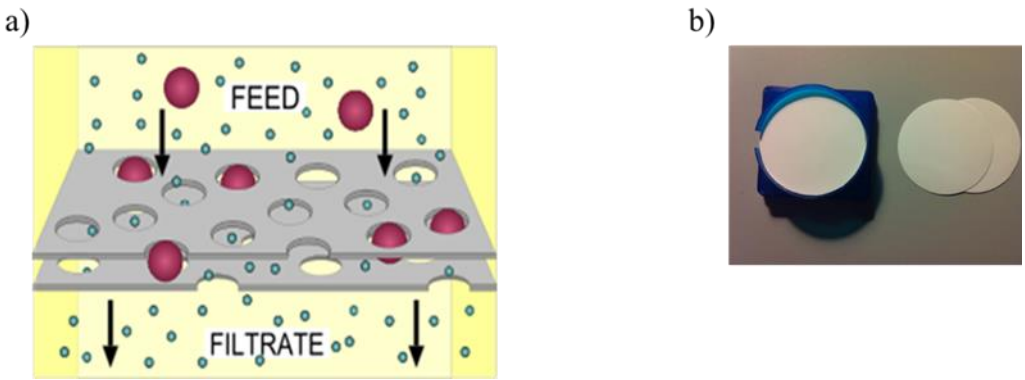

Figure 2.8: (a) Simple schematic representation of the filtration method. (b) Filter papers made of cellulose ester with pores of 50nm in diameter.

The experimental set up used for this method containing the main tools of the process are presented in the next figure (Figure 2.9) and discussed below. The process for MoS_2 deposition by the filtration method is described in the following chapter.

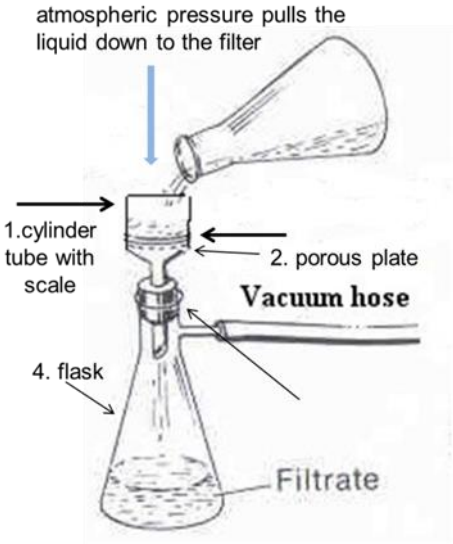

Set up:

1. Cylinder tube with scale (syringe in our case) at the top.
2. Plastic base containing a metallic porous plate.
3. Filter paper on the top of the porous plate (made of cellulose ester).
4. Flask made of glass with an arm connected to vacuum.
5. Rubber bunk for sustaining the base with the filter on the top of the flask.

Figure 2.9: The main objects used for the set – up of the filtration technique.

Filtration process includes the following tools. A cylinder tube with scale which is placed on the top of a plastic base. This base contains a metallic porous plate at the bottom. On this porous plate we put the filter. A rubber bunk is used to sustain the base on the top of a flask connected to vacuum, where the filtrate is collected. When the dispersion is poured into the cylinder, it is pulled down through atmospheric pressure. The solid parts of the dispersion remain on the filter while the flask finally contains only the filtrate.

2.3 – Lithographic techniques for metal deposition

Lithography is a fundamental technique for fabricating devices in micrometer and nanometer scale, required for nanotechnology research. It involves the creation of a desired pattern on a specific layer of material called the resist and the subsequent transfer of that pattern onto the substrate through etching or lift – off process. Many lithographic techniques have been employed in the recent years with various exposure sources, such as photolithography, extreme ultraviolet (UV) lithography, electron beam lithography, ion beam lithography and X – ray lithography. In this thesis electron beam lithography and optical lithography were the lithographic techniques used for metal deposition.

2.3.1 Electron Beam Lithography (EBL)

Electron beam lithography (EBL) constitutes a predominant technique used for nanofabrication due to the ability of forming patterns down to sub – 10nm nanometer scale. It involves a focused electron beam to form the patterns needed for material deposition on a substrate. It provides the fabrication of semiconductor devices with high resolution. [44] This lithographic technique was used for device fabrication in this thesis and is described, in details, in the following section. Figure 2.11 represents the basic steps involved in EBL method.

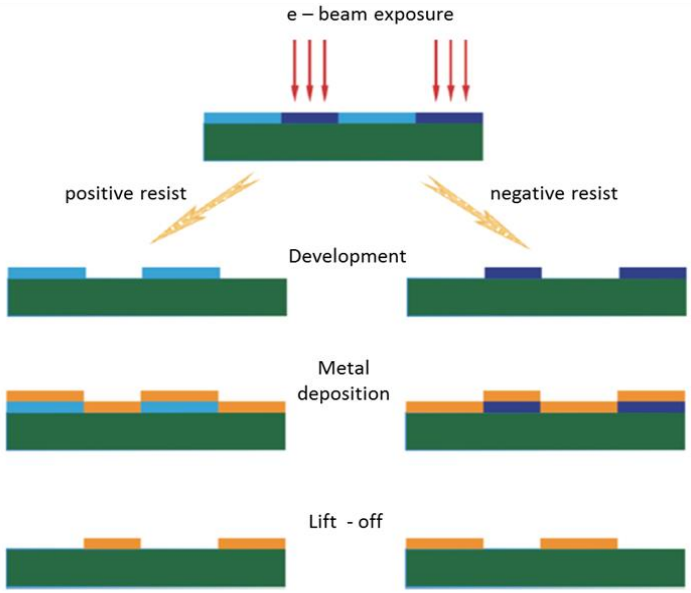

Figure 2.11: Schematic image for the basic steps of e – beam lithographic technique for device fabrication. [44]

In EBL method, the resist that is used, is a material (usually a polymer) which changes its solubility after exposure to electrons. Either negative or positive resists are used depending on whether the unexposed or the exposed areas are removed from the substrate during the process. Regarding positive resist, the regions of the resist exposed to electrons become more soluble in developers while the unexposed areas remain unchanged. The opposite procedure occurs for negative resists. Here the unexposed regions will be removed in developers. Developer is a solvent used after the e – beam exposure which acts on the exposed or unexposed areas according to positive or negative resists, respectively. [44], [45]

2.3.2 Optical lithography

Optical lithography (or photolithography) is another technique used for micro – scale device fabrication. In this technique a photo – resist material (light – sensitive polymer) sensitive to ultraviolet (UV) light is employed for the desired patterning. Initially, the photo – resist material is coated on a transparent substrate. A photomask with opaque features is places afterwards and is then exposed to UV light with wavelengths in the range of 193- 436nm. Using a negative photo – resist the unexposed areas become more soluble in a developer (see e – beam lithography technique) and it can be removed resulting in the desired pattern. [46]

2.4 Experimental set up for photoresponse

After the fabrication of photodetectors based on MoS_2 (drop – casting deposition and metallization) the photoresponse (response under illumination) of the devices was investigated.

For that purpose, a CW laser beam with a wavelength $\lambda = 405nm$ was used for illumination. The laser beam was driven through a mirror to a quartz lens which allowed us to localize the beam on the surface of the sample. The lens was placed on a xyz micrometer translation stage in order to focus the beam on each device with high spatial precision. The laser beam was modulated by an optical chopper – MC2000 Optical Chopper System with MC1F10 10 – slot Chopper Blade – with a frequency range of 20Hz – 1kHz. Two probes were connected to the metal electrodes and the photocurrent signal was detected with the use of a lock – in amplifier – DSP 7260 (EG&G instruments). A CCD Camera – Shixin B/W camera – connected with a screen was focused on the surface of the sample and allowed us to have an optical view of the devices. A voltage source was also used for applying a constant external bias.

All the measurements for photocurrent detection were performed in air at room temperature. A schematic representation of the set up used for photocurrent measurements is presented in Figure 2.14.

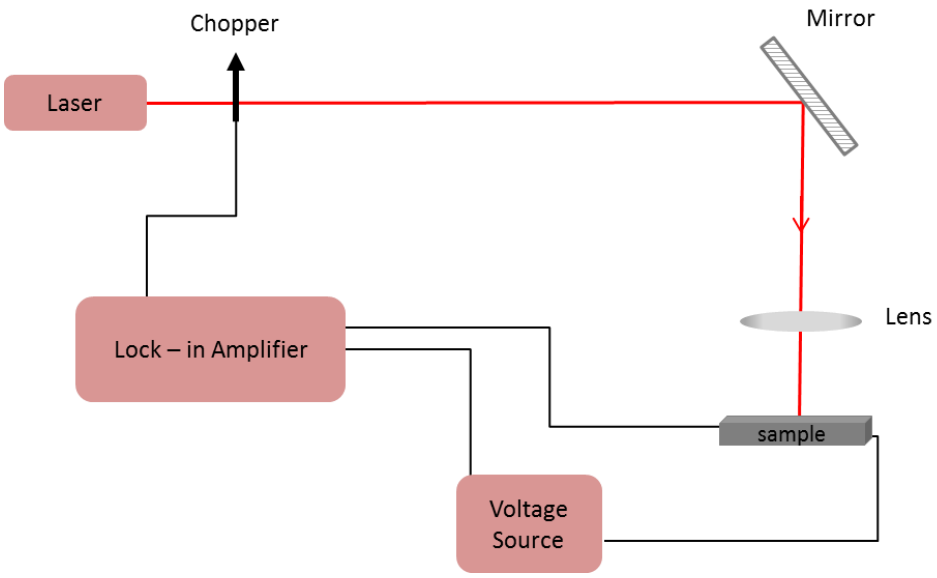

Figure 2.14: Schematic representation of the experimental set up for photocurrent measurements with the use of a lock – in amplifier.

Chapter 3 – MoS_2 deposition - Results

For the liquid deposition methods adopted in this work (drop – casting, dip – coating, and filtration) we used a dispersion containing MoS_2 nanoflakes, the material of interest in this thesis.

The dispersion consists of:

1. MoS_2 – 0.001
2. Ethyl Alcohol – 45%
3. Water – 55%.

3.1 Drop - casting deposition

According to the drop casting method (see section 2.2.1), the first attempt of MoS_2 deposition involves the drop of small droplets from the dispersion through a pipette on untreated Si/SiO_2. The sample was then placed on a hot plate and the temperature was set at 70˚C in order to evaporate the solvent. A representative image of a droplet deposited on the substrate in presented in Figure 3.1.1.

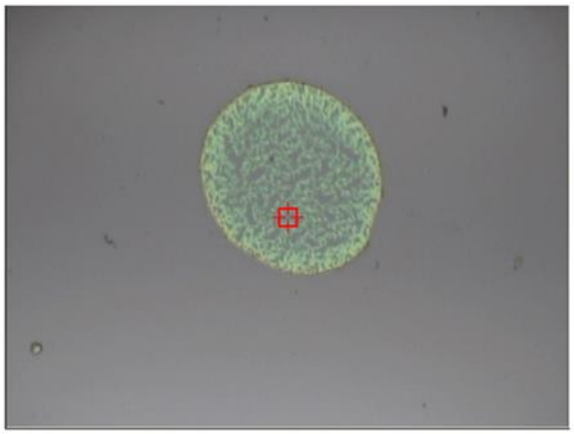

Figure 3.1.1: Optical image for a deposited droplet on Si/SiO_2 substrate taken from the Raman microscope.

For the sample described above Raman analysis was made at the border of a droplet and in a place inside the droplet. Figure 3.1.2 corresponds to the laser spot placed at the border (a) and inside the droplet (b) of the sample which contains small droplets.

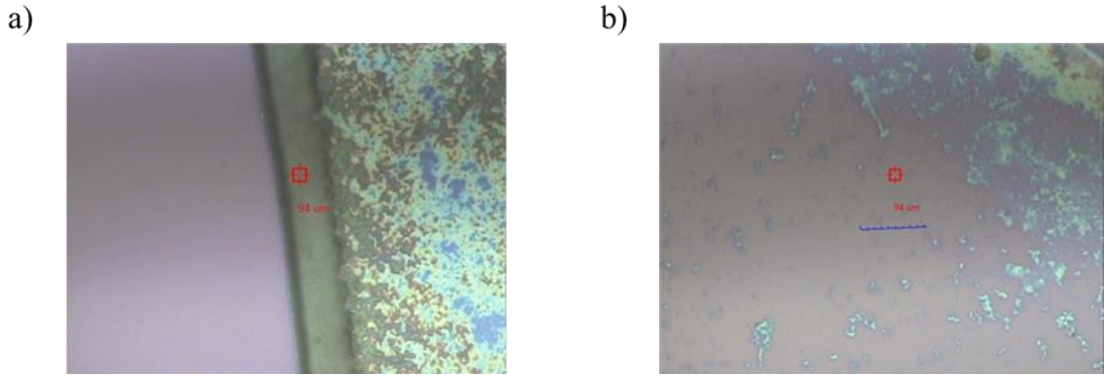

*Figure 3.1.2: Images from the Raman microscope. Laser spot placed **(a)** at the border and **(b)** inside the droplet.*

The Raman spectra regarding to these places of the laser spot are depicted in the following figure (Figure 3.1.3). In Figure 3.1.3 (a) the peak at ~ 519cm^{-1} corresponds to silicon substrate. In Figure 3.1.3, the peak at ~ 379cm^{-1}(a) and at ~ 382cm^{-1} (b) correspond to the $E_{2g}{}^{1}$ vibrational mode and the peaks at ~ 402cm^{-1}(a) and ~ 406cm^{-1}(b) to the A_{1g} mode of MoS_2. From the frequency difference $\Delta\omega\left(A_{1g} - E_{2g}{}^{1}\right) \approx 23cm^{-1}$ we can estimate a trilayer form of MoS_2 flakes compared to previously reported values. [47], [48]

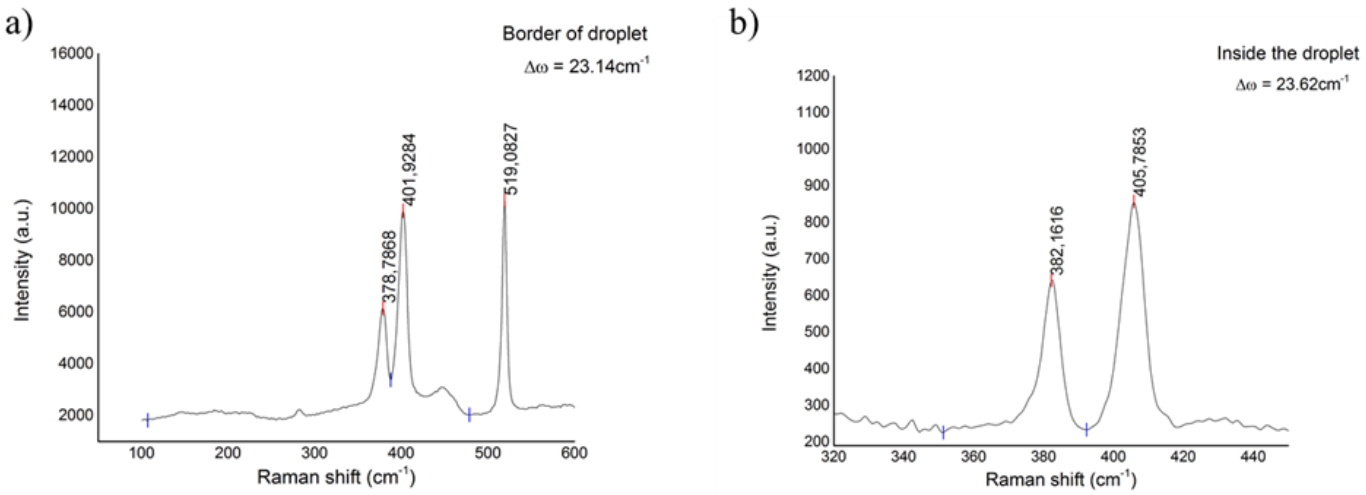

*Figure 3.1.3: Raman spectra for the border **(a)** and inside the droplet **(b)** corresponding to the red spot in Figures 3.1.2 (a), and (b), respectively, providing the existence of MoS_2.*

3.1.1 Cleaning methods

In order to improve the flake separation and increase the dispersion of nanoflakes contained in dispersion, compounds known as surfactants are used in the dispersion which act as dispersants that prevent the agglomeration of nanoflakes. The existence of surfactant was observed during the deposition process of MoS_2 by the dispersion used in this work. In order to remove the surfactant as series of cleaning methods were employed.

I. Water cleaning method

The first attempt for the removal of surfactant was by using water. After MoS_2 deposition the sample was immersed into water and left for 1 hour. Water resulted in the dispersion of the surfactant (the material observed in Figure c) outside the droplet but not in material removal. Figures 3.1.4 (a) and (b) indicate the place of the surface of the sample which was tested after water cleaning. According to the Raman spectrum (Figure 3.1.4 d) the remaining material is not MoS_2.

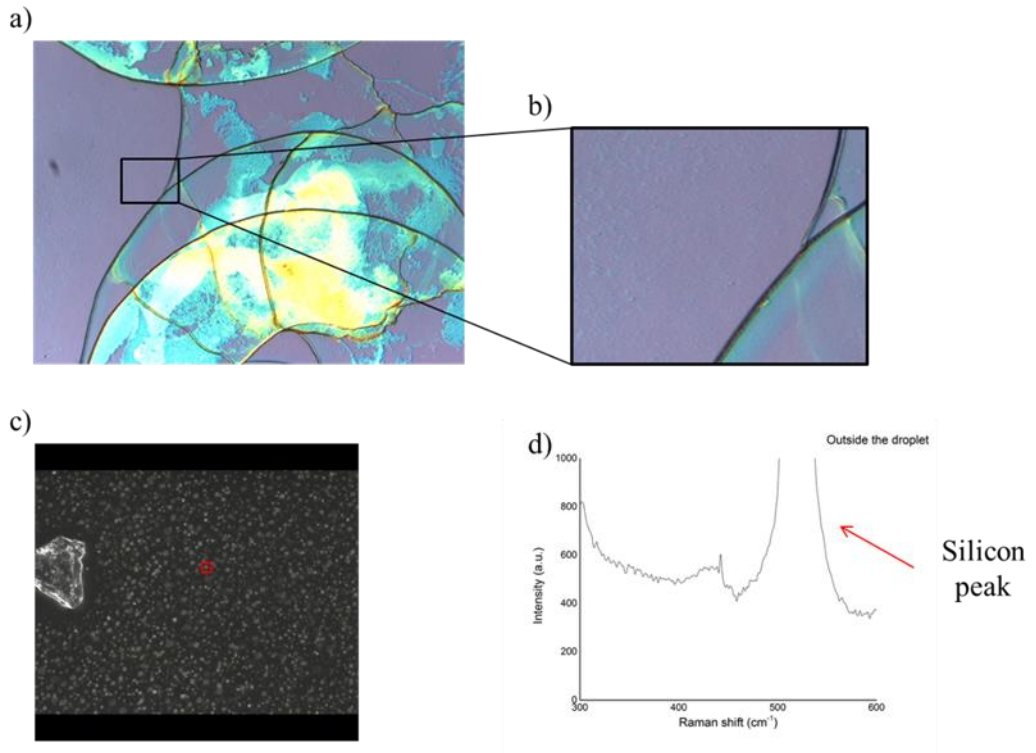

Figure 3.1.4: ***(a)*** *and* ***(b)*** *Images from optical microscope for the sample cleaned with water for 1 hour.* ***(c)*** *Image from Raman microscope and* ***(d)*** *Raman spectrum corresponding to the red spot in (c).*

II. Acetone cleaning method

A second attempt was made by using acetone in order to clean the surface of the sample. Two different samples were tested through Raman spectroscopy. The first was cleaned with acetone for one hour and the second was cleaned with acetone for 2 days. The absence of the surfactant was observed with negligible difference in the distribution of the material. As a result, acetone does not affect the deposition of the material itself. The image from the optical microscope and the corresponding Raman spectrum for the sample cleaned with acetone for one hour are depicted in Figure 3.1.5 (a) and (b), respectively.

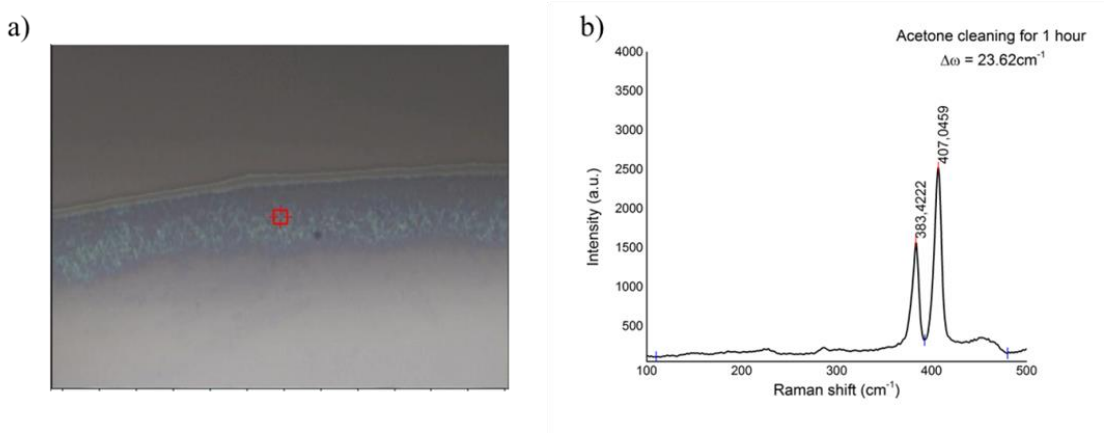

*Figure 3.1.5: Image from optical microscope **(a)** and Raman spectrum **(b)** for the sample cleaned with acetone for 1 hour.*

In the following figure (Figure 3.1.6) the image from optical microscope and Raman spectrum for the sample left in acetone for 2 days, are presented.

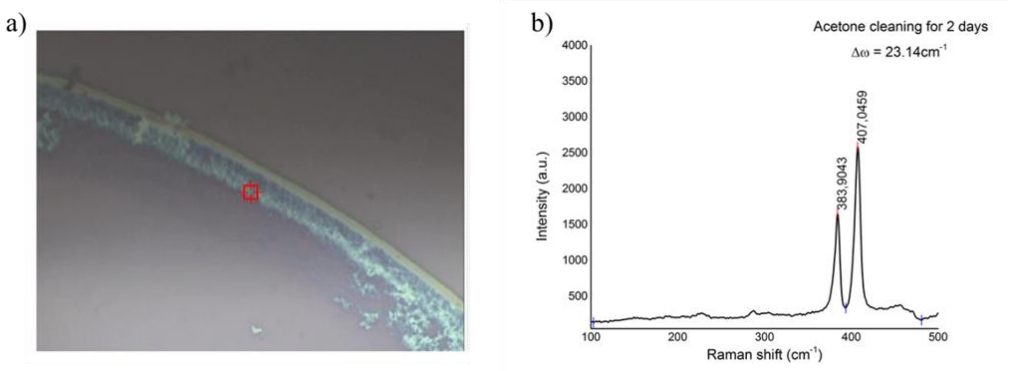

*Figure 3.1.6: Optical microscope image **(a)** and Raman spectrum **(b)** for the sample cleaned with acetone for 2 days.*

3.1.2 Methods for homogeneous deposition

The untreated Si/SiO_2 substrate and the heating temperature of 70˚C for solvent evaporation result in inhomogeneous MoS_2 deposition (through the images from the optical microscope and through the corresponding Raman spectra). By Raman analysis (inserted in the next figures), a significant amount of MoS_2 occurs at the border of the droplet, less is deposited inside the droplet, and negligible amount at areas where the existence of the material was not visible through the optical microscope. In the latter case, a Raman signature of MoS_2 was still observed.

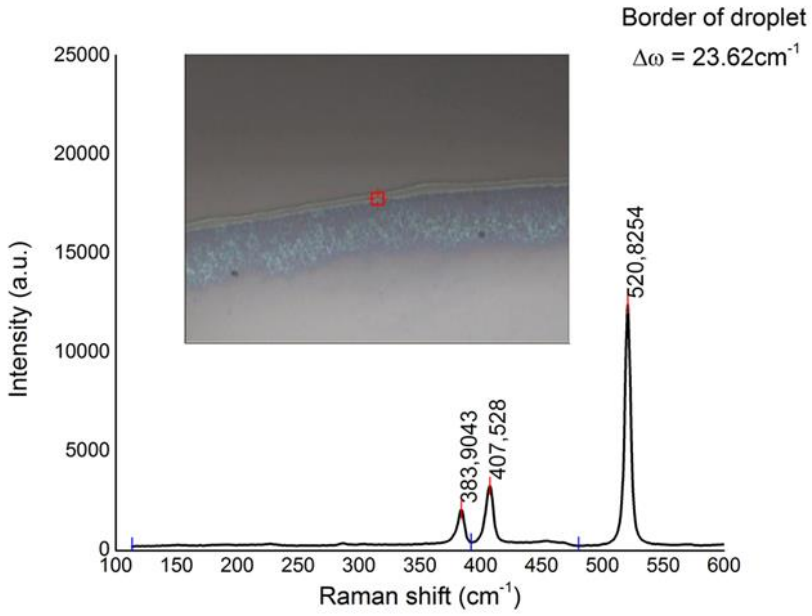

Figure 3.1.7: Raman spectrum for the laser spot position at the border of the droplet. Inset: Image from the optical microscope at the border of the droplet.

Figure 3.1.7 depicts the Raman spectrum and the position of the laser spot at the border of the droplet. The image from the optical microscope for this spot position is also shown.

In Figure 3.1.8 the results from a place inside the droplet are presented. Less amount of material was observed in this case compared to the intensity of the Raman signal with respect to the silicon peak (ω_{Si} = 519,574cm^{-1}).

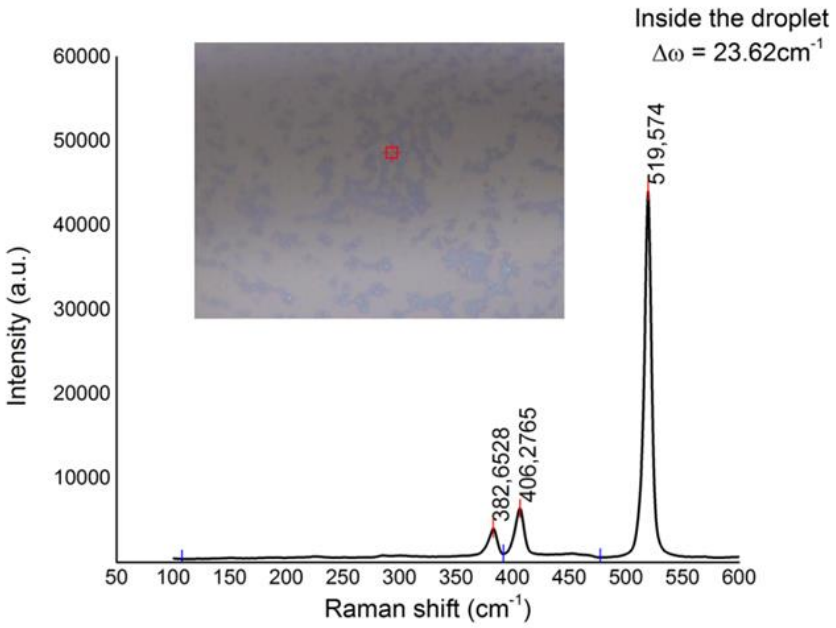

Figure 3.1.8: Raman spectrum for the laser spot position inside the droplet. Inset: Image from the optical microscope at the corresponding laser spot position.

The following figure (Figure 3.1.9 a) represents the result from Raman analysis at a place where the existence of MoS_2 was not observed through the optical microscope. Nevertheless, a negligible amount of material appeared to exist, due to the small intensity Raman signal which was measured. The inset in Figure 3.1.9 depicts the area of the MoS_2 peaks from the Raman spectrum.

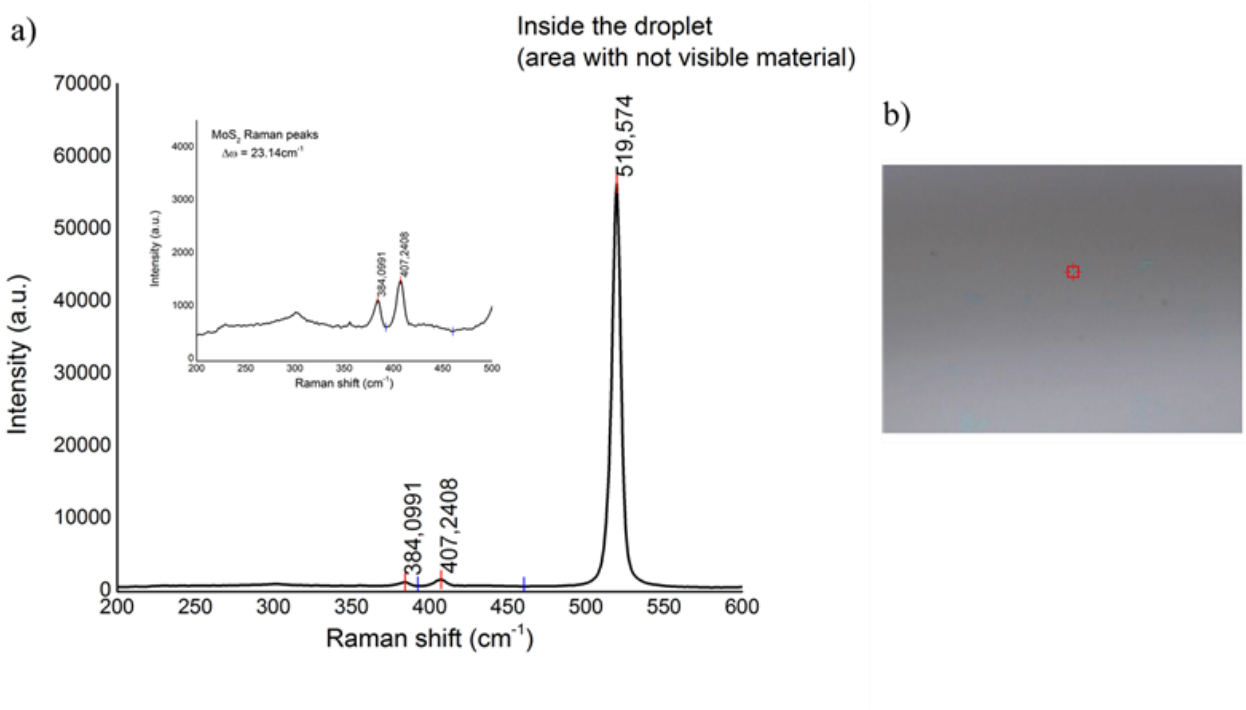

Figure 3.1.9: ***(a)*** *Raman spectrum for the position of the laser spot depicted in the image from optical microscope* ***(b)****. Inset: Further analysis of the Raman spectrum at the range of 200 to 500cm^{-1} including the low intensity MoS_2 peaks.*

I. HMDS treatment

In order to achieve more homogeneous MoS_2 deposition on the surface of the sample, the Si/SiO_2 substrate underwent HMDS treatment. Under this treatment the substrate interacts with HMDS (hexamethyldisilazane), and transforms to hydrophobic. This modification leads to less dispersion of the deposition as the droplet remains at its initial position during solvent evaporation. This procedure involves the use of a spin coater. A big HMDS droplet is deposited on the substrate through a pipette. Then the sample was placed on the base of the spin coater and during the spin coating the liquid spreads and covers all the surface of the substrate. The spinning time was 30s and the sample was heated at T = 110˚C for 1 minute, afterwards. Deposition of MoS_2 then took place on the HMDS treated sample.

The temperature condition under which solvent evaporation occurs is also a critical factor. From the results cited so far, the temperature of T = 70˚C was not efficient for homogeneous deposition of the material. Concerning this factor, solvent evaporation occurred under room temperature, T = 20˚C, with the combination of HMDS treated substrate resulted in an improvement in homogeneity for the deposited material. The results are presented in the following figure (Figure 3.1.10) for a test sample.

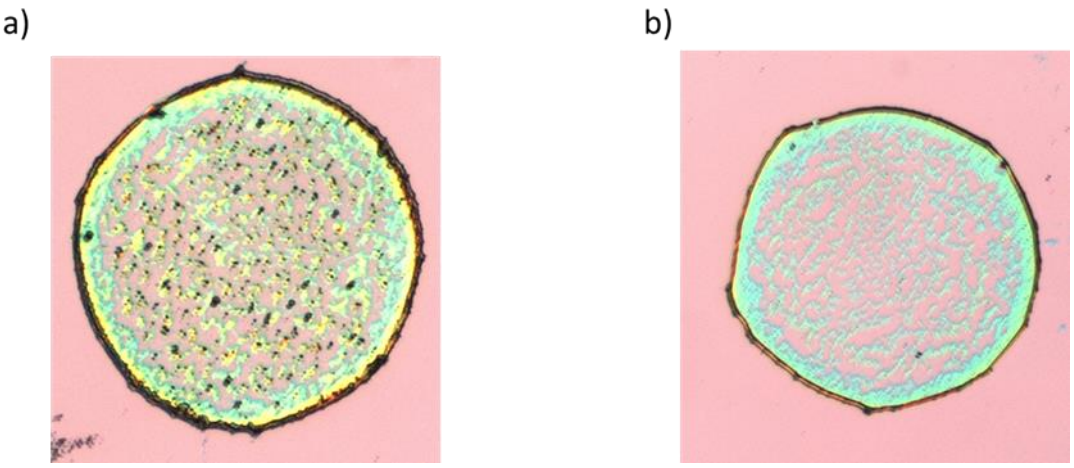

Figure 3.1.10: ***(a)*** *Image from optical microscope for droplet on HMDS treated Si/SiO_2 substrate with solvent evaporation under room temperature.* ***(b)*** *Droplet of the same sample (Figure 3.10 a) cleaned with acetone.*

The aforementioned process, that is HMDS treated substrates and room temperature for solvent evaporation, was adopted for the drop – casting deposition method as the initial step for the fabrication of photodetectors. Small droplets of the material were deposited on HMDS pre – treated Si/SiO_2 substrate and left to dry at room temperature (name of sample: MoS2_det_02).

During the process a homogeneous deposition around the droplet was also observed. This “blue surrounding”, as it shown in Figure 3.1.11, was investigated through Raman analysis and appeared to be surfactant which was easily removed with the use of acetone. In this Figure, two representative droplets deposited on the as – prepared substrate, are shown.

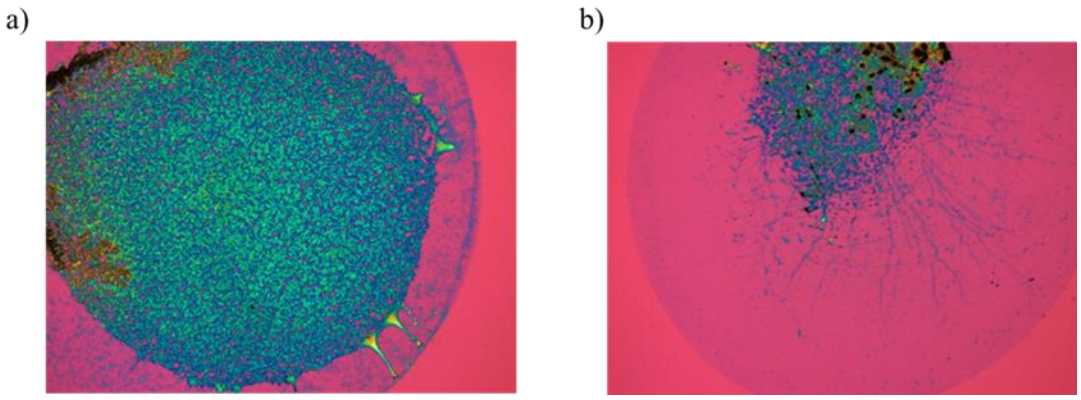

Figure 3.1.11: ***(a)*** *and* ***(b)*** *Droplets of MoS_2 on HMDS treated substrate under room temperature for solvent evaporation.*

In the following figure (Figure 3.1.12) the Raman spectrum corresponding to the "blue surrounding" is inserted, providing indication that this area consists of surfactant but not MoS_2, as the Si peak was the only peak observed in the spectrum.

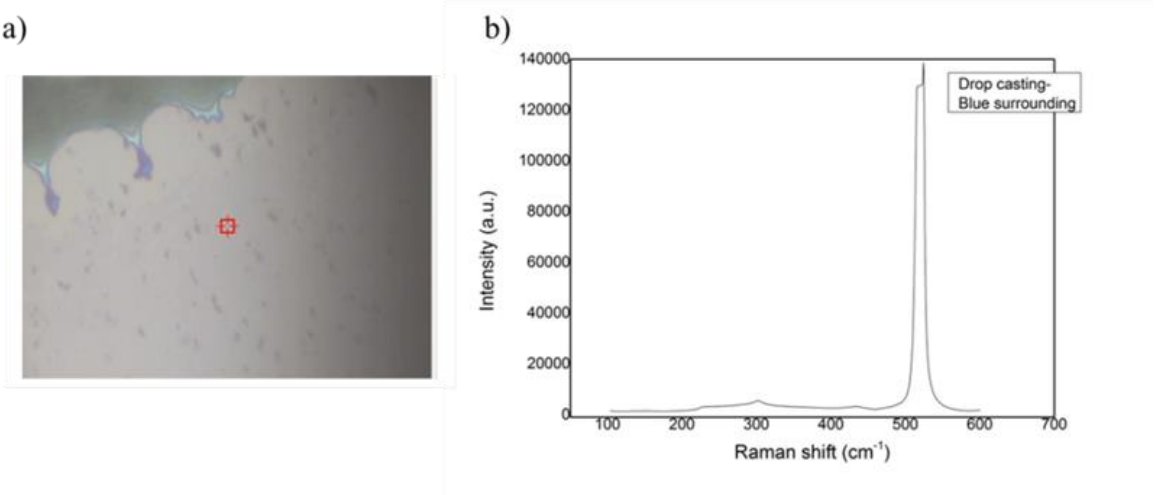

Figure 3.1.12: ***(a)*** *Image from optical microscope for the area of "blue surrounding".* ***(b)*** *Raman spectrum for the position of the laser spot.*

Acetone cleaning method was used in this sample in order to remove the surfactant. The results from this method are depicted in Figure 3.1.13 where another deposited droplet of the same sample is presented. The surrounding containing the remaining surfactant was also observed (Figure 3.1.13 a) and was successfully removed after diving the sample into acetone (Figure 3.1.13 b).

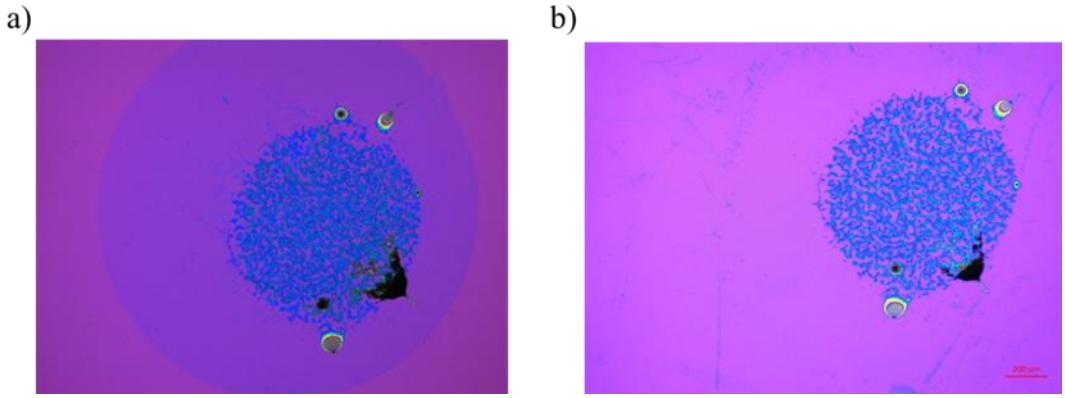

Figure 3.1.13: Droplet of MoS_2 on HMDS treated substrate under room temperature for solvent evaporation. ***(a)*** *pristine sample and* ***(b)*** *sample cleaned with acetone for 5 minutes.*

II. Oxygen Plasma (O_2) treatment

Another effort that was made in order to achieve a homogeneous deposition in a large – scale (larger than the deposition of small droplets) was by oxygen (O_2) plasma treatment. Oxygen plasma cleaning was performed on Si/SiO_2 substrate before MoS_2 deposition. Under this process the physical properties of the substrate alter and it becomes hydrophilic. This fact leads to a wide spreading of the droplet as it contacts with the substrate.

In order to attain a deposition containing a significant amount of MoS_2, 3 big droplets of the solution were deposited on oxygen plasma treated Si/SiO_2 substrate. The droplets covered all the surface of the sample which was left to dry at room temperature. The result of this process with the full coverage of the surface is presented in the next figure (Figure 3.1.14).

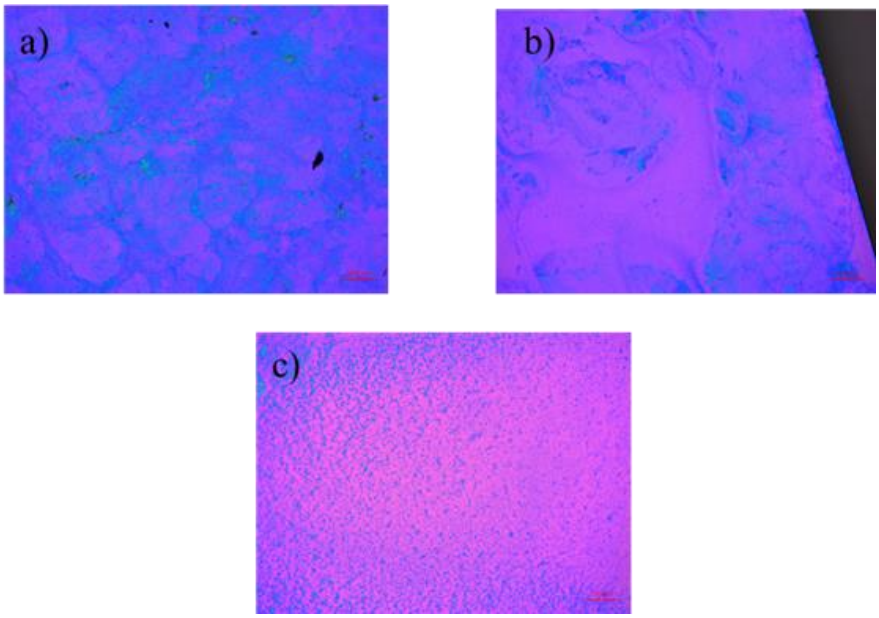

Figure 3.1.14: Image from the optical microscope for the plasma treated sample. ***(a)***, ***(b)***, *and* ***(c)*** *correspond to different places from the plasma treated sample. Solvent evaporation occurred at room temperature.*

Measurements by SEM were also taken for the sample described above, for further investigation. In Figure 3.1.15, the results from these measurements are presented. The homogeneous deposition of the material was observed at 1μm scale (Figure 3.1.15 b). Regarding the results from plasma treatment, the as – prepared sample was used for e – beam lithography (see section 2.3.1) as the next step of device fabrication (name of sample: MoS2_det_01).

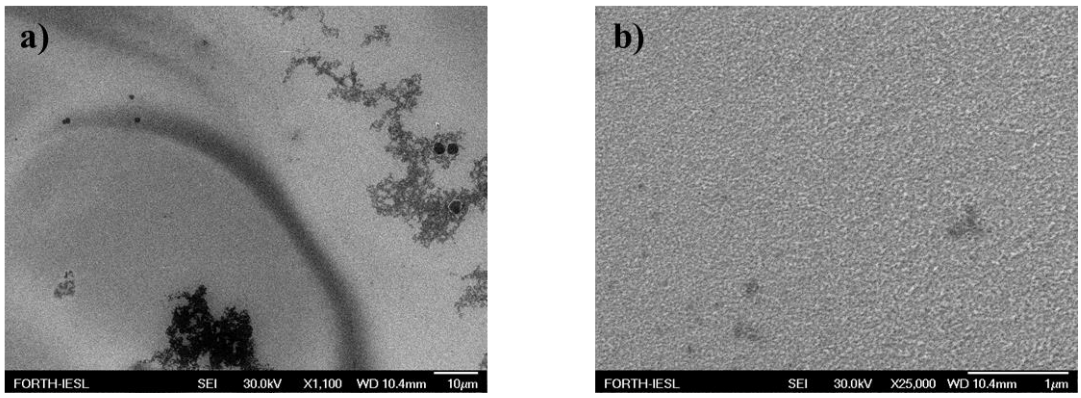

Figure 3.1.15: SEM images for the sample MoS_2*_det_01.* ***(a)*** *SEM image at 10μm scale and* ***(b)*** *SEM image at 1μm scale.*

According to Raman analysis made for the majority of the samples described above, the mean value of the frequency difference was found to be $\Delta\omega \approx 23cm^{-1}$ with no significant variations. Thus, this parameter was used as estimation of the multi – layer nature of MoS_2 flakes, but not with absolute accuracy due to the random stacking and inevitable aggregation among the flakes. The two characteristic Raman modes E_{2g}^1 and A_{1g} reveal the existence of the 2H – MoS_2 crystal. The line widths of the two modes (mean values of ~ $8cm^{-1}$ for E_{2g}^1 , and ~ $9cm^{-1}$ for A_{1g} for the majority of the samples that were tested) are broadened with respect to reported values of exfoliated samples [48] which can be attributed to lateral inhomogeneity of the flakes or to the presence of defects. [7]

3.2 Dip – coating deposition

Dip – coating technique (see section 2.2.2) was another method adopted for MoS_2 deposition. A series of 5 samples was fabricated under different values of temperature (T) and withdrawal speed (u). Table 2 contains all the different samples prepared by this technique. Oxygen plasma treatment was used on Si/SiO_2 substrate for all the aforementioned samples before MoS_2 deposition.

Table 2: Samples with MoS_2 deposition by dip – coating method.

Sample	**Withdrawal Speed (nm/s)**	**Temperature (˚C)**
MoS_2 (GHR0407)	500	20
MoS_2(GHR0405)	250	20
MoS_2(GHR0410)	125	20
MoS_2(GHR0411)	500	40
MoS_2(GHR0403)	500	60

The results for every sample will be discussed in the following section, separately.

- **MoS_2 (GHR0407) → u = 500nm/s and T = 20˚C**

In this sample big clusters were observed to be dispersed on the substrate (Figure 3.1.16). At some place near the clusters there was a small amount of the material according to the Raman spectrum.

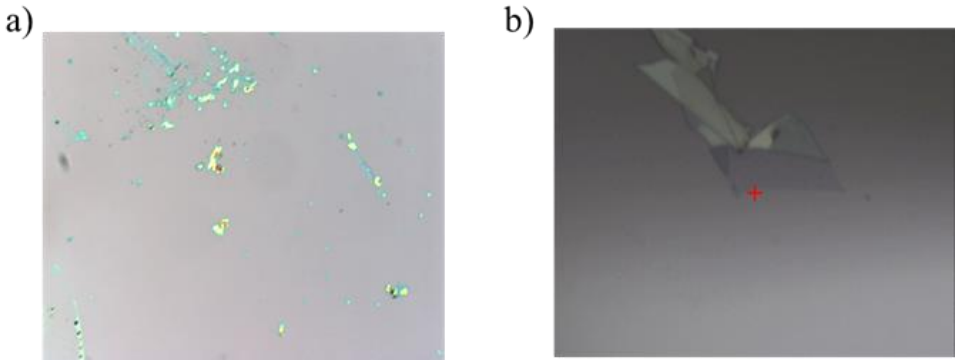

Figure 3.1.16: Optical microscope images for GHR0407 **(***u = 500nm/s and T = 20˚C). **(a)** Image from optical microscope under ×20 magnification and **(b)** big cluster under ×100 magnification.*

Further investigation, through Raman analysis, was made at the area near the big cluster where a thin piece of material appeared to exist, as shown in Figure 3.1.16 b and is inserted in the following figure (Figure 3.1.17). The same estimated trilayer form of MoS_2 ($\Delta\omega = 23.62cm^{-1}$) was observed by the Raman spectrum, as it has been measured so far.

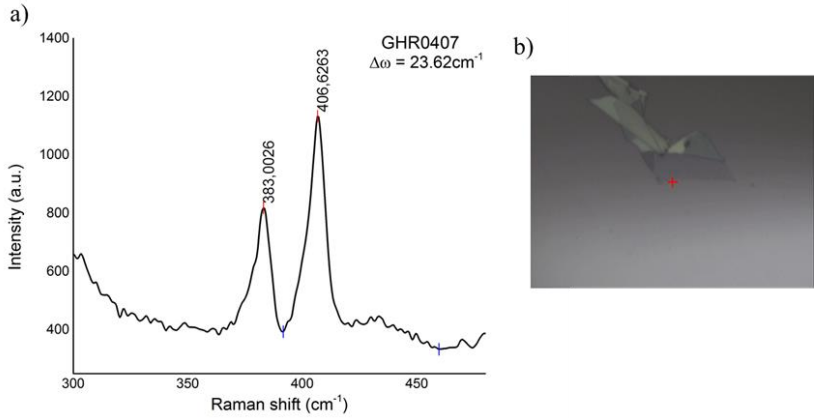

*Figure 3.1.17: **(a)** Raman spectrum for the position of the red cross in **(b)** for the sample GHR0407 (u = 500nm/s and T = 20˚C).*

Almost the same results of deposition were observed for the sample **GHR0405** with withdrawal speed u = 250nm/s, and temperature of T = 20˚C for solvent evaporation.

- **MoS_2 (GHR0410) → u = 125nm/s and T = 20˚C**

  Figure 3.1.18 represents the results of MoS_2 deposition under the above parameters. A significant amount of material was deposited at the position of the holder of the dip – coater (light blue lines in Figure 3.1.17 a).

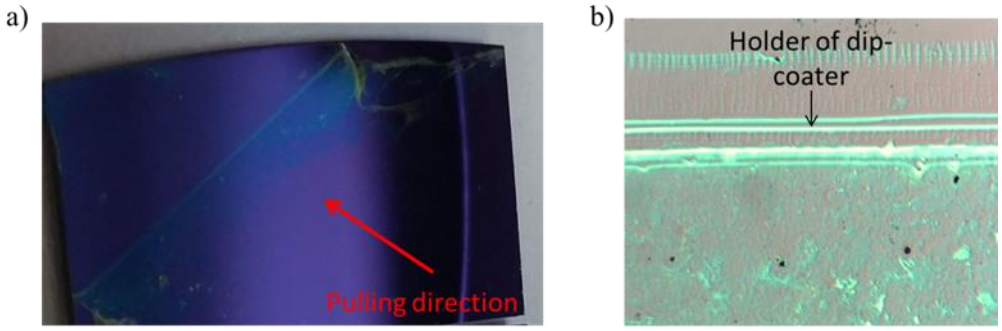

Figure 3.1.18: ***(a)*** *Image from the sample GHR0410 (u = 125nm/s and T = 20˚C**)**. The light blue line corresponds to the position of the holder of dip – coater and the direction of withdrawal is also depicted with the red arrow.* ***(b)*** *Image from the optical microscope at the area near the holder of dip – coater (light blue line from (a)).*

In the following figure (Figure 3.1.19) the area away from the position of the holder is presented.

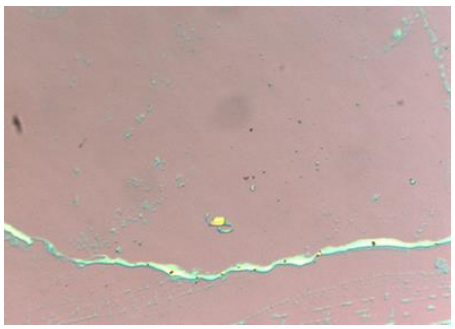

Figure 3.1.19: Image from the optical microscope at the area away from the holder at the surface of the sample GHR0410 (u = 125nm/s and T = 20˚C).

In this kind of deposition big traces of the material were deposited, as shown in the image above (Figure 3.1.19).

- **MoS_2 (GHR0411) → u = 500nm/s and T = 40˚C**

According to the deposition for the sample GHR0411, agglomerations of the material were observed in the form of lines, as shown in the next figure (Figure 3.1.20 b). The light blue colored areas correspond to the deposition of material (MoS_2).

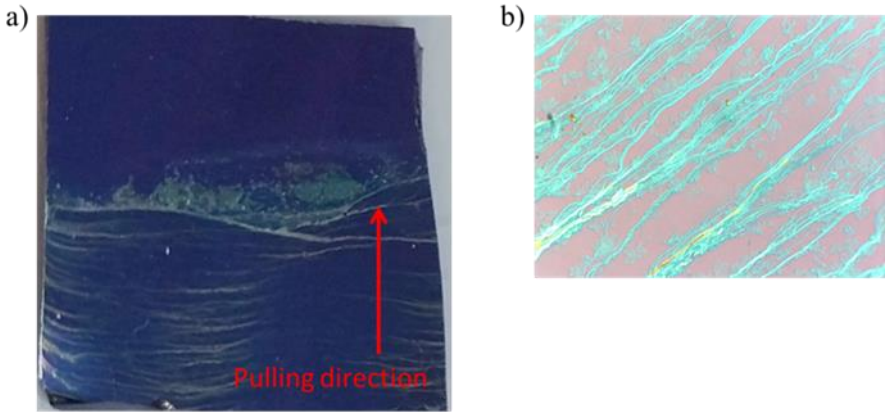

Figure 3.1.20: ***(a)*** *Image from the sample GHR0411 (u = 500nm/s and T = 40˚C).The red arrow indicates the direction of withdrawal.* ***(b)*** *Image from the optical microscope at the area of the line form agglomeration.*

Further investigation was made in the area between those "line form" agglomerations in order to find out whether material is contained. Raman spectrum provided the signature of MoS_2 existence in the corresponding area, as shown in the following figure (Figure 3.1.21).

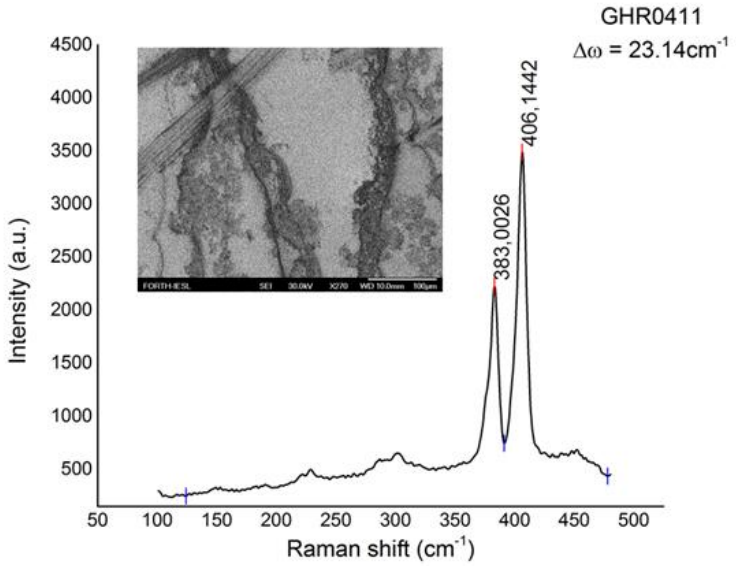

Figure 3.1.21: Raman spectrum for the area between the "line form" MoS_2 deposition for the sample GHR0411 (u = 500nm/s and T = 40˚C). Inset: SEM image for the corresponding area.

- **(MoS_2) GHR0403 → u = 500nm/s, T = 60˚C**

More pronounced "line form" agglomerations revealed under the temperature of T = 60˚C near the bottom of the sample and are presented in Figure 3.1.22.

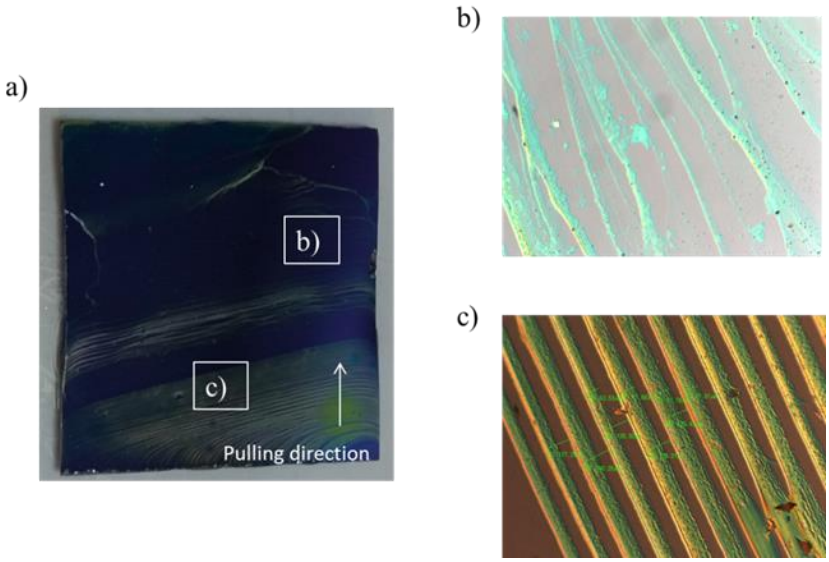

*Figure 3.1.22: **(a)** Image from the sample GHR0403 (u = 500nm/s, T = 60˚C). The direction of withdrawal is also presented with the white arrow. **(b)**, and **(c)** Images from the optical microscope from the respective areas depicted with white boxes in (a) on the surface of the sample.*

In Figure 3.1.23 the area between two adjacent thick “lines” of material deposition is shown. A significant amount of material is contained at the border of the “line”, less near the border, and small traces at the area before the beginning of the next line form deposition. The area with the small traces was also investigated by SEM measurements (Figure 3.1.23 b).

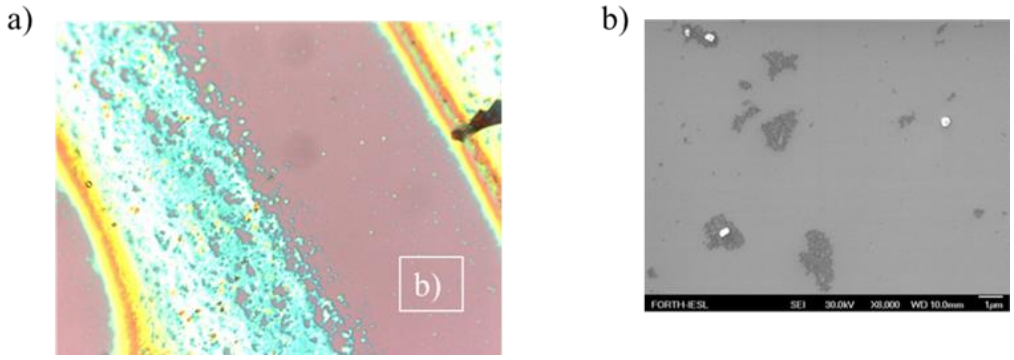

Figure 3.1.23: ***(a)*** *Images from the optical microscope for the area between two adjacent “line” forms of agglomeration for the sample GHR0403 (u = 500nm/s, T = 60˚C).* ***(b)*** *SEM image of the area depicted with the white box in (a).*

Considering the results emerged by the dip – coating method, inhomogeneity in MoS_2 deposition was observed to all the aforementioned samples. Further investigation is needed for the temperature conditions and the withdrawal speed in order to achieve more homogeneous deposition preferable for the good performance of devise operation. In the case of low temperature (T = 20˚C) the combination of high pulling speed (u = 500nm/s) with the fact that the substrate was hydrophilic (with O_2 plasma treatment) may led to the washout of the material leaving the substrate with thick traces of the material, during the withdrawal. As a result, an inhomogeneous deposition took place for the sample GHR0407. The lowering of the pulling (withdrawal) speed seemed not to be efficient as well, regarding the results for the samples made with u = 250nm/s, and u = 125nm/s, under T = 20˚C – GHR0405 and GHR0410, respectively. In the case of high speed (u = 500nm/s) we tried to gain efficient adhesion of the material to the substrate by increasing the value of temperature. According to the respective results from samples made under T = 40˚C and T = 60˚C even though a significant amount of material was observed to stick on

the substrate, the deposition was not again homogeneous and undesirable of device fabrication.

3.3 Filtration

For the deposition of MoS_2 by the filtration method, vacuum is at first, created in the flask using rubber tubing connected to a vacuum source. Then, a small amount of the solution (3mL) containing MoS_2 flakes is poured into the cylinder tube. The liquid is pulled down to the filter through atmospheric pressure. The MoS_2 flakes remain on the surface of the filter while the solvent passes through and ends up into the flask. A small amount of isopropanol (3mL) is poured afterwards, in order to remove any particles (surfactant) which may have been attached on the MoS_2 flakes. Finally, water is inserted on the cylinder (30ml) to draw away all the remaining elements (isopropanol and surfactant) and leave the filter with the material on the surface. (see set up in section 2.2.3)

The following step is to transfer the deposited material from the filter onto the Si/SiO_2 substrate. In order to achieve that, the filter is removed from the plastic base and dipped into methanol for 1 minute, before been deposited on the substrate. Methanol prevents air molecules to penetrate the pores of the filter which could create bubbles when the filter is immersed into acetone (next step), leading to destruction of the deposition. For that purpose we use methanol which causes no destruction either to the filter or the deposition. The side of the filter containing the material is then placed on the substrate. The sample is placed but not immersed into a beaker containing acetone which is put on a hot plate and heated at T = 80˚C, afterwards. The acetone vapors, created under this temperature, start to dissolve the filter. When the filter is completely soaked in acetone, it is placed in the acetone bath to completely dissolve the filter material. The beaker is then removed from the hot plate.

The removal of the filter was attempted by three different ways. The first attempt was made by slowly wetting the sample with small droplets of acetone. The second was by holding the sample within stirring acetone in order to draw away the

layer of the filter. The last attempt was by leaving the sample into acetone for 1 hour without any treatment. The filter used in this process (made of cellulose ester) contains pores of 50nm in diameter. Small MoS_2 (smaller than the porous diameter) flakes were trapped within the filter resulting in the delamination of the MoS_2 film from the substrate during the removal of the filter in all three attempts described previously. As a result, we did not manage to create a large – area of material deposition needed for the device fabrication through the filtration method.

- ***Conclusion for the deposition methods***

In conclusion, dip – coating and filtration methods appeared to be less efficient techniques for homogeneous deposition of the material compared to drop – casting method, and they were not employed as the first step of device fabrication in this work.

Chapter 4 - Electrical and optical characterization – Results

4.1 - Sample: MoS2_det_01

In the following section the fabrication process, the electrical and optical measurements for the device operation, are discussed in details for detectors of the sample named MoS2_det_01.

4.1.1 Fabrication by e– beam lithography

In order to investigate the electrical and optical response of photodetectors based on few – layered MoS_2, a considerable amount of devices had to be patterned onto the sample containing MoS_2 flakes all over its surface. For that purpose a design including 576 patterns, was made.

In this design the devices were separated in 12 periods. Each period consists of 8 different columns with 6 devices in each column ((a) – (f) from bottom to top – Figure 4.1.1) resulting in 48 devices in total. The rows from 1 to 7 contain detectors with 8 different patterns. Each detector differs in the number of the inter – digitated metal contacts (fingers) and in the distance between each pair of metal contacts (finger separation) – length of the channel. The devices in the same column (a – f) are constructed with the same characteristics (same number of fingers and channel length).

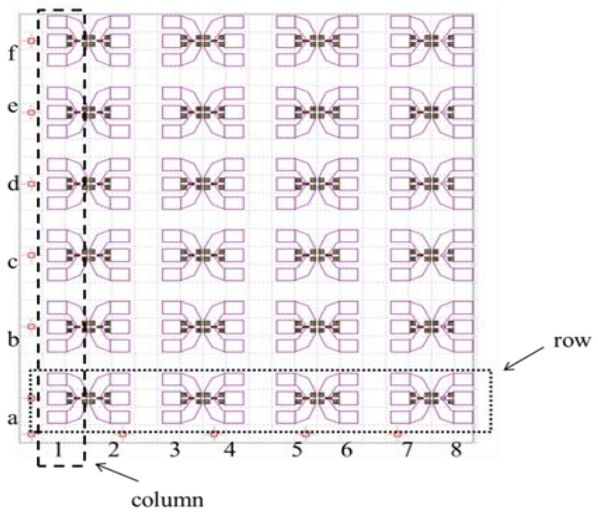

Figure 4.1.1: Schematic representation of a period containing 6 detectors at a column and 8 detectors at a row (48 devices in total).

Devices in the columns 1, 2, and 3 contain 16, 8, and 4 metal fingers respectively with a 150nm separation between fingers. Devices in columns 4, 5, 6, and 7 are made of 4 metal fingers with different finger separation – channel length – from 450nm to 300nm (Table 2). The devices at the last 8th column include short – circuit and open – circuit devices used as reference. Table 2 represents all the different patterns of the detectors.

Table 2: The characteristics of the MoS_2 detectors at each column from 1 to 7.

Column number	Number of fingers (channel length = 150nm)
1	16
2	8
3	4
Column number	Channel length(nm) (4 metal fingers)
4	450
5	400
6	350
7	300

The patterning of such a nano – scale structure was achieved using electron beam lithography (EBL) which has already been discussed (see section 2.1.3).

The sample made by this technique is named "MoS2_det_01" and the fabrication steps are described as follows. Big droplets of the dispersion containing MoS_2 flakes are at first, deposited on Si/SiO_2 (SiO_2 had thickness of 290nm) substrate by the drop – casting method. A bilayer of positive resist PMMA A4 495 and PMMA A2 950 is then deposited on top of the substrate with MoS_2 flakes, via spin - coating. Each layer is baked, after deposition, up to 130˚C. Electron beam lithography is next performed on the sample. After the exposure the sample is placed in MIBK: IPA (1:3) developer and the exposed regions of PMMA are removed. The following step is the metal deposition (metallization). This process consists of the deposition of Ti/Au and Pt/ Au as the two asymmetric metal contacts with 30nm thickness for each contact. The sample is then immersed into acetone in order to remove the remaining PMMA and the needless metal layer (lift – off process). Due to the fact that MoS_2 is deposited all over the surface of the substrate, a dry etching step is then performed in order to remove the remaining material outside the device area. For that purpose an etching mask is patterned through e – beam lithography in negative resist N2403 and then MoS_2 is etched in Cl_2 and BCl_3 mixture. Finally, Au pads (coplanar wave guide - CWG), are patterned as the last step of e – beam lithography, with a thickness of 300nm.

The design of the device as a result of this process is presented in the following image (Figure 4.1.2 a). The purple regions correspond to the Au metal pads and the rectangular box indicates the active area of the device (Ti and Pt metallization with the material underneath). The blue color corresponds to the Ti and the green color to the Pt metal fingers.

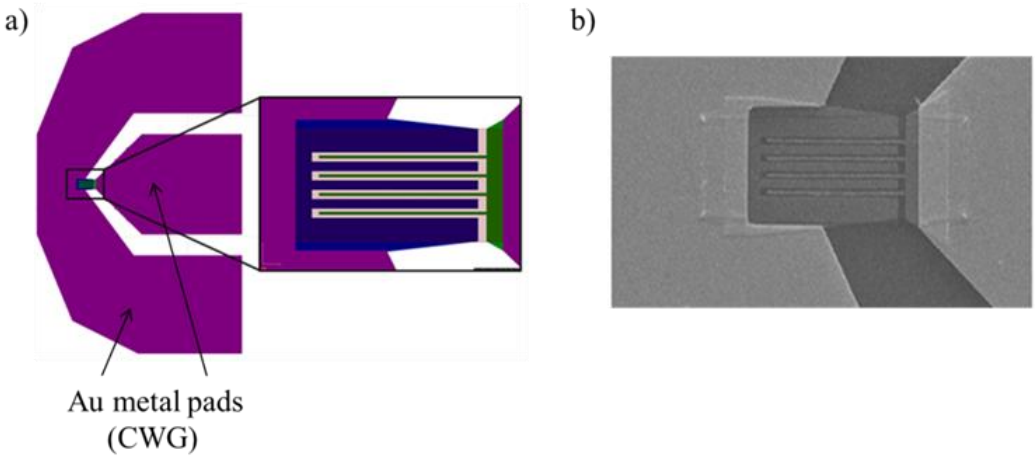

Figure 4.1.2: ***(a)*** *Representation of the design and the active area of the device. The blue and green areas in the box correspond to the Ti and Pt metal contacts, respectively.* ***(b)*** *SEM image from the active area of the detector constructed by 4 metal fingers.*

4.1.2 Electrical characterization

The sample MoS2_det_01, containing MoS_2 after drop – casting deposition on plasma treated Si/SiO_2 (see section 3.1.1 – O_2 plasma treatment) was used for patterning of photodetecting devices by e – beam lithography. An asymmetric metallization was employed by the use of two different metal contacts, Ti/Au and Pt/Au. Pt electrode was applied to MoS_2 as a high work function metal with $\Phi_{Pt} = 5.65$ eV while Ti electrode was applied as a low work function metal with $\Phi_{Ti} = 4.33$ eV. The following image (Figure 4.1.3) indicates the band alignment of the device with Pt/Ti asymmetric metal electrodes applied to MoS_2 channel. The work function of MoS_2 is at a range of 4.48 – 5.2eV. [31]

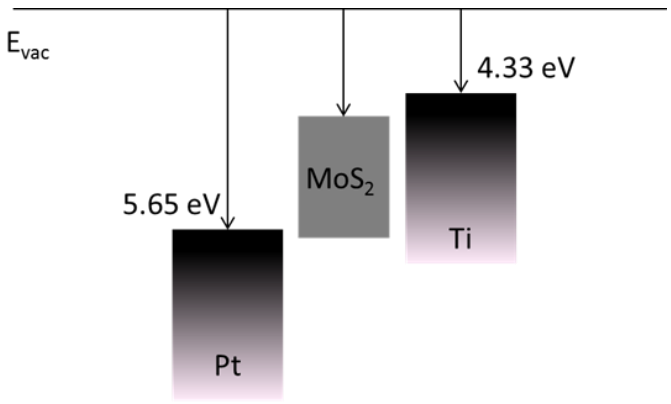

Figure 4.1.3: Schematic band alignment for asymmetric Pt/Ti metal contacts at both edges of MoS_2 channel.

I – V characteristic of a device containing 8 fingers is shown in the next figure (Figure 3.2.2). At the metal/semiconductor junction, the Schottky barrier height is related to the difference between the work function of the metal and the electron affinity of the semiconductor, i.e. $\Phi_B = \Phi_M - \chi$. However, MoS_2/Ti interface was estimated to provide an Ohmic contact ($\Phi_{Ti} < \Phi_{MoS_2}$). On the other hand, MoS_2/Pt junction was estimated to offer a quite high Schottky barrier due to the high work function Pt electrode. Since the devices with a metal – semiconductor – metal configuration, with one Schottky contact on one side (MoS_2/Pt) and Ohmic contact on the other side (MoS_2/Ti), carriers were expected to be controlled only by the high Schottky barrier at the MoS_2/Pt interface, and a more rectifying behavior of the I – V curve was expected according to this asymmetric metallization. However, a symmetric I –V curve was measured, as it is shown in Figure 4.1.4. This can be explained as follows. Firstly, MoS_2/Ti interface appears to offer a Schottky instead of Ohmic contact. Furthermore, electron affinity of MoS_2 is a thickness dependent feature. It increases as the thickness of MoS_2 flakes increase, as has recently been reported [40]. Thus, for the multilayer form of MoS_2 in our case, the Schottky barrier between the high work function metal – Pt – and MoS_2 may be smaller and comparable to the Schottky barrier between the low work function metal – Ti – and MoS_2, resulting in such a symmetric I – V curve. [49]

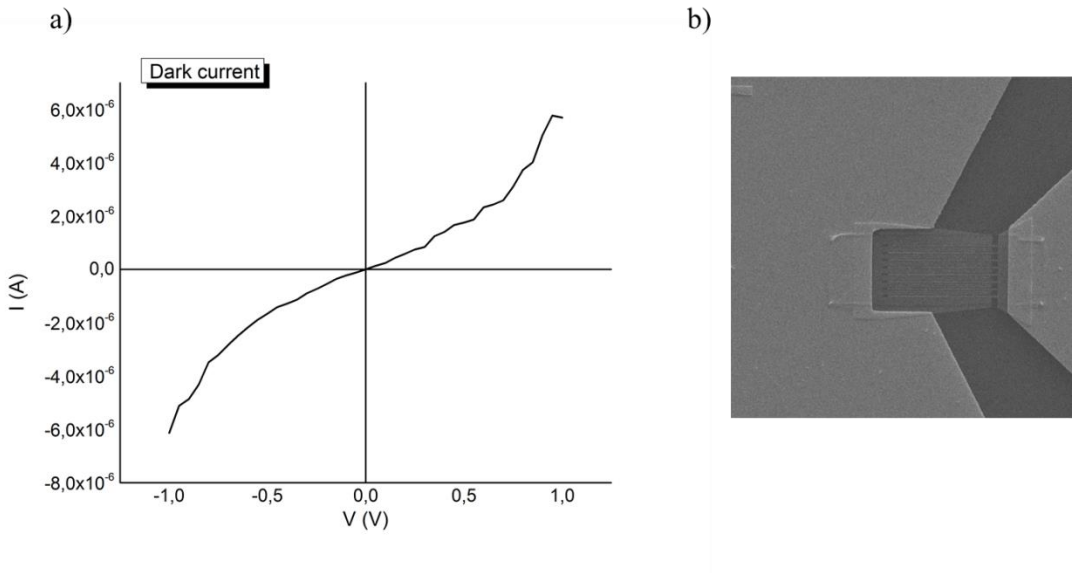

Figure 4.1.4: ***(a)*** *I – V characteristic for the asymmetric contact (Pt/Ti) device with 8 metal fingers without illumination (dark current).* ***(b)*** *SEM image of the corresponding device measured in (a).*

This symmetric behavior can be observed more clearly in the following figure (figure 4.1.5) were the y – axis contains the absolute values of the output current in logarithmic scale.

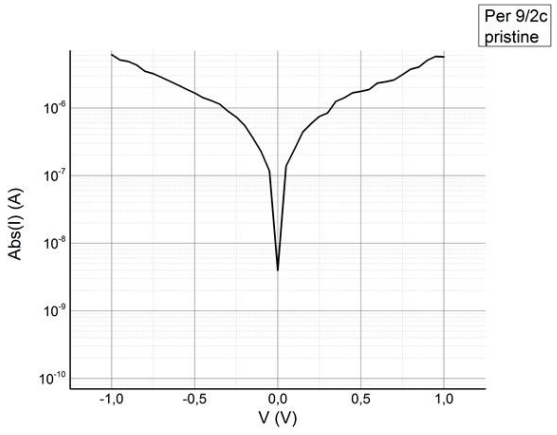

Figure 4.1.5: I –V characteristic for the asymmetric contact (Pt/Ti) device with 8 metal fingers in semi – log scale.

In Figure 4.1.6 the I – V characteristics for devices with different patterning are also presented. Almost the same symmetric behavior was observed to all of these devices. In (a) the device has a 4 finger patterning with 150nm channel length, in (b) and (c) the devices contain 4 fingers with 350nm and 300nm channel length respectively (Table 2). For the measurements presented in figures 3.2.3 and 3.2.4 the applied voltage is at the range of -1V to 1V with a step of 0.05V.

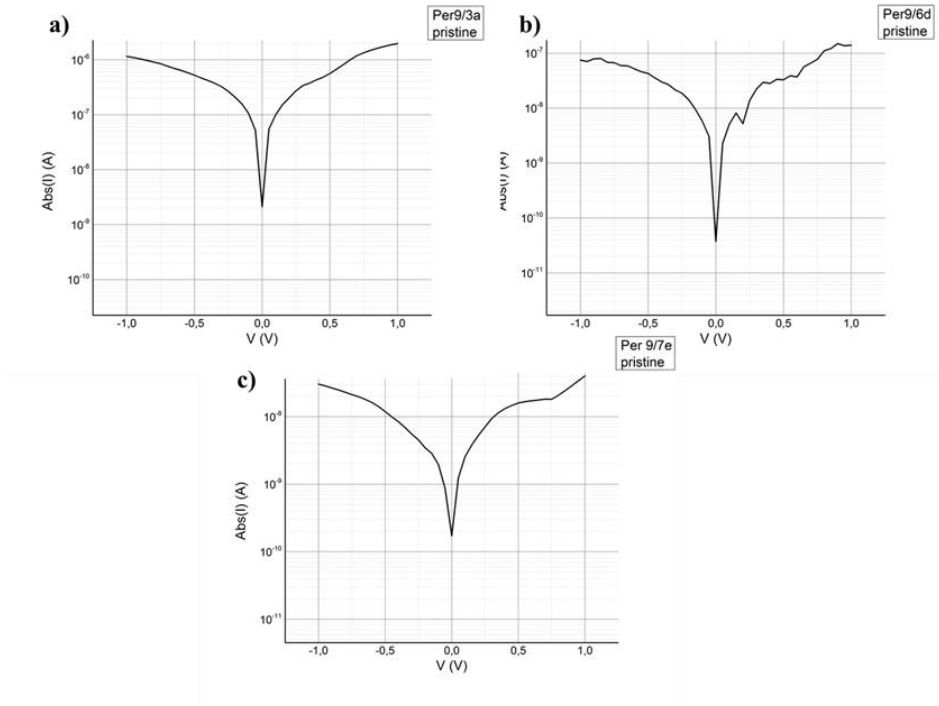

Figure 4.1.6: I – V characteristic for devices with Pt/Ti asymmetric metal contacts and different channel lengths. ***(a)***, ***(b)***, *and* ***(c)*** *correspond to 150nm, 350nm, and 300nm channel lengths, respectively.*

4.1.3 Annealing process

In order to investigate the effect of annealing on our devices we cut the sample (MoS2_det_01) into 2 two pieces and one of these was annealed at a temperature of T = 250˚C for 5 minutes in H_2/N_2 atmosphere (forming gas). In the following figures, Figure 4.1.7 and Figure 4.1.8, the comparison between pristine and annealed devices is presented. The diagrams include the absolute values of current in logarithmic scale since the impact of the annealing process on the devices is more evident. The first device presented is the same as in Figure 4.1.4 (b).

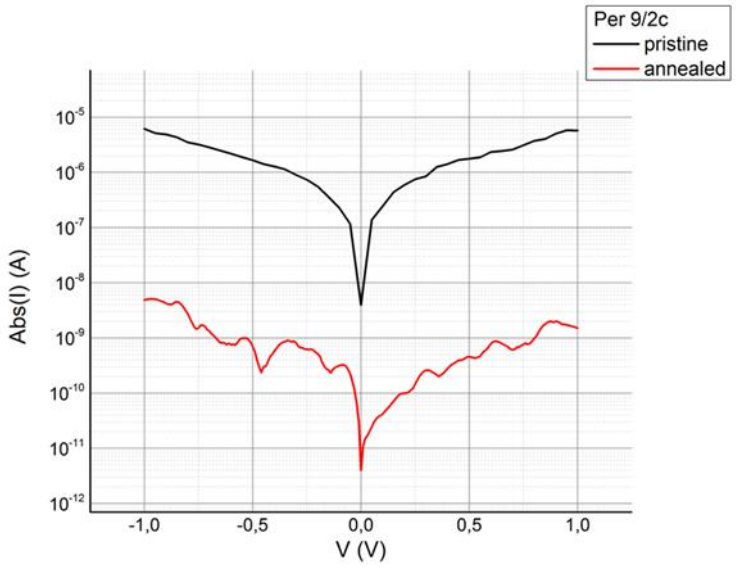

Figure 4.1.7: I – V characteristic of the Pt/Ti contact device with 8 metal fingers. The black curve corresponds to the device before annealing (pristine device) and the red curve to the same device after the annealing process.

Figure 4.1.8 indicates the corresponding I – V characteristics before and after annealing for the devices presented in Figure 4.1.6 (b) and (c). In all the measurements the applied voltage is at the range of -1V to 1V with a step of 0.01V.

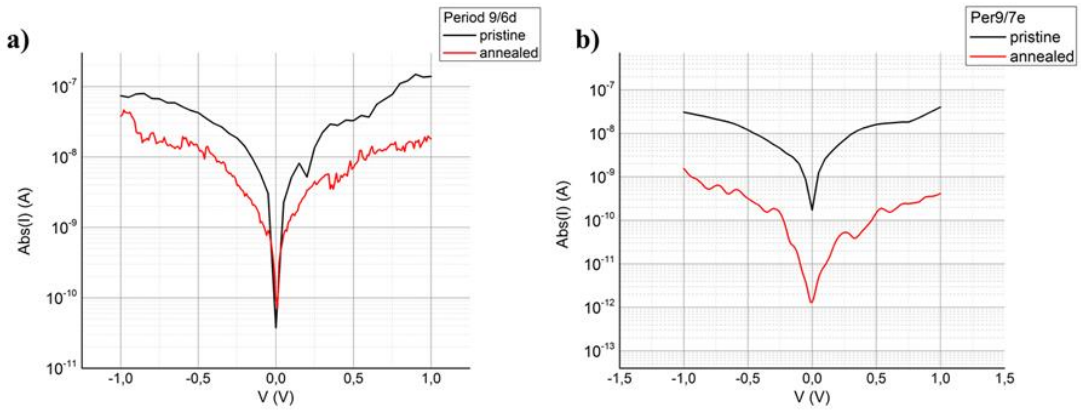

*Figure 4.1.8: I – V characteristics for devices with 4 metal fingers and channel length of 350nm **(a)** and 300nm **(b)**.The black and red curves correspond to pristine and annealed devices, respectively.*

As can be observed from all the above diagrams, there is a difference in the output current. The symmetric I – V curve from the pristine (without the annealing process) samples can be also attributed to a thin layer of undesirable material that exists at the metal/MoS_2 interface. With the annealing operation a part from this material has been dissolved leading to more theoretically expected results as it can be observed from the asymmetry of the red curves from the respective diagrams (Figures 4.1.7, and 4.1.8). Moreover, the current values after the annealing process have been reduced compared to the respective values of the pristine samples. This fact is a result of the reduction of dopants on the surface of MoS_2 which make the material less conductive. Therefore, annealing process is an efficient method to employ after the device fabrication steps used in this work, which leads to more expected results according to theory and previous works. [49]

Another device was also tested revealing a different behavior as can be observed from the comparison of the I – V curves (Figure 4.1.9) without and after the annealing process.

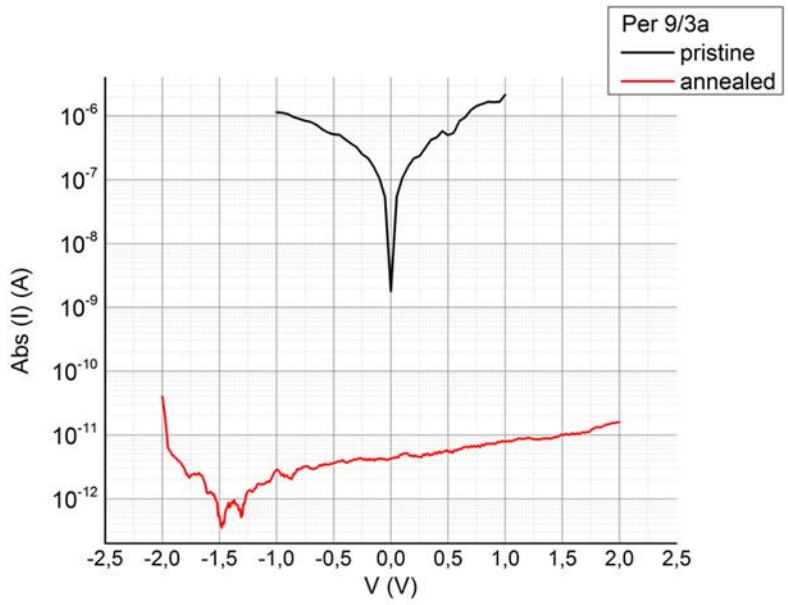

Figure 4.1.9: I – V characteristic of the device with 4 metal fingers and 150nm channel length. The black curve is for the pristine device and the red curve is for the device after annealing.

A shift of the minimum value of current is observed at V = -1.48V. A voltage at the range of -2V to 2V had to be applied in order to reveal this shift. This fact can be attributed either to the impact of the metal/MoS_2 junction which leads to a built – in electric field at the interface or to the impurities that act like dopants at the interface.

In Figure 4.1.10 the measurement of hysteresis for this device, is shown. Large hysteresis was observed leading us to the conclusion that the contribution of the impurities is higher than the metals.

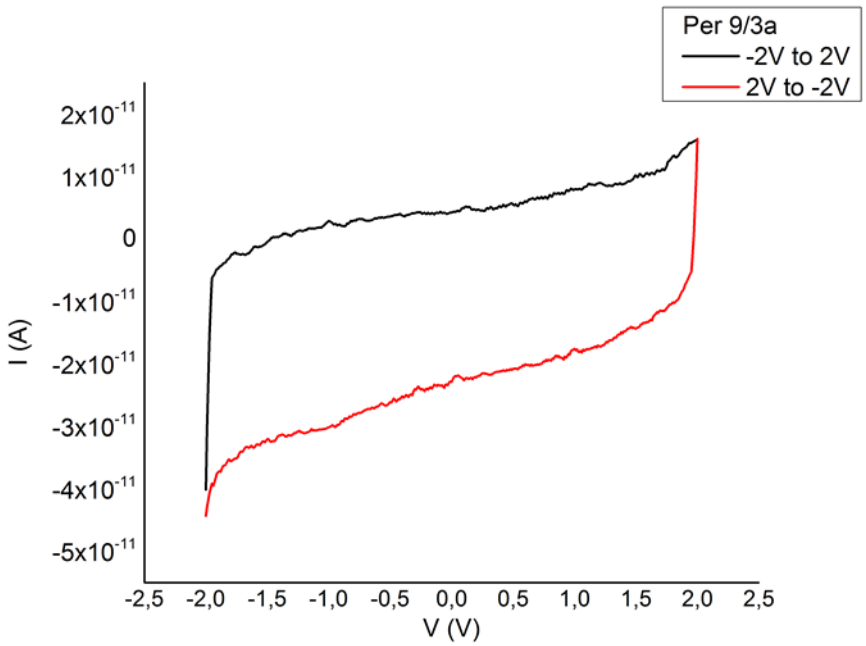

Figure 4.1.10: I – V characteristics for hysteresis test of the device with 4 metal fingers and 150nm channel length. The black curve corresponds to voltage sweep from -2V to 2V and the red correspond to voltage sweep from 2V to -2V.

4.1.4 Optical measurements

In order to study the response of the devices described above under illumination a CW laser beam was used with a wavelength of λ = 405nm (E = 30,6eV), circular spot size with diameter d = 1413μm and maximum incident optical power P_{inc} = 12,5mW. The active area of the device is 240μm^2 (Figure 2.11) and the illuminated area on the sample is estimated to be ~1,57mm^2, thus the active area of the photodetectors was fully illuminated. All the measurements discussed in this section have been taken under zero external bias and ambient conditions.

In Figures 4.1.11 and 4.1.12 the photoresponse of the devices to incident optical power is presented. Six Neutral density filters were used for the reduction of incident power with corresponding numbers 3, 2, 1, 0.5, 0.3, and 0.1 and the output power was calculated through the equation

$$P = \frac{P_0}{10^{ND}} \tag{3.1}$$

where P_0 is the incident laser power (without filter) and ND is the number of the filter.

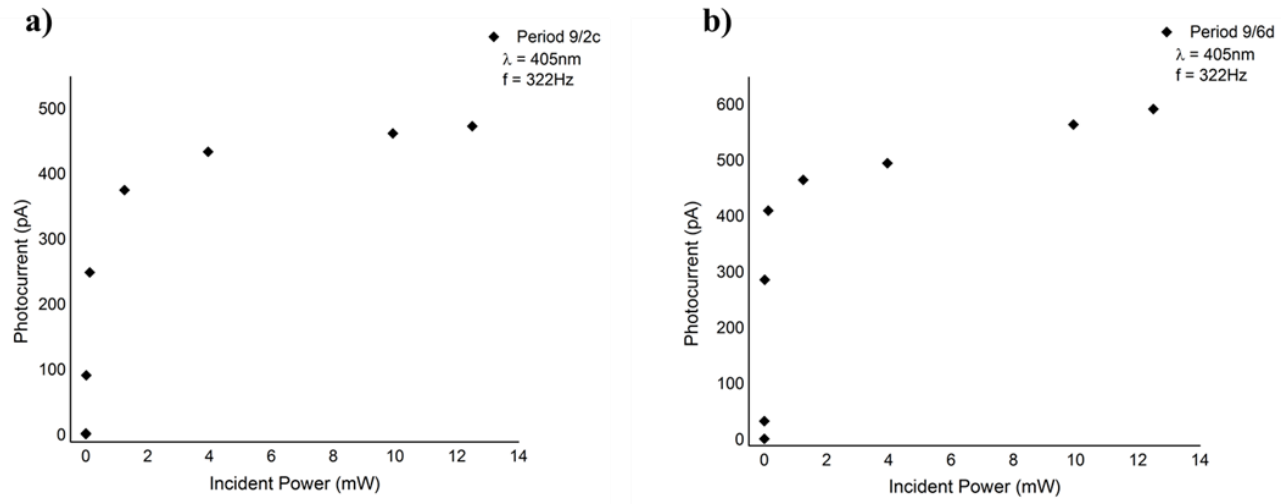

Figure 4.1.11: Photocurrent as a function of incident power. ***(a)*** *Device with 8 metal fingers and 150nm channel length.* ***(b)*** *Device with 4 metal fingers and 350nm channel length. Modulation frequency f= 322Hz and maximum incident power P_0 = 12,5mW.*

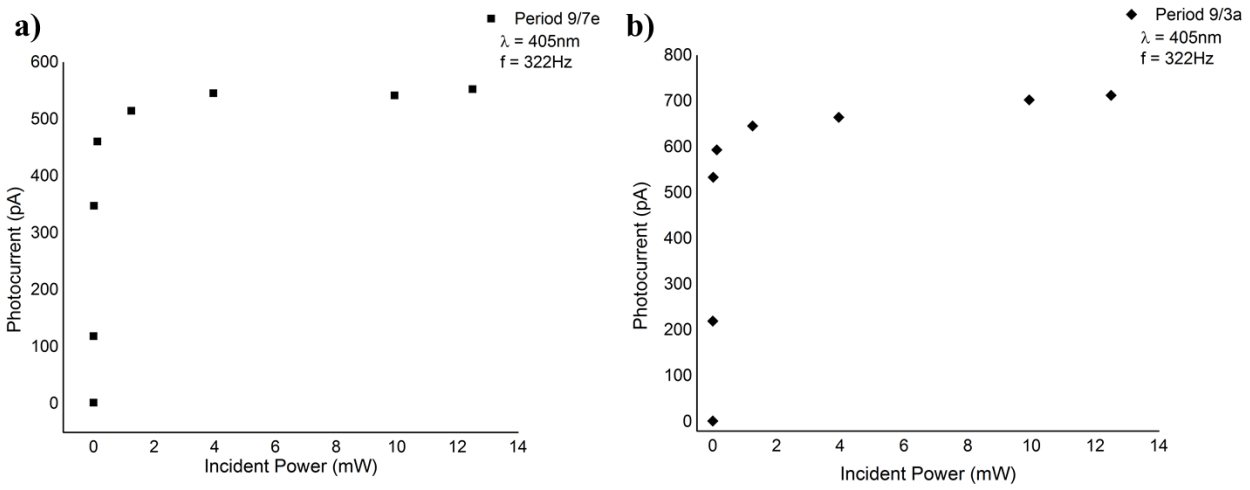

Figure 4.1.12: Photocurrent as a function of incident power. ***(a)*** *Device with 4 metal fingers and 300nm channel length.* ***(b)*** *Device with 4 metal fingers and 150nm channel length. Modulation frequency f= 322Hz and maximum incident power* P_0 *= 12,5mW.*

The non – linear power dependence of photocurrent may arise from the existence of a significant amount of trap states within the material due to the inevitable disorder caused by the random stacking among the layers of the liquid exfoliated flakes as it has already been observed in previous works. [29] Another phenomenon that may contribute to the non – linear photocurrent dependence to incident optical power is the contribution of the silicon substrate.

In column 8 of the pattering, the devices were fabricated without containing the active material (without MoS_2) and with no metal fingers. These devices were measured in order to investigate the contribution of silicon substrate. In Figure 4.1.13 the photoresponse of such a referenced device is shown. As it can be observed there is a significant response of this open circuit device under illumination similar to the response of the aforementioned devices (Figures 4.1.11, and 4.1.12). Consequently, a significant amount of current is induced from silicon substrate which contributes to the overall photocurrent values.

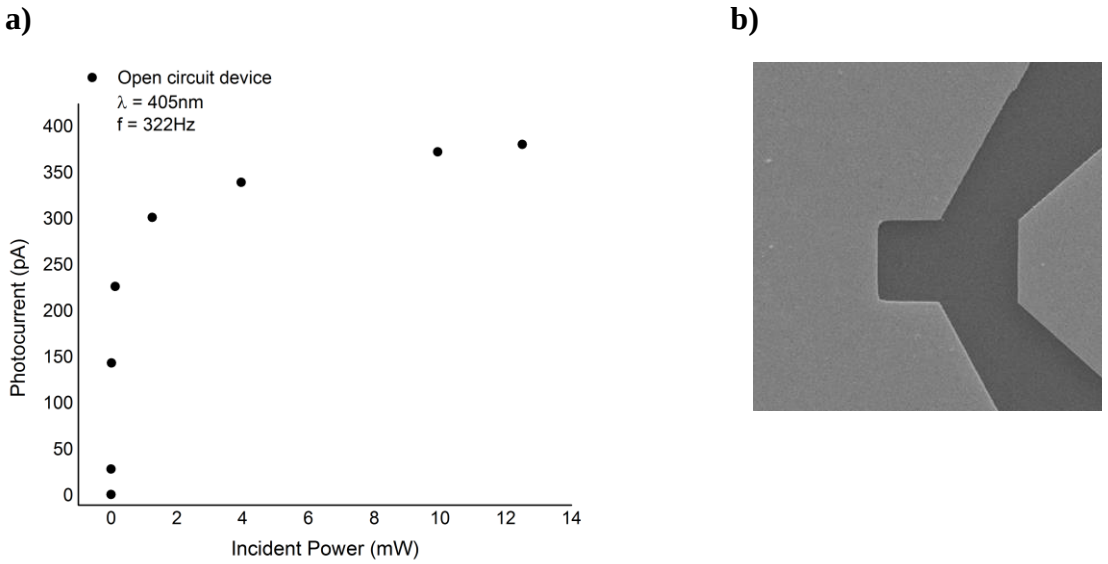

Figure 4.1.13: ***(a)*** *Photocurrent as a function of incident power of a reference device (open circuit device without metal fingers and without material. Modulation frequency f= 322Hz and maximum incident power* P_0 *= 12,5mW.* ***(b)*** *SEM image of the corresponding open circuit device.*

The contribution of silicon substrate is more evident through the photocurrent measurements to modulation frequency. The results are shown in the following figure (Figure 4.1.14) for a device with 16 metal fingers and 150nm channel length.

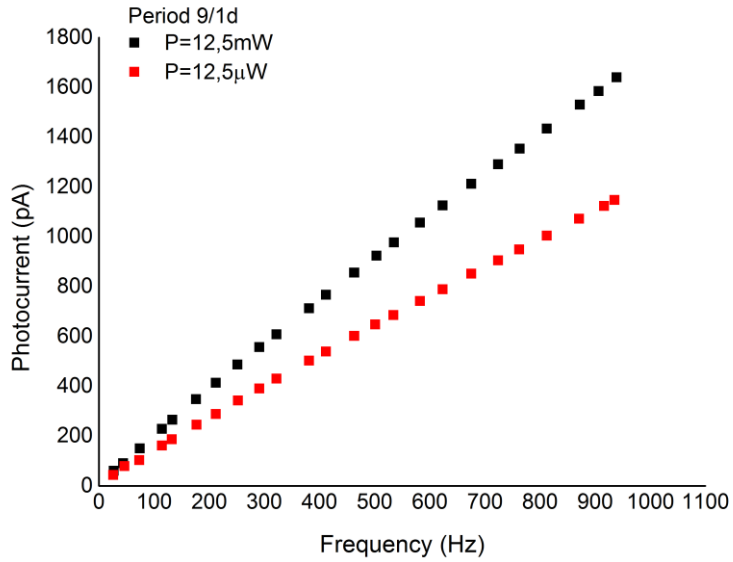

Figure 4.1.14: Photocurrent as a function to modulation frequency for device with 16 metal fingers and 150nm channel length. Black points correspond to measured photocurrent at P = 12.5mW incident power and red points to measured data at P = 12.5μW incident power.

An increase in photocurrent values is observed as frequency increases. This can be attributed to the fact that under alternating incident light (laser beam modulated by chopper) the device with a $MoS_2 – SiO_2 – Si$ arrangement is operating as a capacitor resulting in a significant photocarrier generation within the silicon substrate which eventually contributes to the measured output photocurrent values.

In order to evaluate the photocurrent values without the contribution of the silicon substrate we subtracted the photocurrent values of the reference device from the output photocurrent values measured for the corresponding devices. Figures 4.1.15 and 4.1.16 show the power dependence curves after this subtraction.

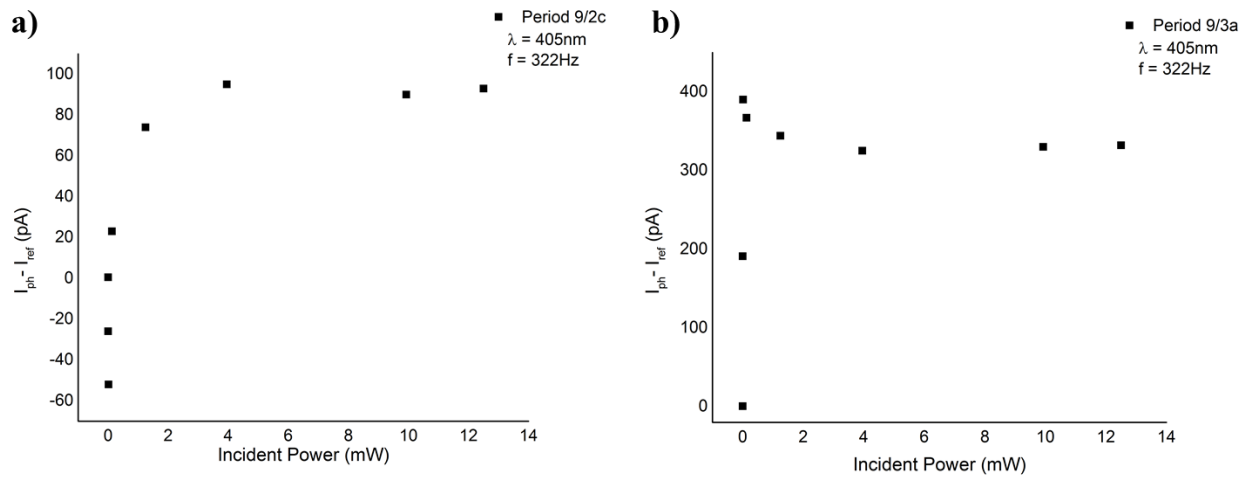

Figure 4.1.15: I_{ph} - I_{ref} as a function of incident power. ***(a)*** *Device with 8 metal fingers and 150nm channel length.* ***(b)*** *Device with 4 metal fingers and 150nm channel length. Modulation frequency f= 322Hz and maximum incident power P_0 = 12,5mW.*

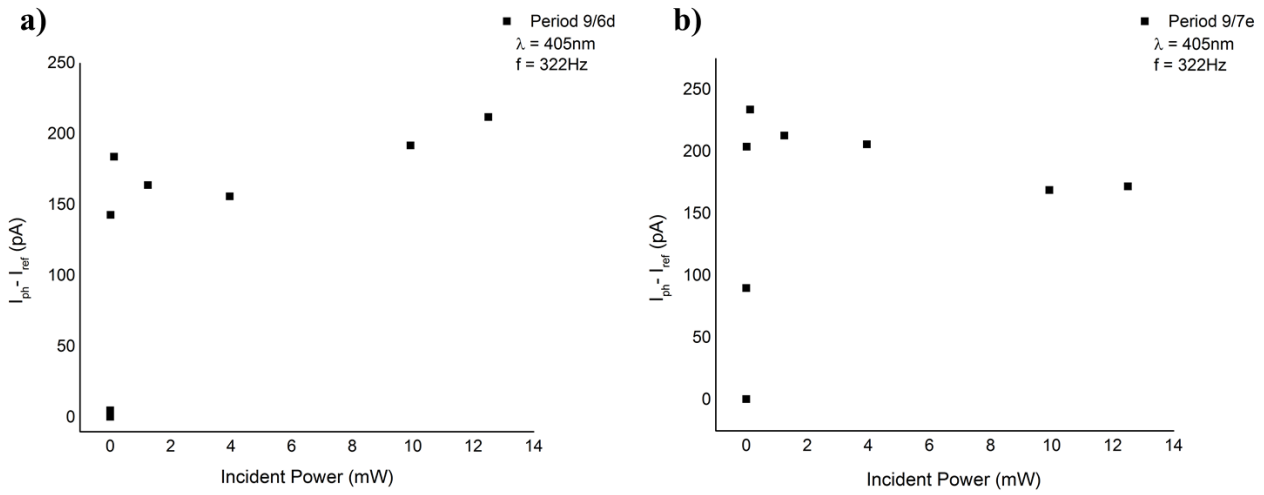

Figure 4.1.16: I_{ph} - I_{ref} as a function of incident power. ***(a)*** *Device with 8 metal fingers and 150nm channel length.* ***(b)*** *Device with 4 metal fingers and 150nm channel length. Modulation frequency f= 322Hz and maximum incident power P_0 = 12,5mW.*

The above results were not expected. A source of error is the part of optical power that eventually reaches the substrate which changes depending on the design and size of the inter – digitated detector. Thus, a more careful subtraction of the open circuit device used as reference would be needed to improve the accuracy of the corrected results. Another approach is to avoid the Silicon substrate all together. This has been achieved by using a glass substrate instead of silicon. E – beam lithography is much more difficult in the case of electrically isolating substrates thus an optical lithography mask was used in that case.

4.2 - Sample: MoS2_det_02glass

The following sections include the fabrication, electrical and optical (under illumination) results for the detectors of the sample named MoS2_det_02glass.

4.2.1 Fabrication by optical lithography

Regarding the fabrication of MoS_2 detectors on glass substrate (sample MoS2_det_02glass), the deposition of MoS_2 was made by drop – casting method with 5 big droplets on the substrate before metallization. Optical lithography was employed in order to fabricate MoS_2 photodetecting patterns. SU8 polymer was spin coated as photo – resist on MoS_2/glass substrate and baked for 1 minute. A metal – semiconductor – metal (M – S – M) configuration was then patterned with Au metal contacts. Inter – digitated Au electrodes of 9μm – width, 1575.5μm – long, and 150nm – thick were used for the M – S – M photodetectors. Figure 4.2.1 (a) shows the whole region of the photodetecting device containing the Au metal electrodes and the material underneath which can be observed more clearly in 4.2.1 (b). Figure 4.2.1 (c) represents a schematic of a single MoS_2 photodetector with the aforementioned construction.

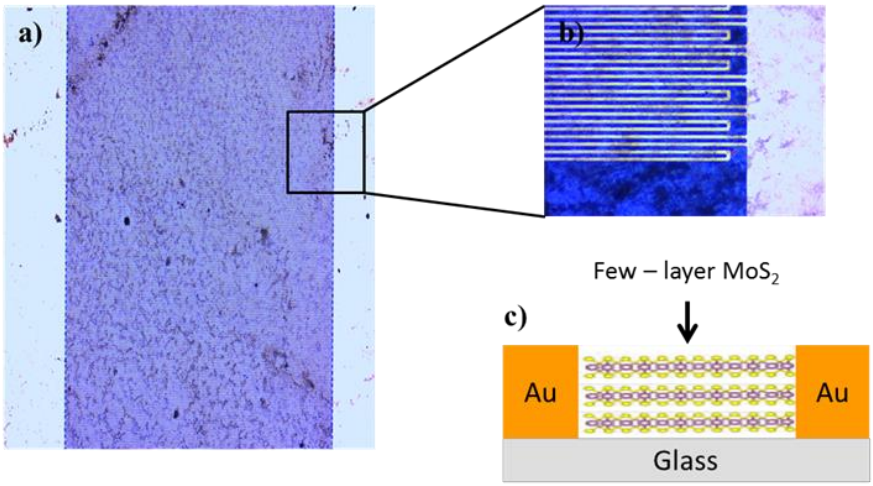

Figure 4.2.1: ***(a)*** *Image from optical microscope at the photosensitive region of a MoS_2 photodetecting device with 240 Au metal fingers.* ***(b)*** *Image corresponding to the respective area in the black box with greater magnification.* ***(c)*** *Schematic of a single MoS_2 photodetector with Au metal contacts on glass substrate.*

4.2.2 Electrical characterization

After fabrication, the device was electrically characterized by applying a voltage from -1V to 1V with a step of 0.01V. The electrical measurements were carried out with the use of Keithley Source meter (2400 SMU instrument) and all the measurements were taken at room temperature. The respective I – V characteristic of the device is shown in the next figure (Figure 4.2.2).

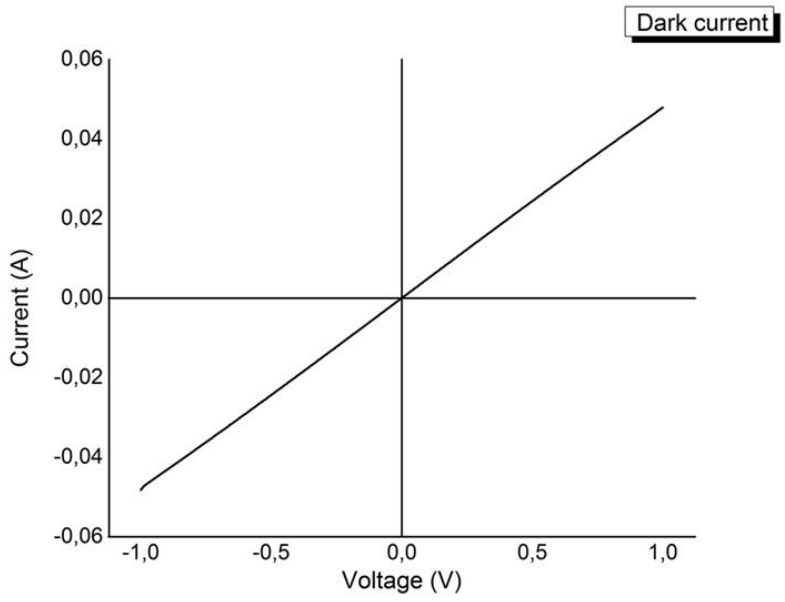

Figure 4.2.2: I – V characteristic of the device containing 240 Au metal fingers on top of MoS_2 with 3μm distance between fingers (channel length).

A symmetric behavior was observed as expected due to the symmetric Au metallization. A linear dependence of the output current is also shown as a function of the applied voltage indicating an ohmic – like Au/MoS_2 contact. The significant amount of metal electrodes (240 fingers) lead to a numerous metal – semiconductor – metal (M-S-M) configuration connected in parallel, giving rise to an enhanced overall current, as can be observed from the current values in the order of tens of mA (I_{max} = 48mA for V=1V).

From the slope of I – V curve, the resistance of the device can be extracted as follows,

$$slope = \frac{1}{R} \Rightarrow R = 20{,}7\Omega$$

Consequently, the pattern of a device with such a configuration leads to a really conductive photodetector.

4.2.3 Optical measurements

After electrical characterization, we probed the response of the device under illumination. A focused laser beam with a wavelength of λ = 405nm was used and an illumination power of P_{inc} = 12,6mW. The laser power was measured by a Power meter (Newport) which was placed at the location of the sample without the chopper. Power meter is calibrated to every wavelength in order to measure the exact value of the optical power. A voltage source was also used in order to apply a constant external voltage. The optical measurements were taken under two different conditions. At the first condition, the measurements were carried out without the use of the lens resulting in a spot size of 1mm in diameter (d_1) of the laser beam with incident optical power $P_{inc,1}$ = 12,6mW. Under the second condition, we used a lens resulting in a laser spot size of 750μm in diameter (d_2) and incident optical power $P_{inc,2}$ = 10,7mW. The following figure (Figure 4.2.3) depicts the dependence of photocurrent as a function of the applied voltage under these two different conditions.

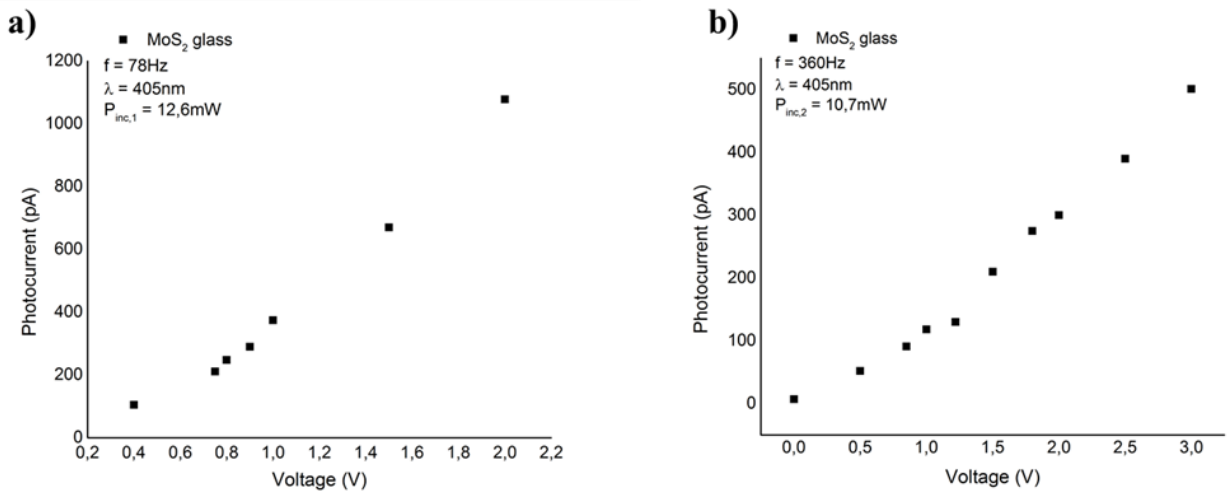

Figure 4.2.3: Photocurrent as a function of the applied voltage. ***(a)*** *Voltage range of 0.4V to 2V, spot size diameter d = 1mm, frequency f = 78Hz, and* $P_{inc,1}$*=12,6mW .* ***(b)*** *Voltage range of 0V to 3V, spot size diameter d = 750μm, frequency f = 360Hz and* $P_{inc,2}$*=10,7mW.*

Figure 4.2.3 (a) corresponds to the measurements which were taken for a spot size of 1mm and a modulation frequency of 78Hz. The applied voltage was at a range of 0,4V to 2V. Figure 4.2.3 (b) corresponds to a spot size of 750μm, modulation frequency f = 360Hz and voltage range of 0V to 3V.

From the curves presented in Figure 4.2.3, an increase of photocurrent is shown as the applied voltage increases. This result is attributed to the fact that as the applied voltage increases the drift velocity of the photogenerated carriers (electron – hole pairs created under illumination) increases with a related reduction of the carrier transit time (time that carriers need to travel through the channel before recombination) which is defined as:

$$T_{tr} = \frac{l^2}{\mu V} \tag{3.2}$$

where l is the length of the channel, μ is the carrier mobility and V is the applied voltage. [26] If all the photogenerated carriers could reach the electrodes, the photocurrent would result in a maximum constant value and saturation could be observed under a specific value of applied voltage. However, only a portion of these

carriers actually reaches the electrodes contributing to the photocurrent while the biggest part recombines within the channel. As a result no saturation was observed at the corresponding curves.

The dependence of photocurrent as a function of modulation frequency of the laser beam was the next step of our investigation. Two different chopper wheels were used for this kind of measurements. The first was a chopper wheel with 10 chopper blades and a range of 20Hz to 1kHz while the second chopper wheel contained with 30 chopper blades and a range of 20Hz to 3kHz. The applied voltage in both cases was V = 1V. In the next figure (Figure 4.2.4) the results of these measurements are inserted. In Figure 4.2.4 (a) the laser beam has a spot size of 1mm and in (b) it has a spot size of 750μm.

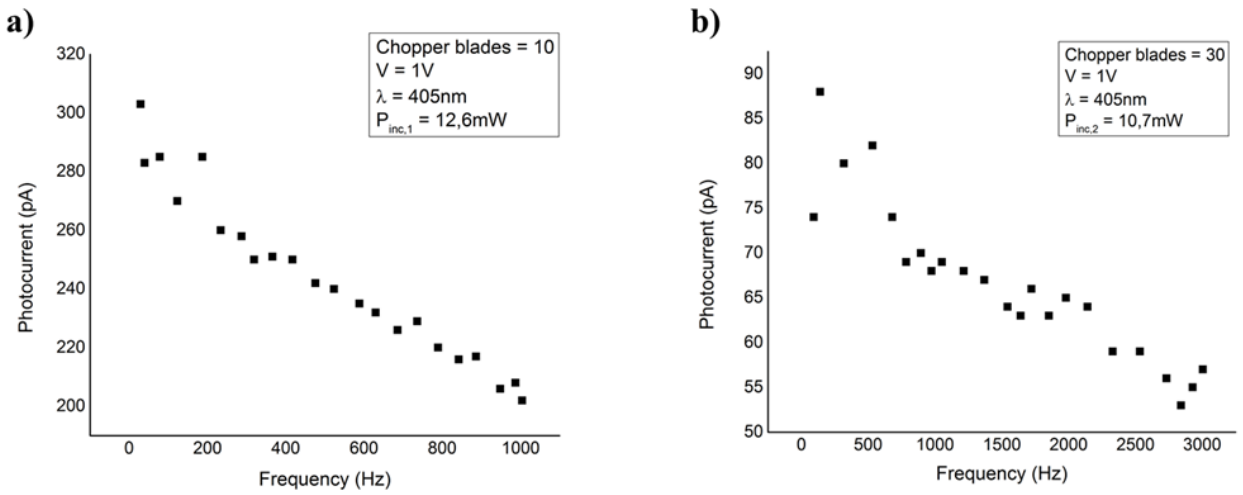

Figure 4.2.4: Photocurrent as a function of modulation frequency. ***(a)*** *10 chopper blades and a range of 20Hz to 1kHz (spot laser beam diameter d_1=1mm, $P_{inc,1}$=12,6mW).* ***(b)*** *30 chopper blades and a range of 20Hz to 3kHz (laser beam diameter d_2=750μm, $P_{inc,2}$=10,7mW).*

A reduction of the photocurrent values can be observed in both cases. This fact could be attributed to the existence of a significant amount of trap states within the channel which prevent the device from exhibiting a fast response. As the frequency of the chopper wheel increases the ON state (under illumination) occurs so fast that a significant part of the photogenerated carriers cannot manage to quench the traps

existing in the material resulting in a decrease of the output photocurrent as the frequency increases.

To clarify the photocurrent generation as a function of incident power in both conditions (different laser spot sizes: d_1 =1mm and d_2 = 750μm and different incident power $P_{inc,1}$ = 12,6mW and $P_{inc,2}$ = 10,7mW), power dependence measurements were performed. For this kind of measurements neutral density (ND) filters were used with the corresponding numbers ND: 3, 2, 1, 0.5, 0.3, and 0.1.

For d_1 = 1mm the illumination area (area of the laser spot) is $A_{spot,1} = \pi \cdot R^2$ = 0,7854mm^2 ,and for d_2 = 750μm the corresponding area of illumination is $A_{spot,2}$ = 0,4418mm^2. The photosensitive region of the detector (the area including the metal fingers and the material underneath) is calculated from the design of the patterns as A_{det} = 4,5591mm^2. Consequently, the laser spot in both cases illuminated a region inside the photosensitive area of the device ($A_{spot} < A_{det}$). Figure 4.2.5 shows the dependence of photocurrent (I_{ph}) as a function of incident laser power. The measurements were acquired under the applied voltage of V = 1V.

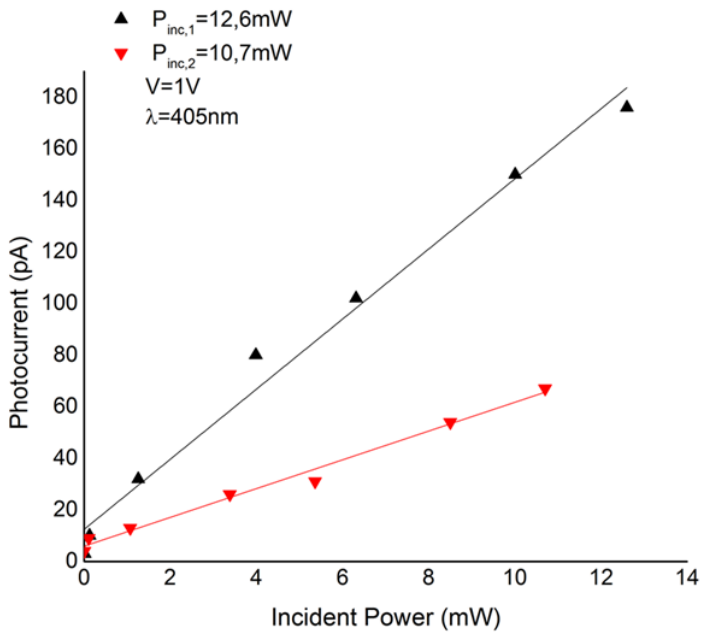

Figure 4.2.5: Dependence of photocurrent on incident laser power for bias voltage V = 1V. The black points correspond to laser spot d_1 = 1mm at a frequency f = 328Hz and the red points correspond to laser spot d_2 =750μm at a frequency f = 334Hz. The red solid lines show the linear fit.

From the slope of the above curves we can extract the external photoresponsivity - R_{ext} of our device which is defined as

$$R_{ext} = \frac{I_{ph}}{P_{inc}} \text{ (in the order of nA/ W)} \quad (3.3)$$

where I_{ph} is the generated photocurrent and P_{inc} the incident power of the laser beam. The calculated results are presented below (see section 1.5).

- For $P_{inc,1}$ = 12,6mW (black points) the external responsivity is $R_{ext,1}$ = 13,59nA/W.
- For $P_{inc,2}$ = 10,7mW (red points) the external responsivity is $R_{ext,2}$ = 5,58nA/ W.

Another important parameter except for the external responsivity for our detectors is the internal responsivity (R_{int}) i.e. the responsivity that can be extracted by the dependence of photocurrent as a function of the laser power incident to the active area of the device – P_{act}. The active area (A_{act}) is the total region of the device containing the active material – MoS_2 (light blue area of Figure 4.2.6).

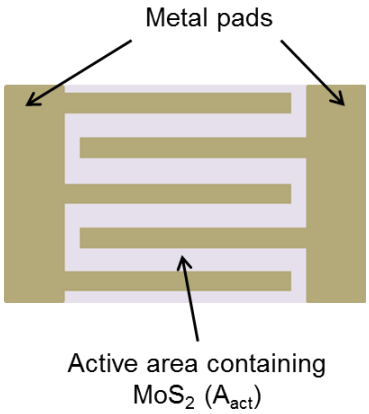

Figure 4.2.6: Schematic representation of the active area of the device (light blue area) containing the active material (MoS_2).

This area was found to be A_{act} = 1,134mm^2 (calculated from the design of the detector patterns). Thus, P_{act} can be evaluated from the equation

$$P_{act} = P_{inc} \cdot \frac{A_{act}}{A_{\det}} \tag{3.4}$$

where P_{inc} is the power of incident laser beam, A_{act}, the active (photosensitive) area of the device and A_{det} is the entire illuminated area of the detector (including the metal fingers). The dependence of photocurrent as a function of power of incident light on the active area - P_{act} is shown in the next figure (Figure 4.2.7).

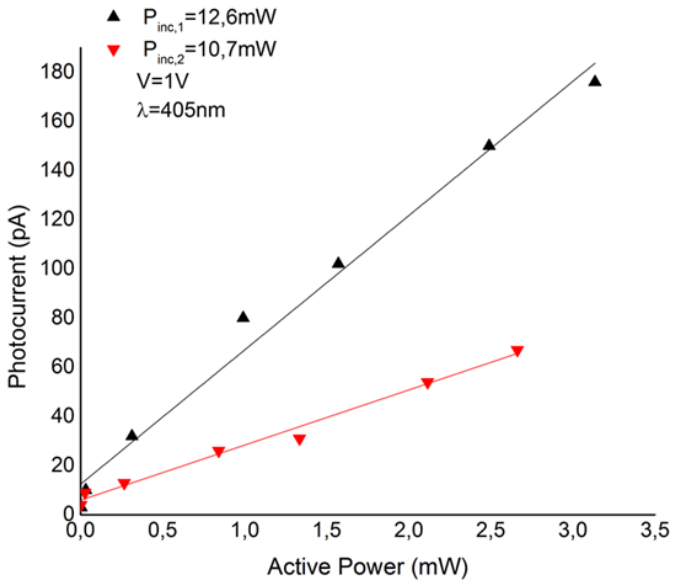

Figure 4.2.7: Dependence of photocurrent as a function of laser power onto the active area of the device (P_{act}) for bias voltage V = 1V. The black points correspond to laser spot d_1 = 1mm at a frequency f = 328Hz and the red points correspond to laser spot d_2 =750μm at a frequency f = 334Hz. The red solid lines correspond to linear fit.

The internal responsivity – R_{int} – can be extracted from the slope of the above curves in Figure 4.2.7 and the results for the two different values of incident power are presented below.

- For $P_{inc,1}$ = 12,6mW (black points),the internal responsivity is $R_{int,1}$ = 54,63nA/W.
- For $P_{inc,2}$ = 10,7mW (red points), the internal responsivity is $R_{int,2}$ = 22,43nA/W.

One of the most important figures of merit for a photodetector is quantum efficiency (QE) defined as

$$QE = \frac{I_{ph}}{q \cdot \phi} \tag{3.5}$$

where I_{ph} is the photocurrent, q is the unit electron charge, and φ is the photon flux. In order to evaluate QE we first have to calculate the photon flux which is the number of incident photons per second. It is defined as

$$\phi = \frac{P}{E_{ph}} \tag{3.6}$$

where P is the power of incident light and E_{ph} is the energy of a single photon (see section 1.5). For the laser beam with a wavelength of λ = 405nm the photon energy is

$$E_{ph} = \frac{1240}{\lambda(nm)} = \frac{1240}{405} = 3{,}06eV \approx 5 \cdot 10^{-19} J \tag{3.7}$$

If we take into account only the power of incident light that reacts we the active area of the device - P_{act}, from equation (3.6) we have

$$\phi' = \frac{P_{act}}{E_{ph}} \tag{3.8}$$

For the maximum values of P_{act} calculated from equation (3.4) we have:

- $P_{act,1} = P_{inc,1} \cdot \frac{A_{act}}{A_{\det}} = 3{,}134mW$ (for $P_{inc,1}$ =12,6mW)
- $P_{act,2} = P_{inc,2} \cdot \frac{A_{act}}{A_{\det}} = 2{,}661mW$ (for $P_{inc,2}$ = 10,7mW)

So the respective photon fluxes are:

$$\phi'_1 = \frac{P_{act,1}}{E_{ph}} = \frac{3{,}134 \cdot 10^{-3}}{5 \cdot 10^{-19}} \approx 6{,}3 \cdot 10^{15}\ photons/\sec$$

$$\phi'_2 = \frac{P_{act,2}}{E_{ph}} = \frac{2{,}661 \cdot 10^{-3}}{5 \cdot 10^{-19}} \approx 5{,}3 \cdot 10^{15}\ photons/\sec$$

For the photon fluxes calculated above (φ'_1 and φ'_2) we can evaluate the external quantum efficiency EQE_1 and EQE_2 respectively. Therefore, the respective EQE_1 and EQE_2 for photon fluxes φ'_1 and φ'_2 are:

$$EQE_1 = \frac{I_{ph}}{q \cdot \phi'_1} = \frac{176 \cdot 10^{-12}}{1{,}6 \cdot 10^{-19} \cdot 6{,}3 \cdot 10^{15}} = 17{,}5 \cdot 10^{-8}$$

$$EQE_2 = \frac{I_{ph}}{q \cdot \phi'_2} = \frac{67 \cdot 10^{-12}}{1{,}6 \cdot 10^{-19} \cdot 5{,}3 \cdot 10^{15}} = 7{,}9 \cdot 10^{-8}$$

In order to evaluate the internal quantum efficiency which refers to the electron – hole pairs generated from the active material – MoS_2 per incident photon once the portion of incident power that is absorbed - P_{abs} from the material must be estimated. When incident light reaches a medium of different index of refraction, a part of it is reflected, another part is transmitted through the medium and another part is absorbed from the medium (Figure 4.2.8). The absorbed power can be estimated by subtracting the sum of reflected power – P_r and transmitted power – P_{tr}.

$$P_{abs} = P_{act} - P_r - P_{tr} \tag{3.9}$$

where P_{act} is the active power, P_r is the reflected power and P_{tr} is the transmitted power.

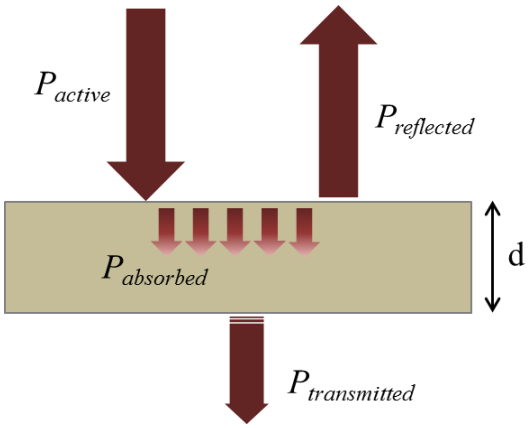

Figure 4.2.8: Schematic of the different portions of incident laser power reaching a medium of thickness d. Here, the active power of incident light is taken into account.

The fraction of incident power that is reflected is defined as

$$P_r = \Re \cdot P_{act} \tag{3.10}$$

where, $\Re$ is reflectivity which depends on the index of refraction n and the extinction coefficient κ of the medium (eq. 3.11) [50]. For propagation of incident light from air ($n_{air} = 1$) to MoS_2 ($n_{MoS_2} \approx 2{,}5$ for few layer MoS_2) [51] and extinction coefficient $\kappa_{MoS_2} \approx 1{,}7$ [51] we can estimate the reflectivity from the surface of the material as

$$\Re = \frac{(1-n_{MoS_2})^2 + \kappa_{MoS_2}{}^2}{(1+n_{MoS_2})^2 + \kappa_{MoS_2}{}^2} = \frac{5{,}14}{15{,}14} = 0{,}34 \tag{3.11}$$

For $P_{act,1}$ =3,134mW and $P_{act,2}$ = 2,661mW the corresponding reflective powers are

- $P_{r,1} = \Re \cdot P_{act,1} = 0{,}34 \cdot 3{,}134 = 1{,}065 mW$
- $P_{r,2} = \Re \cdot P_{act,2} = 0{,}34 \cdot 2{,}661 = 0{,}904 mW$

The transmitted power for light propagation through a medium of thickness d is defined as

$$P_{trans} = P_0 \cdot e^{-a \cdot d} \tag{3.12}$$

where P_0 is the incident power and a is the absorption coefficient of the material. [50] For a ~10^5 cm^{-1} the absorption coefficient of MoS_2 in the visible range [47] and for the material thickness d = 130nm we evaluate a·d = 1.3. Therefore, from equation (3.12) and if we take into account the values of active power $P_{act,1}$ and $P_{act,2}$ we have

- $P_{tr} = P_{act,1} \cdot e^{-1,3} = 0{,}854 mW$ (for $P_{act,1}$ = 3,134mW)
- $P_{tr} = P_{act,2} \cdot e^{-1,3} = 0{,}725 mW$ (for $P_{act,2}$ = 2,661mW)

Consequently, the absorbed power values $P_{abs,1}$ and $P_{abs,2}$ from the material, for the respective values of active power from equation (3.9) are:

- $P_{abs,1} = 3{,}134 - 1{,}065 - 0{,}854 = 1{,}215 mW$ (for $P_{act,1}$ = 3,134mW)
- $P_{abs,2} = 2{,}661 - 0{,}904 - 0{,}725 = 1{,}032 mW$ (for $P_{act,2}$ = 2,661mW)

The respective photon fluxes for the above values of absorbed power are:

$$\phi''_1 = \frac{P_{abs,1}}{E_{ph}} = \frac{1{,}215 \cdot 10^{-3}}{5 \cdot 10^{-19}} \approx 2{,}4 \cdot 10^{15}\ photons/\sec$$

$$\phi''_2 = \frac{P_{abs,2}}{E_{ph}} = \frac{1{,}032 \cdot 10^{-3}}{5 \cdot 10^{-19}} \approx 2{,}1 \cdot 10^{15}\ photons/\sec$$

From the calculations above and taking into consideration only the part of active power that is absorbed from the material we can extract an estimation of the internal quantum efficiency IQE. Thus from equation (3.5) and for photon fluxes ϕ''_1 and ϕ''_2 we have

$$IQE_1 = \frac{I_{ph}}{q \cdot \phi''_1} = \frac{176 \cdot 10^{-12}}{1{,}6 \cdot 10^{-19} \cdot 2{,}4 \cdot 10^{15}} = 45{,}8 \cdot 10^{-8}$$

$$IQE_2 = \frac{I_{ph}}{q \cdot \phi''_2} = \frac{67 \cdot 10^{-12}}{1{,}6 \cdot 10^{-19} \cdot 2{,}1 \cdot 10^{15}} = 19{,}9 \cdot 10^{-8}$$

The small values of the estimated internal quantum efficiency can be attributed to the inevitable presence of defects which induce trap states acting as recombination centers and suppress the efficiency of the as – prepared MoS_2 photodetectors.

4.3 Conclusion

In this thesis, the fabrication and operation of photodetectors based on liquid exfoliated MoS_2 was discussed. Three techniques were employed for the deposition of liquid phase exfoliated MoS_2 i.e. drop – casting, dip – coating, and filtration. Homogenous deposition was achieved only by the drop – casting method and at room temperature solvent evaporation. Consequently, this method was finally chosen for MoS_2 deposition.

Raman analysis revealed the two modes E_{2g}^1 and A_{1g} of 2H – MoS_2 crystal with a mean value of frequency difference at $\Delta\omega \approx 23cm^{-1}$ for all the samples which were tested. This difference was used as estimation for a mean value of three layers for MoS_2 flakes but not with great certainty due to inevitable aggregation and random restacking of the flakes during the sample preparation using MoS_2 dispersion. The broadened line widths of these two modes ($\sim 8cm^{-1}$ for E_{2g}^1 and $\sim 9cm^{-1}$ for A_{1g}) can also be attributed to the presence of defects or to inhomogeneity of the flakes.

Concerning the metallization of the devices, an inter – digitated metal – semiconductor – metal (M – S – M) configuration was applied. Two different types (samples) of this M – S – M arrangement were fabricated. At the first sample which was tested (MoS2_det_01), asymmetric Pt/Ti metal contacts were deposited on $MoS_2/SiO_2/Si$ substrate. A symmetric behavior was observed through the corresponding I – V characteristic for almost all the devices which were tested. This result is in contrast to the rectifying behavior which was expected due to the use of a combination of a high work function Pt (high Schottky barrier) and a low work function Ti metal (Ohmic contact) electrode pair. However, after the annealing process the asymmetry which was observed from the respective curves, was much closer to the expected results.

Regarding the second sample (MoS2_det_02glass) a symmetric Au metallization was used on MoS_2/glass substrate. Au/MoS_2 interface resulted in an ohmic – like behavior due to the similar work functions of Au and MoS_2 and the linear I – V characteristic of the corresponding device.

For the response of the devices under illumination, a laser beam with a wavelength of λ=405nm (E= 3,06eV, energy larger than the band gap of MoS_2) was used for detection.

A non – linear dependence of photocurrent as a function of incident power and a great contribution of Si substrate was observed in the case of the first sample (MoS2_det_01). The measurements were carried out under zero applied voltage due to the built in electric field that occurred at the metal MoS_2 interface.

A linear dependence of photocurrent to incident power was observed for the second sample (MoS2_det_02glass). During the measurements, external bias of V=1V was applied to break the symmetric band alignment of metal/MoS_2 between anode and cathode and to propel the photogenerated carriers.

Internal responsivity was found to be in the order of nA/W ($R_{int,1}$ = 54,63nA/W for $P_{inc,1}$ = 12,6mW, and $R_{int,2}$ = 22,43nA/W for $P_{inc,2}$ = 10,7mW) which is much lower compared to previous reported values (Table 1). Small values of internal quantum efficiency were estimated ($IQE_1 = 45.8 \cdot 10^{-8}$, and $IQE_2 = 19.9 \cdot 10^{-8}$). Even the small calculated values of internal responsivity and quantum efficiency, the device on glass substrate was more suitable for such an analysis because of the linearity in power dependence measurements and the absence of contribution of silicon substrate to the measured photocurrent.

The fabrication techniques used in this thesis were quite simple in operation and low in cost. A significant amount of devises can be made from several droplets of the solution deposited on the same substrate which paves the way for massive production of optoelectronic devices. However, further investigation is needed in order to achieve better results for the operation of the devices. The use of monolayer MoS_2 flakes (with direct band gap) and the deposition of asymmetric metal contacts which should induce Schottky barriers at the metal/semiconductor interface (to reduce the dark current) on glass substrate, are some actions that could lead to an improvement of the efficiency and fast response of photodetectors.

References

[1] Q. Wang, J. Lai, and D. Sun "Review of photo response in semiconductor transition metal dichalcogenides based photosensitive devices", *Optical Materials Express* , 6(7), pp. 2313-2327, 2016.

[2] M. Ye, D. Winslow, D. Zhang, R. Pandey, and Y. K. Yap, "Recent advancement on the optical properties of two-dimensional molybdenum disulfide (MoS_2) thin films, *Photonics*, 2, pp. 288-307, 2015.

[3] X. Zhang, X. F. Qiao, W. Shi, J. B. Wu, D. S. Jiang, and P. H. Tan, "Phonon and Raman scattering of two – dimensional transition metal dichalcogenides from monolayer, multilayer to bulk material", *Chem. Soc. Rev.*, 44, pp. 2757-2785, 2015.

[4] J. Jia, F. Xu, S. Wang, X. Jiang, Z. Long, and X. Hou , "Two-dimensional MoS_2 nanosheets as a capillary GC stationary phase for highly effective molecular screening", *Analyst*, 139, pp. 3533- 3536, 2014.

[5] B. Radisavljevic, A. Radenovic, J. Brivio, V. Giacometti, and A. Kis, "Single-layer MoS_2 transistors", *Nature Nanotechnology*, 6, pp. 147-150, 2011

[6] S. L. Li, K. Tsukagoshi, E. Orgiu, and P. Samorì, "Charge transport and mobility engineering in two-dimensional transition metal chalcogenide semiconductors", *Chem. Soc. Rev*, 45, pp. 118-151, 2016.

[7] G. Eda, H. Yamaguchi, D. Voiry, T. Fujita, M. Chen, and M. Chhowalla, "Photoluminescence from chemically exfoliated MoS_2", *Nano Lett.*, 11 (12), pp 5111-5116, 2011.

[8] K. F. Mak, K. He, J. Shan, and T. F. Heinz, "Control of valley polarization in monolayer MoS_2 by optical helicity", *Nature Nanotechnology*, 7, pp. 494-498, 2012.

[9] J. G. Kim, W. S. Yun, S. Jo, J. Lee, and C.-H. Cho, "Effect of interlayer interactions on exciton luminescence in atomic – layered MoS_2 crystals", *Scientific Reports*, 6, no. 29813, 2016.

[10] Y. Wang, C. Cong, C. Qiu, and T. Yu, "Raman spectroscopy study of lattice vibration and crystallographic orientation of monolayer MoS_2 under uniaxial strain", *Small*, 9(17), pp. 2857-2861, 2013.

[11] H. Li, Q. Zhang, C. C. R. Yap, B. K. Tay, T. H. T. Edwin, A. Olivier, and D. Baillargeat "From bulk to monolayer MoS_2: Evolution of Raman scattering", *Adv. Funct. Mater.*, 22, pp. 1385-1390, 2012.

[12] S. Najmaei, Z. Liu, P. M. Ajayan, and J. Lou, "Thermal effects on the characteristic Raman spectrum of molybdenum disulfide (MoS_2) of varying thicknesses", *Appl. Phys. Lett.* 100, no. 013106, 2012.

[13] Q. H. Wang, K. Kalantar-Zadeh, A. Kis, J. N. Coleman, and M. S. Strano, "Electronics and optoelectronics of two-dimensional transition metal dichalcogenides", *Nature Nanotechnology*, 7, pp. 699-712, 2012.

[14] H. Zeng, and X. Cui, "An optical spectroscopic study on two dimensional group-VI transition metal dichalcogenides", *Chem. Soc. Rev*, 44, pp. 2629-2642, 2015.

[15] K. S. Novoselov, A. K. Geim, S. V. Morozov, D. Jiang, Y. Zhang, S. V. Dubonos, I. V. Grigorieva, and A. A. Firsov, "Electric field effect in atomically thin carbon films", *Science*, 306, pp. 666-669, 2004.

[16] F. Wang, Z. Wang, Q. Wang, F. Wang, L. Yin, K. Xu, Y. Huang, and J. He, "Synthesis, properties and applications of 2D non-graphene materials", *Nanotechnology*, 26, no. 292001, 2015.

[17] M. Placidi, M. Dimitrievska, V. Izquierdo-Roca, X. Fontané, *et al*, "Multiwavelength excitation Raman scattering analysis of bulk and two-dimensional MoS_2: vibrational properties of atomically thin MoS_2 layers", *2D Mater.*, 2, no. 035006, 2015.

[18] J. R. Creighton, and P. Ho, "Introduction to Chemical Vapor Deposition (CVD)", *ASM International*, (#06682G), 2001.

[19] Y. P. Venkata Subbaiah, K. J. Saji, and A. Tiwari, "Atomically Thin MoS_2: A versatile non-graphene 2D material", *Adv. Funct. Mater.*, 26, pp. 2046-2069, 2016.

[20] Z. Gholamvand, D. McAteer, C, Backes, N. McEvoy, A. Harvey, *et al*, "Comparison of liquid exfoliated transition metal dichalcogenides reveals $MoSe_2$ to be the most effective hydrogen evolution catalyst", *Nanoscale*, 8, 5737-5749, 2016.

[21] S. Das, H.-Y. Chen, A. V. Penumatcha, and J. Appenzeller, "High Performance Multilayer MoS_2 Transistors with Scandium Contacts", *Nano Lett.*, 13, pp.100-105, 2012.

[22] D. Jariwala, V. K. Sangwan, L. J. Lauhon, T. J. Marks, and Mark C.Hersam, "Emerging device applications for semiconducting two-dimensional transition metal dichalcogenides", *ACS Nano*, 8, pp. 1102-1120, 2014.

[23] M. Fukuda, "Optical semiconductor devices".

[24] Z. Yin, Hai Li, Hong Li, L. Jiang, Y. Shi, Y. Sun, G. Lu, Q. Zhang, X. Chen, and H. Zhang, "Single-layer MoS_2 phototransistors", *ACS Nano*, 6, pp. 74-80, 2012.

[25] W. Choi, M. Y. Cho, A. Konar, J. H. Lee, G.-B. Cha, S. C. Hong, S. Kim, J. Kim, D. Jena, J. Joo, and S. Kim, "High-detectivity multilayer MoS_2 phototransistors with spectral response from ultraviolet to infrared", *Adv. Mater.*, 24, pp.5832-5836, 2012.

[26] O. Lopez-Sanchez, D. Lembke, M. Kayci, A. Radenovic, and A. Kis, "Ultrasensitive photodetectors based on monolayer MoS_2", *Nature Nanotechnology*, 8, pp. 497-501, 2013.

[27] D.-S. Tsai, K.-K. Liu, D.-H. Lien, M.-L. Tsai, C.-F. Kang, C.-A. Lin, L.-J. Li, and Jr-H. He, "Few layer MoS_2 with broadband high photogain and fast optical switching for use in harsh environments", *ACS Nano*, 7, pp. 3905-3911, 2013.

[28] N. Perea-López, Z. Lin, N. R Pradhan, A. Iñiguez-Rábago, A. L. Elías, A. McCreary, *et al*, "CVD-grown monolayered MoS_2 as an effective photosensor operating at low-voltage",*2D Mater.*, 1, 011004, 2014.

[29] S. Ghosh, A. Winchester, B. Muchharla, M. Wasala, S. Feng, A. L. Elias, M. Bala M. Krishna, *et al*, "Ultrafast intrinsic photoresponse and direct evidence of sub-gap states in liquid phase exfoliated MoS_2 thin films", *Scientific Reports*, 5, 11272, 2015.

[30] T. Mueller, F. Xia, and P. Avouris, "Graphene photodetectors for high-speed optical communications", *Nature Photonics*, 4, pp. 297-301, 2010.

[31] M. Fontana, T. Deppe, A. K. Boyd, M. Rinzan, A. Y. Liu, M. Paranjape, and Paola Barbara, "Electron-hole transport and photovoltaic effect in gated MoS_2 Schottky junctions", *Scientific Reports*, 3, 1634, 2013.

[32] M. Buscema, J. O. Island, D. J. Groenendijk, S. I. Blanter, G. A. Steele, H. S. J. van der Zant, and A. Castellanos-Gomez, "Photocurrent generation with two-dimensional van der Waals semiconductors", *Chem. Soc. Rev*, 44, pp. 3691-3718, 2015.

[33] Z. Sun and H. Chang, "Graphene and graphene – like two – dimensional materials in photodetection: mechanisms and methodology", *ACS Nano*, 8 (5), pp. 4133-4156, 2014.

[34] http://www.slideshare.net/jakkaas/electron-microscope-7739581

[35] Measurement of critical dimension in scanning electron microscope mask images, Wonsuk Lee et al, J. Micro/Nanolith. MEMS MOEMS. 10(2), 023003 (April 27, 2011). doi:10.1117/1.3574771

[36] http://serc.carleton.edu/research_education/geochemsheets/techniques/SEM.html

[37] http://www.mee-inc.com/hamm/scanning-electron-microscopy-sem/

[38] G. S. Bumbrah, R. M. Sharma, "Raman spectroscopy – Basic principle, instrumentation and selected applications for the characterization of drugs of abuse", *Egypt J Forensic Sci*, http://dx.doi.org/10.1016/j.ejfs.2015.06.001, 2015.

[39] G. Gouadec, P. Colomban, "Raman Spectroscopy of nanomaterials: How spectra relate to disorder, particle size and mechanical properties", *Progress in Crystal Growth and Characterization of Materials, Elsevier*, 53 (1), pp. 1-56, 2007.

[40] M. Palsson, "Raman spectroscopy and confocal Raman imaging", 2003.

[41] W.E. Smith, and G. Dent, "Modern Raman spectroscopy – A practical approach".

[42] G. E. Peckham, "Phonon Dispersion Relations in Crystals", Trinity College, Cambridge.

[43] M.S. Dresselhaus, G. Dresselhaus, R. Saito, A. Jorio, "Raman spectroscopy of carbon nanotubes", *Physics Reports*, 409, pp. 47-99, 2005.

[44] L. Jiadan, "Investigation of electronic and optical properties of molybdenum disulfide modulated by surface functionalization", B.Sc. Sichuan University, Department of Physics, 2014.

[45] A.E. Grigorescu, and C.W. Hagen, “Resists for sub-20-nm electron beam lithography with a focus on HSQ: state of the art”, *Nanotechnology*, 20, 292001, 2009.

[46] A. Pimpin, and W. Srituravanich, “Review on micro- and nanolithography techniques and their applications”, *Engineering Journal*, 16 (1), pp. 37-56, ISSN 0125-8281, 2012.

[47] D.-S. Tsai, D.-H. Lien, M.-L. Tsai, S.-H. Su, K.-M. Chen, J.-J. Ke, Y.-C. Yu, *et al*, “Trilayered MoS_2 metal–semiconductor–metal photodetectors: photogain and radiation resistance”, *IEEE Journal of Selected Topics in Quantum Electronics*, 20 (1), 3800206, 2014

[48] C. Lee, H. Yan, L. E. Brus, T. F. Heinz, J. Hone, and S. Ryu, “Anomalous lattice vibrations of single and few-layer MoS_2”, *ACS Nano*, 4 (5), pp. 2695-2700, 2010.

[49] H. S. Yoon, H.-E. Joe, S. J. Kim, H. S. Lee, S. Im, B.- K. Min and S. C. Jun “Layer dependence and gas molecule absorption property in MoS_2 Schottky diode with asymmetric metal contacts”, *Scientific Reports*, 5, 10440, 2015.

[50] H. Zimmermann, “Basics of optical emission and absorption”, Integrated Silicon Optoelectronics, 2000.

[51] C. Yim, M. O’Brien, N. McEvoy, S. Winters, I. Mirza, J. G. Lunney, and G. S. Duesberg, “Investigation of the optical properties of MoS_2 thin films using spectroscopic ellipsometry”, *Appl. Phys. Lett*, 104, no. 103114, 2014.